Modelling prerequisites – FEM/SEA

Impact and Airborne Sound

Delphine Bard
Juan Negreira
Catherine Guigou Carter
Gerard Borello
Jean-Luc Kouyoumji
Alice Speranza
Corentin Coguenanff
Klas Hagberg

Report no STB01 WG1
RISE Report 2017:56

SILENT TIMBER BUILD

RISE Research Institutes of Sweden AB

RISE Rapport: 2017:56
ISBN: 978-91-88695-23-9
Göteborg

Table of Contents

1. Introduction

This report comprises results from the work done within work package 1 in the WWN+ project “Silent Timber Build”, WP 1: *Prediction tools, low and high frequencies*. The aim from this WP was to develop prediction tools applied for wooden constructions. Included in this is also to create necessary basis for enough accuracy for any European wood construction. It implies development of new methods but also to understand how input forces primarily from the tapping machine affects the results of impact sound levels. The WP also describes how models are developed, in order to provide expected accuracy and then how to further improve the models in order to optimize floor and wall assemblies. The Work Package has been closely linked to WP 2 but also WP3. Using the results from WP 2, the prediction model results can be compared to expected values for any European construction. From that optimization of floor assemblies and refining of the model is possible.

The work package included four tasks. First task is to identify a European target value primarily for impact sound insulation and airborne sound insulation. Task two and three includes the development of prediction models depending on frequencies considered and finally task four is needed to combine the different approaches, main principles are given in figure 1.1.

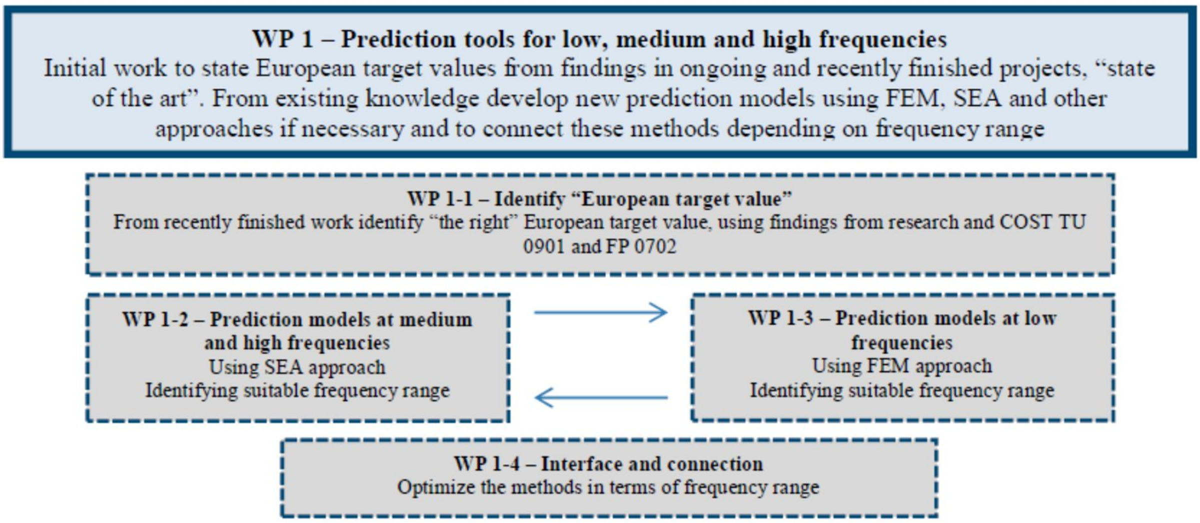

Figure 1.1: Schematic overview of Work Package 1

During the progress of the work, some adaptations have been made due to valuable findings throughout the project (and parallel projects). Impact sound is the most complex topic for sound insulation in buildings in terms of input forces but also in terms of annoyance, particularly in multi-family residential buildings. Impact sound is less easy to predict compared to airborne sound. The prediction of airborne sound using Silent Timber Build methods are satisfactory, not least due to the fact that the low frequencies is of less importance compared to the case with impact sound.

To this end, a “first level tool” based on combining complex methods and theory is proposed. Simplifications based on the important parameters identification are suggested (see also report from WP 2). This methodology has been applied for both levels of prediction: the components (floors and walls) acoustic performance and the building acoustic performance (including direct and flanking sound transmissions). After considerations from Task no 1 and grouping from WP 2, main focus has been to model floor assemblies (as also mentioned previously). Wall assemblies are also included and so are junctions. For the latter the development comprises mainly input from extensive measurement campaigns, which is useful as input for any standardized models and future commercial software invariants.

1.1 Task 1 – Identify “European Target Values”

The target values for sound insulation in buildings might vary a lot depending on which country that might be of interest, even within Europe. For wooden floor and wall assemblies, there are a common interest to adapt the current target values to future expectations from habitants, in order to compete with any other structural material with completely different physical characteristics. Hence, when predicting the sound insulation at present it is necessary to think beyond the current legislation and to predict for “the future”. The future for habitants but also for a future sustainable wooden industry.

Following the recommendations from COST / TU0901 the frequency range that should be covered starts at 50 Hz and terminates at 3150 Hz. New research has shown that it might be of importance to cover frequencies down to 20 Hz (e.g. down to the frequency limit for the human hearing), however it is not yet “secured” enough in order to introduce that into any regulatory framework [57]. In spite of remaining uncertainties, Silent Timber Build has covered the frequency range between 20 Hz and up to 3150 Hz as the ability to predict sound insulation, has been investigated.

1.2 Task 2 – Prediction models at medium and high frequencies

For the medium and high frequencies modelling approaches have been carried out by using a combination of FEM and SEA, see sections 2.1, 3.1, 2.2 and 3.2. For the “normal” standardized frequency range 100 Hz – 3150 Hz used to evaluate weighted sound reduction index and weighted impact sound levels according to ISO 717-1 and 2, a software is used which has been further developed within the “Silent Timber Build” project. The software is SEAWOOD [40] and provided by the project partner InterAC. To cover the extended standardized frequency range according to ISO 717 (from 50 Hz) combinations of SEA and FEM are used, in various manners. An FEM-to-SEA converter algorithm is included in SEAWOOD as an additional software module. This module implements a proprietary technique named Virtual SEA [41] to analyze the modal dynamics of the FEM model and to derive, using an intelligent inverse method, the most appropriate SEA representation that provides both SEA partition into subsystems and related SEA model parameters which restitute the observed spaced and frequency band-averaged velocity transfer provided by the original FEM model. Related models are called VSEA models.

VSEA methodology is quite interesting as it provides from a FEM model representation of a dynamical system, easy to measure SEA parameters in rather automated way. The most efficient measurement technique for validating FEM and related Virtual SEA models is the inverse SEA method [42, 45] based on recording vibrational point-to-point transfer functions as implemented in SEA-TEST and SEA-XP software [43, 44]. SEA parameters such as damping and coupling loss factors, equivalent mass, modal density and driving point mobility can be compared in band-integrated frequency format such as Octave or 1/3rd octave frequency bands.

The SEA model is generally made of a few subsystems so that deficiency of FEM models, if any, shall be easily brought to the fore by cross-checking against measurements each of the elementary FEM-derived VSEA parameters. Because only modal amplitudes at a limited set of nodes are required as input to the VSEA inverse solver, the extraction of eigenvalues and eigenshapes of the FEM model is possible up a frequency limit where the propagating wavelength is about 10 times the size of the FE mesh. Wood structures are thick and relatively stiff, floor structural FEM models can be computed and VSEA processed up to 2000 Hz of standard PC [46], covering what is called the medium frequency range. From 1000 Hz and above, the vibrational energy within timber-framed structures is quite diffuse with strong energy gap at discontinuities such as change in thickness, material or joint. Analytical SEA takes over the calculation. The VSEA parameters limited into frequency by the FEM mesh size are then expanded by related analytical operators embedded in the VSEA subsystems which extend the frequency limit above 20 kHz. The VSEA model is then becoming an SEA hybrid model partly built from FEM and partly from analytical operators. VSEA models of that kind can then be run on an extended frequency range from typically 100 Hz to 20000 Hz.

Whenever it is possible, the VSEA model may be converted into an equivalent analytical SEA model, leading to faster calculation and on-the-fly change of dynamic system properties in order to guide acoustic design. Next picture (figure 1.2) illustrates the data flow process of VSEA method for identifying the SEA parameters of a coupled floor-wall system.

The final VSEA model is made of four panel subsystems and gives access to all SEA parameters of such a model as modal densities and mean driving-point mobility of individual panels and coupling loss factors between panels. Figure 1.3 shows a comparison of VSEA driving-point mobility of the floor with a related simulation using analytical modeling of the floor as SEAWOOD rib-stiffened plate. A good agreement is seen regarding the spectral evolution of both mobilities of the FEM-derived result and the analytical one but also significant differences in some frequency-band as the analytical simulation cannot capture with accuracy all detailed features of the 3D geometry of this system while FEM can. The ability to predict mobility is an important feature for tuning analytical models as the band-averaged driving point mobility is a descriptor which quickly converges to the driving point mobility of the corresponding infinite medium (thin plate in that case), a parameter independent of subsystem size.

Further in this document, other examples of SEA simulations of timber-framed structures will be shown and discussed.

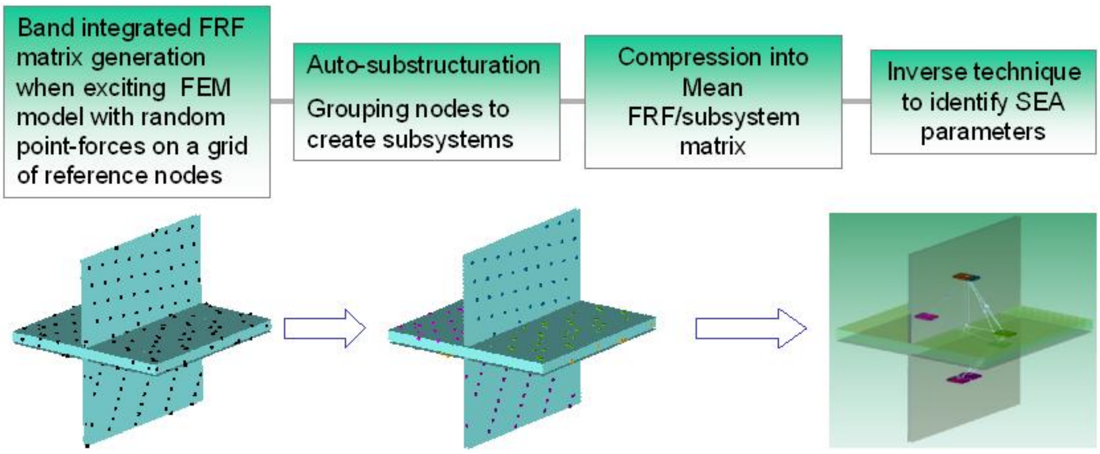

Figure 1.2: Analysis of wall-to-floor junction using VSEA method

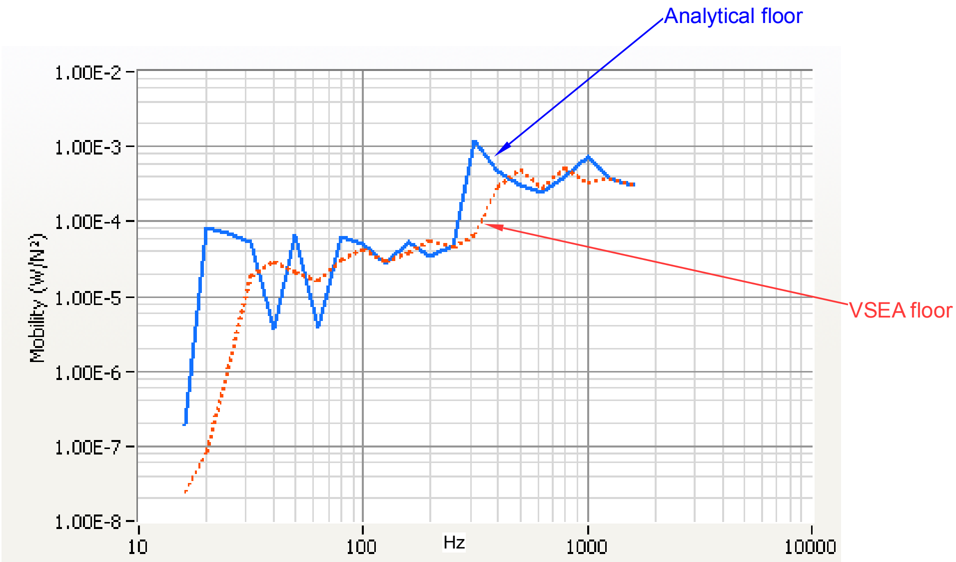

Figure 1.3: Analysis of wall-to-floor junction using VSEA method

1.3 Task 3 – Prediction models at low frequencies

For the lowest frequencies, modelling has been carried out specifically by using FEM, see sections 2.1 and 3.1. The simulations cover the frequency range from 20 Hz to 200 Hz. A number of comparisons between predicted and measured values have been done with floor assemblies built up in the laboratory in IBP Fraunhofer Institute in Stuttgart, and the floors were delivered from the industrial project partner Bauer Holzbau in Germany.

In general, the accuracy is rather limited in the lowest frequency range in each third octave band, especially for impact sound insulation. The accuracy for impact sound stabilizes at 31,5 Hz but still there are some difficulties. That is also the reason why the project invested a lot of time and effort to characterize the tapping machine, see section 4. If only studying single numbers the accuracy is improving.

For airborne sound third octaves the accuracy is ±20 dB at 20 Hz and diminishes rather quick to ±10 dB at 100 Hz. For more detailed description, see section 3 (FEM).

1.4 Task 4 – Interface and connections

For the standardized frequency range applied for commercial buildings and other public buildings the SEAWOOD software can be used solely. For dwellings with high requirements, a combination of FEM and SEA is proposed since the low frequencies have to be considered as well, in particular for residential buildings with high requirements. Often SEAWOOD combined with the built-in SEAVirt (the FEM-postprocessing module) implementing the VSEA FEM-to-SEA conversion method [46,47] will be sufficient. However if the structures become complex and more long span, detailed FEM prediction should be applied as well.

Additionally, measurements of transmission losses through junctions have been undertaken in order to provide better basis for future improved standardized calculation models, K_{ij} measurements. For this, some tests have been done by the project partner FCBA in a real building with typical CLT junctions. Kij parameters can be easily predicted by SEA simulation model from their definition. Examples of Kij prediction will be given in the following.

Predicting Sound Transmission Loss (STL) of lightweight constructions has to deal with anisotropic structures with multiple build-up possibilities. Each design of wall or floor is associated to a modeling strategy. SEA proves to be a seductive theory because it can be easily applied. Indeed, its developments do not need any elaborate numerical method. Modelling involves cutting the structure into sub-systems (spatial) and decomposing the spectrum into octaves or thirds of octave (frequency dependant). In this way, the exchange of energy flow in the sub-structures can be analyzed. The parameters that govern vibrational transmission between subsystems are damping and coupling loss factors (DLF and CLF). DLF and CLF can be identified experimentally by reversing the problem (Reverse SEA). This feature in particular makes SEA the most effective design tool in structural acoustics and vibration. SEA can be mixed with TMM or FEM, it is then the framework used for different theories that uses energy as state variable, see section 2.2.

The project partner Rothoblaas has also provided an extensive measurement series of Kij, however limited to the frequency range 100 Hz – 3150 Hz. Nevertheless the basis for calculation using EN12354 model, see section 2.3 and section 3.3.

2. Methods

2.1 FEM

2.1.1 General

Separating lightweight systems in building constructions are complex assemblies combining the intrinsic properties of each component to meet various constraints: mechanical durability, thermal insulation, sound insulation etc. Figure 2.1 gives examples of common geometries and highlight existing structural transmission paths, inherent to many timber based designs.

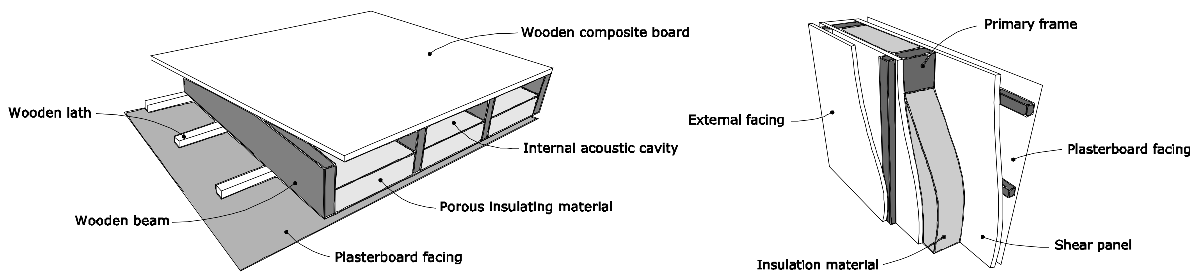

Figure 2.1: Common floor assembly using joists in wood based lightweight systems

The finite element method is attractive for modeling such systems due to its ability to solve boundary value problems within geometries of arbitrary complexity. However, most of the time, the main drawback of such approach lies in the non-negligible modelling effort that has to be put in every time a new geometry is considered. A prerequisite to spread out those methodologies and to use FE models as an everyday approach to system design would consequently be to drastically reduce modelling efforts. Fortunately, typical building systems display rectangular geometries and components, patterns, and can be decomposed in regular layers. A high-level description of the geometry can be constructed in terms of parameters such as “layer thickness”, “number of studs” etc. Then, such a high-level description can be interpreted by a dedicated FE code for the direct generation of the meshes and models. This was achieved during the course of the work [1] and the obtained computational code is used in following applications.

2.1.2 Computational vibro-acoustic model

Typical wood-based systems can be decomposed into three classes of physical components: solid elastic that might be slender (facing, shear panel, etc.) or not (primary or secondary wood frames), poroelastic domains (mostly fibrous insulation materials) able dissipate acoustic energy through thermal and viscous losses and acoustic fluid domains (air cavities). Classical linear theories [2], [3], dedicated to each class, are used in order to build a coupled vibro-acoustic problem.

Then, a finite-element mesh is constructed over the different domains as shown in figure 2.2. The fields from continuum mechanics (displacement, pressure, etc.) are interpolated on finite-element basis from their nodal values. At each frequency, a finite set of equations results from the process and yields a computational model associated with the coupled vibro-acoustic problem. The limitation of such an approach lies within the number of elements (number of unknown) that has to be included in order to catch mechanical wavelengths that get shorter with increasing frequency.

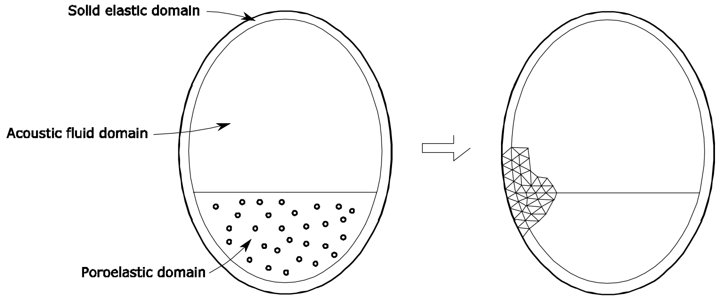

Figure 2.2: Domain discretization : finite-element mesh

2.1.3 External excitation

Various system acoustic performances are classically evaluated with respect to two criteria: airborne sound insulation (vertical and horizontal systems) and impact sound insulation (horizontal systems). Both are linked to the ability of a system to display minimal sound radiation while excited by an airborne source (pressure field) for the former, and impacts (localized forces) for the latter. Associated normalized performance indices and measurement principles can be found within Refs. [4]–[8].

From the modeling point of view, such evaluations require to generate corresponding external excitations on the system. That is: an acoustic pressure field and/or impacts resulting from the standard tapping machine. CSTB work [1, 11] has concentrated in developing a method for both problems in using FEM and in particular for the excitation associated with the tapping machine. In fact, impact forces depend on the structure being excited so that the excitation depends on the position of the falling tapping machine hammer. Up to 6 dB variations can be expected at low frequencies due to momentum differences between impacts with and without rebound [9]. Once the injected force spectrum is known, the vibrational field of the floor system is obtained using standard FEM. Deterministic as well as probabilistic approaches and applications were presented in Refs. [10], [11].

2.1.4 Sound radiation

Once the vibrational field of the building system is known, radiated power can be evaluated. Sound radiation of the baffled system within a semi-infinite acoustic medium is the most straightforward approach. However, abundant literature argue for the use of a more detailed model able to take into account the available information about the effective acoustic volume in which the system radiates energy [12]–[19]. Indeed, at low frequencies, acoustic volumes such as laboratory rooms display low modal overlap: sound pressure levels are locally dominated by acoustic modes and thus strongly depend on room characteristics. Comparisons undertaken in Refs. [12], [16], [17] display a good agreement between computed sound pressure levels in rigid parallelepiped acoustic enclosures and experimental results. In particular, with regard to such narrow band results, experimental and computed resonances and anti-resonances are consistent with each other. However, damping (and consequently energy levels per band) appears as a critical concern for aimed accurate third-octave band prediction.

2.1.5 Airborne sound insulation

In order to justify of discuss modelling choices, a bit of context is first recalled. Within laboratory conditions, airborne sound insulation is measured between a source room and a receiving room separated by the evaluated system (see figure 2.3). According to standard procedure [4], various loudspeaker positions have to be used for the generation of a steady sound pressure field in the source room. The aim is then to evaluate the sound reduction index *R*, defined as a ratio of incident and radiated sound power such that :

$$R = 10\,\log_{10}\frac{W_S}{W_R}\,. \tag{2.1}$$

In order to evaluate such ratio, Sabine theory is classically used to link sound powers and the spatial average of the quadratic pressure fields. Then, the sound reduction index reduces to

$$R = L_S - L_R\ + 10\,\log_{10}\frac{S}{A}\,, \tag{2.2}$$

where L_S, L_R, S and A respectively denote the sound pressure levels in the source and receiving rooms, system surface and equivalent acoustic absorption area.

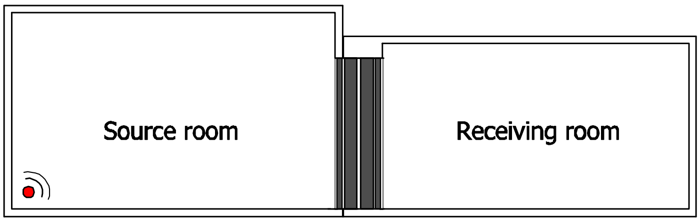

Figure 2.3 : Laboratory setup for airborne sound insulation

Thus, sound reduction index is, at first, defined as a power ratio, and could be modelled as such in using diffuse field theory, plane wave excitation and baffled sound radiation within half-space. However, practical evaluation is performed in using sound pressure levels which are closely related to sound powers through Sabine theory, under the critical assumption of diffuse sound fields. At low frequencies, given the room dimensions, it can be expected that such an assumption is not valid. Sound reduction index as defined by Eq. (2.2) does not represent power flows anymore. Then, the modelling of the sound reduction index as a sound power ratio would introduce a distance between predicted and measured quantities.

As a way of consequence, we present in the following a methodology trying to be as close to laboratory conditions as possible such that numerical and experimental quantities are comparable as far as this could be relevant. It should be noted that given the current state of the art, such an approach remains exploratory and primarily aims to define a suitable work basis.

Parallelepiped room model

Hereinafter, the pressure field and the sound pressure level in the source room as well as the sound pressure level in the receiving room are evaluated in using a basis of analytical solutions of the Helmoltz equation in a rigid parallelepiped room. The expansion of pressure fields on such a normalized truncated basis can be written as:

$$p(\omega;\boldsymbol{x}) = \sum_{p,q,r} A_{pqr}(\omega)\,\varphi_{pqr}(\boldsymbol{x})\,, \tag{2.3}$$

where functions $\varphi_{pqr}(\boldsymbol{x})$ are constructed from classical cosine products.

Then, the generalized coordinates (or expansion coefficients) $A_{pqr}(\omega)$ are fully determined by the knowledge of a spatial distribution of acoustic sources $Q(\omega;\boldsymbol{x})$ and can be computed as :

$$A_{pqr}(\omega) = \frac{\iiint Q(\omega;\boldsymbol{x})\,\varphi_{pqr}(\boldsymbol{x})\,d\boldsymbol{x}}{\omega_{pqr}^2 + 2i\xi_{pqr}\omega\omega_{pqr} - \omega^2} \tag{2.4}$$

Acoustic damping experimental information is contained within measured frequency dependent reverberation times such that factor ξ_{pqr} can be constructed as [20] :

$$\xi_{pqr} = \frac{1}{2}\frac{2.2}{f_{pqr}\,T} \tag{2.5}$$

However, it should be noted that at low frequencies such approach has the limits of the reverberation time itself [21]. It is used here as default because no better information is available.

Finally, in using the orthogonality properties of functions $\varphi_{pqr}(\boldsymbol{x})$ over the acoustic domains, spatial averages of the quadratic sound pressure can be computed as :

$$\langle p^2(\omega)\rangle_V = \frac{\rho c^2}{V}\sum_{p,q,r}\left|A_{pqr}(\omega)\right|^2 \tag{2.6}$$

In the following, the spatial distribution of acoustic sources $Q(\omega;\boldsymbol{x})$ will be constructed either from acoustic monopoles (Dirac distributions) for the source room, or from the parietal velocity field of the evaluated system for the receiving room. For the sake of clarity, the adopted decoupled approach is briefly summarized:

- As a first step, the source room is considered as an independent dynamical system. With respect to a given acoustical excitation, the sound pressure field can be determined according Eq. (2.3). Then, an incident pressure field on the boundary with the evaluated system as well as the spatial average of the quadratic pressure field can be evaluated in the source room.

- As a second step, the external excitation on the system is constructed from the incident pressure field resulting from the first step. A computational model of the system, constructed from the finite element method, is then solved for the displacement field of the structure on the boundary with the receiving room.

- As a third step, the receiving room is considered as an independent dynamical system. Then, the acoustical excitation of the receiving room is constructed from the displacement field of the structure on the boundary with the receiving room. Finally, the spatial average of the resulting quadratic sound pressure field can be evaluated.

2.1.6 Impact sound insulation

Within laboratory conditions, the evaluated system is placed over a receiving room (see figure 2.4). A standard tapping machine is used for the generation of a steady mechanical excitation in various positions. Then, microphones in the receiving room provide the spatial sampling of the sound pressure field in the receiving room used to evaluate the spatial and time average of the quadratic pressure field. Consequently, a methodology consistent with the one presented in for airborne sound insulation will be used for the evaluation of the sound pressure level in the receiving room. In the following, we must put the emphasis on the structural excitation, which is a sequence of impacts resulting from the standard tapping machine [5], [6].

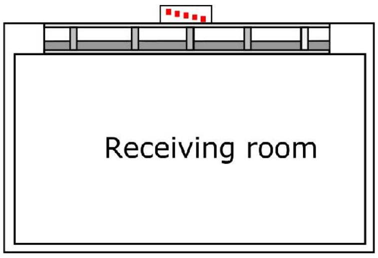

Figure 2.4: Laboratory setup for impact sound insulation

Tapping machine model

The following description of the standard tapping machine can be found in [6], [9]. The experimental setup is such that five equally spaced hammers of mass $M_h = 0.5\ \mathrm{kg}$ hit the structure along a 40 cm line after a free fall from a $h_f = 4\ \mathrm{cm}$ height. Each hammer strikes the floor with the velocity $v_0 = \sqrt{2gh_f} = 0.886\ \mathrm{m/s}$ (standard acceleration due to gravity $= 9.81\ \mathrm{m.s^{-2}}$) at a given time period $T = 0.5\ \mathrm{s}$ and with a time shift from the previous one of $\Delta T = 0.1\ \mathrm{s}$. By way of consequence, the force time signal $f_h(t)$ resulting from a periodic impact of hammer *h* can be expanded using a complex Fourier series such that :

$$f_h(t) = \sum_{n=-\infty}^{+\infty} f_n^h\ e^{i\frac{2\pi n}{T}t}, \tag{2.7}$$

in which

$$f_n^h = \frac{1}{T}\int_0^T f_h(t)\ e^{-i\frac{2\pi n}{T}t}\ \mathrm{d}t. \tag{2.8}$$

Moreover, Fourier transform and inverse Fourier transform are defined by using the convention:

$$\hat{f}(\omega) = \int_{-\infty}^{+\infty} f(t)\ e^{-i\omega t}\ \mathrm{d}t \quad \text{and} \quad f(t) = \frac{1}{2\pi}\int_{-\infty}^{+\infty} \hat{f}(\omega)\ e^{i\omega t}\ \mathrm{d}\omega \quad . \tag{2.9}$$

According to Eqs. (2.7) and (2.9), the spectrum $\hat{f}_h(\omega)$ associated with the periodic impact of the hammer *h* can be written as:

$$\hat{f}_h(\omega) = \sum_{n=-\infty}^{+\infty} f_n^h \, \delta(\omega - \omega_n) \, , \tag{2.10}$$

where $\omega_n = \frac{2\pi n}{T}$ and $\delta(.)$ denotes the Dirac distribution. Thus, in can be noted that the force spectrum takes discrete values every 2 Hz. Moreover, low frequency bounds for f_n^h can be derived in using maximal and minimal momentum variations [9]. Fourier coefficients f_n^h are then comprised between $2M_h v_0/T$ and $M_h v_0/T$ respectively for an impact with rebound and an impact without rebound.

Let $F(\omega; \boldsymbol{x})$ be the whole external excitation field associated with the five hammers, we then have :

$$F(\omega; \boldsymbol{x}) = \sum_{h=1}^{5} \hat{f}_h(\omega) \; e^{-i\omega h \Delta T} \, \delta(\boldsymbol{x} - \boldsymbol{x}_h) \, . \tag{2.11}$$

where $\boldsymbol{x}_h$ denotes the impact position of hammer *h*.

Following, it can be noted that every 10 Hz, complex exponentials $e^{-i\omega h \Delta T}$ are in phase, applied force and injected powers are then maximal. Then, according to this model, the excitation spectrum takes discrete values every 2 Hz, with maximal values every 10 Hz. At very low frequencies, in can be understood how structural resonances positioning with respect to maximal excitation frequencies could be critical in the framework of this standard setup.

Numerical evaluation of Fourier coefficient

The evaluation of Fourier coefficients f_n^h through Eq. (2.8) requires adequate sampling of the time signal $f_h(t)$. Within the context of lightweight building systems, and in particular for joisted floors, high spatial variations of input mobility can be observed. Thus, variations of impact forces can be expected depending of the impact point. Previous observations indicate that, in the low frequency range, such variations can be expected to belong to a 6 dB wide interval ($2M_h v_0/T$ and $M_h v_0/T$). Hereinafter, a finite element based method is proposed for the sampling of impact force time signal $f_h(t)$ function of the impact point.

For any $t \geq 0$, a finite-element model of the elastic structure subjected to a single impact from a mass M_h at velocity v_0 can be written as :

$$([\mathbb{M}] + [\Delta\mathbb{M}_h])\ddot{\mathbb{U}}(t) + [\mathbb{D}]\dot{\mathbb{U}}(t) + [\mathbb{K}]\mathbb{U}(t) = \mathbf{0} \, , \tag{2.12}$$

$$\dot{\mathbb{U}}(0) = v_0 \mathbb{E}_h \, , \tag{2.12}$$

$$\mathbb{U}(0) = \mathbf{0} \, , \tag{2.12}$$

where $\mathbb{E}_h$ is a vector that has null elements but 1 on the line corresponding to the degree of freedom impacted by hammer *h*. Moreover, $[\Delta\mathbb{M}_h]$ corresponds to the mass added by the hammer to the system during the impact time. We then have $[\Delta\mathbb{M}_h] = \mathbb{E}_h M_h \mathbb{E}_h^{\mathrm{T}}$.

After the impact the system is freely evoluting from the kinematical initial conditions. An unconditionnaly stable Newmark scheme (see for example [22]) can be used for the direct numerical integration of the equations with a time step Δt. The simulation is then stopped at the time t_{cut}, corresponding to *n* steps , of the first zero-crossing of the acceleration at the impact point. Indeed, the null acceleration at the impact point means that the hammer is projected away from the system.

Following, displacements, velocities and acceleration's are known for each degree of freedom during the impact time. In particular, the acceleration at the impact point can be used to evaluate the impact force time signal. The obtained sampled time signal corresponds to the discretization of $f_h(t)$ and can be used in the numerical evaluation of Eq. (2.8) to obtain the Fourier coefficients.

2.2 SEA

2.2.1 Introduction to SEA

Statistical Energy Analysis (SEA) of coupled vibratory systems is born in the early 1960’s from the work of H. R. Lyon and G. Maïdanik. In this pre-computer time, availability of simple formulas for vibration prediction was a strategic objective to avoid unnecessary testing and establish robust specifications of random vibration environment of rocket and war ships.

Nowadays, these objectives, becoming civilian, remain valid. It is always preferable to provide at project start a good description of vibration environment resulting from the operating mode of a machine rather than suffer unforeseeable consequences requiring changes afterwards, always expensive and often ineffective when the design is frozen. Vibroacoustic forecasting methodologies are now developing in all areas of the industry and the research program is focusing on SEA use for complex timber framed system in building acoustics. Computing power is still limited compared to the size of discretized problems. Furthermore, the physical laws may change with frequency, requiring analysis by complex and lengthy finite-elements calculation. That is why the SEA analysis, despite or because of its simplifying assumptions is a must-to-have method for vibroacoustic engineers.

2.2.2 Energy balance in coupled oscillators

A building may be split into various elementary components. These components such wall, floor, mainframe, acoustic volume, are dynamical objects showing resonances. Some resonances are local to the objects; some others are global. In a full building the global resonances are for example the first bending modes of the building, the modes which involve a global dynamical phased motion of the stairs. The various walls are cross-coupled through the global motion. Each wall will exhibit local motion due to short wavelength waves that propagate inside the wall and are reflected at wall boundary creating local wall resonances depending only on wall characteristics. These modes are local modes.

Each mode is associated to a resonance frequency. A mode is mathematically interpreted as one-degree-of-freedom oscillator described by its mass and its stiffness, modelled as a spring as seen in figure 2.5. During the oscillatory motion the stiffness is storing potential energy while the mass is storing kinetic energy. Because the mass is attached to the ground by the intermediate of the spring, the resonance is interpreted as periodic exchange of potential and kinetic energy inside the oscillator. If a dissipative force is applied to the mass motion through a dashpot producing a force proportional to the velocity of the mass, a fraction of potential and kinetic energies will be per cycle of vibration dissipated as heat by the "viscous" force.

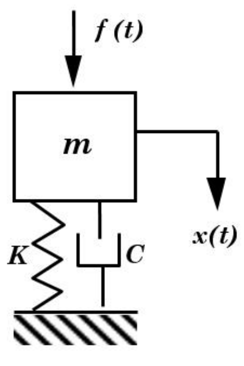

Figure 2.5. Mass-spring oscillator

The Newton's law applied to the oscillator motion states that the inertial force due to acceleration of the mass is equal to sum of external forces which are the spring force $-Kx$- and the dashpot force $-C\dot{x}$, x symbolizing the mass motion in function of time and $\dot{x}$the velocity, derivation of motion vs. time indicated by the dot point. The acceleration $\ddot{x}$ being written with a double dot .

$$m\ddot{x} + Kx + C\dot{x} = f(t)$$

Solution of this equation in frequency domain provides the resonance frequency f_0 of the oscillator

$$f_0 = \frac{1}{2\pi}\sqrt{\frac{K}{m}}$$

If any force oscillating in the vicinity of f_0 is applied to the oscillator, the mass motion will be amplified and the amount of amplification is depending on the amount of dissipation, i.e. on the value of the C coefficient.

In buildings, the applied forces are generally random. A random signal can only be described by statistics. In dynamical problems, a random signal is characterized by its mean squared value over some time lag T (RMS) to which is associated in frequency domain its power spectral density (PSD). The PSD corresponds to the decomposition of RMS value over frequency domain.

If a random force is applied to a mass-spring oscillator, some remarkable results can be demonstrated. First the mean potential energy (over time)

$$E_p = \frac{1}{2}K\left\langle x^2 \right\rangle_T$$

is exactly equal to mean kinetic energy

$$E_k = \frac{1}{2}m\left\langle \dot{x}^2 \right\rangle_T$$

leading to a description of energy stored in the oscillator by a single term: its total energy

$$E = E_p + E_k$$

Second, the mean energy dissipated by the dashpot force is proportional to the total energy

$$P_{diss} = 2\pi f_0 \eta E = \omega_0 \eta E$$

η is the dissipation loss factor (DLF) equal to $\dfrac{C}{m \cdot \omega_0}$

Third the mean injected power P_{inj} delivered by the force is independent of oscillator motion.

$P_{inj} = \dfrac{S_0}{2m}$ where S_0 if the force PSD.

Therefore, it leads to a power balance equation describing the dynamical response of mass-spring system as the whole injected power has to be converted into heat i.e. into dissipated power

$$P_{in} = P_{diss} = \eta\omega_0 E$$

The energy of the oscillator in function of force PSD is then given by

$$E = \frac{S_0}{2m\eta \cdot \omega_0}$$

Now, consider two oscillators excited by random force cross-coupled by non-dissipative elastic, inertial or gyroscopic forces. These forces are induced by some local stiffness, mass or gyroscopic coefficients at the junction between the two oscillators coupling their motion. In that case, Lyon and Maïdanik have shown that the steady-state power exchanged by the two oscillators through the coupling is found proportional to the difference of their total energy such as:

$$P_{12} = \beta_{12}(\omega_1, \omega_2)\left(E_1 - E_2\right)$$

with β_{12} the coefficient of proportionality depending on both resonance frequencies of the oscillators.

2.2.3 General SEA Energy balance equations

This result can be extended to the coupling of continuous dynamical systems. As β_{12} coupling term is large only when oscillators have nearby radian resonance frequencies ω_1 and ω_2 , the frequency domain to analyze is first truncated into frequency bands of width $\Delta\omega$ and only modes of system 1 and 2 resonating in this band are taking into account (modes having far away resonance frequency exchange very little power). We assume there are N_1 resonances in systems 1 and N_2 in system 2 in $\Delta\omega$.

There are $N_1 N_2$ pairs of modes exchanging their energy in the coupling. From this the exchanged power is statistically expressed as

$$P_{12} = N_1 N_2 \left\langle \beta_{12}(\omega_i, \omega_j) \right\rangle \left(\varepsilon_1 - \varepsilon_2 \right)$$

where $\left\langle \beta_{12}(\omega_i, \omega_j) \right\rangle$ is the mean coupling coefficient of a particular mode *i* of system 1 with a particular mode *j* of system 2 and is symmetrical, $\beta_{12} = \beta_{21}$ due to the linearity of the dynamical equations.

ε_1 and ε_2 are the mean energy of a particular mode in resp. systems 1 and 2.

Because the modes in system 1 and 2 are assumed to be local modes, the total energy carried by system 1 and 2 is given by the sum of modal energies in the band i.e.:

$$E_1 = N_1 \varepsilon_1 \qquad E_2 = N_2 \varepsilon_2$$

In the analysed band $\Delta\omega$, the power balance related the total energies is found equal to:

$$P_{1inj} = P_{1diss} + P_{12} = \left\langle \eta_1 \right\rangle \omega N_1 \frac{E_1}{N_1} + N_1 N_2 \left\langle B_{12} \right\rangle \omega \left(\frac{E_1}{N_1} - \frac{E_2}{N_2} \right)$$
$$P_{2inj} = P_{2diss} + P_{21} = \left\langle \eta_2 \right\rangle \omega \frac{E_2}{N_2} + N_1 N_2 \left\langle B_{12} \right\rangle \omega \left(\frac{E_2}{N_2} - \frac{E_1}{N_1} \right)$$

We now can clearly see the modal statistics introduced in the SEA power balanced equations. The damping loss factor is described as the mean damping over modes in $\Delta\omega$, the mean mode in the band assumed to oscillate at the central radian frequency of the band ω. The coupling coefficient is expressed as the mean coupling over the modal series at ω and modal energy is simply obtained as total energy divided by the number of modes.

In SEA, to be conform to the description of dissipation loss factor interpreted as the fraction of total energy dissipated into heat, the modal coupling coefficient is replaced by the coupling loss factor (CLF) which represents the fraction of energy lost in the coupling by the system.

Per definition $P_{12} = \eta_{12} \omega E_1 \Rightarrow \eta_{12} = N_2 \left\langle B_{12} \right\rangle$

The power balance in function of total energy and CLF's is at the end given by next equations known as the SEA power balance equilibrium.

$$P_{1inj} = \eta_1 \omega_1 E_1 + \eta_{12} E_1 - \eta_{21} E_2$$
$$P_{2inj} = \eta_2 \omega_2 E_2 + \eta_{21} E_2 - \eta_{12} E_2$$

From symmetry of $\left\langle B_{12} \right\rangle$ comes the reciprocity relationship between CLF

$$\eta_{12} N_1 = \eta_{21} N_2$$

This is a useful formula as knowing the CF in the direction 12, provides the CLF in direction 21 as soon as the modal count in the band is known.

When coupling more than two subsystems together, previous equations are put into a matrix form, leading the matrix expression of the SEA power balance:

$$\omega\begin{bmatrix} \eta_1+\sum_{j_1}\eta_{1j} & \cdots & -\eta_{i1} & \cdots & -\eta_{N1} \\ \cdots & \cdots & & \cdots & \cdots \\ -\eta_{1i} & \cdots & \eta_i+\sum_{j_i}\eta_{ij} & \cdots & \cdots \\ \cdots & \cdots & \cdots & \cdots & \cdots \\ -\eta_{1N} & \cdots & \cdots & \cdots & \eta_N+\sum_{j_N}\eta_{ij} \end{bmatrix}\cdot\begin{bmatrix} E_1 \\ \cdots \\ E_i \\ \cdots \\ E_N \end{bmatrix}=\begin{bmatrix} P_1 \\ \cdots \\ P_i \\ \cdots \\ P_N \end{bmatrix}$$

Solving an SEA problem is then sequentially performed by

- Defining series of frequency band containing several resonances and covering the frequency range to span
- Defining a partition into subsystems that guaranties previous condition on the presence of resonances
- Estimating the components of injected power vector P_i*'s* in each bands. It involves converting physical forces applied to the various subsystems into power through some function of frequency (driving point mobility) which only depends of the intrinsic property of the excited medium.
- Estimating CLF's between coupled subsystems. This is generally achieved using wave transmission theory between infinite coupled medium by decomposing modes into waves.
- Estimating appropriate DLF in each subsystem, most of the time by measurement of intrinsic material dissipative properties.
- Constructing the Loss Factor matrix relating energy to power.
- Solving the linear problem $\eta E = P/\omega$ in each band centered around ω to get the energy vector.

2.3 European and international standards

The European standard series EN 12354 has been under revision and will incorporate a building performance prediction method for lightweight wood-based building. Furthermore, this new version of the European standard series EN 12354 is going to become an international standard series ISO 12354 (and replace the current ISO 15712).

The prediction method has been discussed and mostly defined during COST Action FP0702. When wood or steel frame lightweight constructions are investigated, both current standardized methods, EN 12354-1 and -2 for predicting building acoustic performances, and the related standardized laboratory measurement methods for characterizing building elements and their junctions have to be reconsidered [23].

The most direct method of predicting the acoustic performance is to establish a database of measured flanking sound reduction indices for different combinations of lightweight elements and junctions. The measurement of individual flanking transmission path can be performed in a dedicated facility by using sound intensity and/or by acoustically shielding all of the flanking elements not involved in the path considered. The direct prediction method is being used by NRC in Canada [24], [25] and by EMPA in Switzerland. This method has the advantage of using measured values. However, a major difficulty with this approach is the extension to the low frequencies, where adequate shielding is difficult. Another problem is the impossibility to predict the performance of constructions, which have not already been tested.

The second (indirect) method consists in deducing the flanking sound reduction indices of lightweight building constructions from the performance of the elements; it involves adapting the existing EN 12354 method, to the presence of non-uniform vibration fields, relatively high damping (high internal loss factors) and non-resonant fields [26]. Much work has been carried out to modify the EN 12354 framework in order to take into account these particularities [26]–[30].

The prediction method in the current version of the standard for evaluating building acoustic performance is valid for “Type A” elements. These Type A elements are defined by a structural reverberation time that is primarily determined by the connected elements (up to at least the 1 000 Hz one-third-octave band), and a decrease in vibration level of less than 6 dB across the element in the direction perpendicular to the junction line (up to at least the 1000 Hz one-third-octave band). Massive wood panels (such as CLT) construction fall into this category. Plasterboard/timber cladding on timber or metal frames are “Type B” elements; a Type B element is defined as any element that is not a Type A element.

In the section below, the prediction method for evaluating the building acoustic performance is described for Type B elements construction.

The prediction of the flanking path is briefly recalled below. Following EN 12354 prediction model for airborne and impact sound insulation [31], the flanking sound reduction index R_{ij} and the flanking impact sound level $L_{n,ij}$ from element i in the source room to element j in the receiving room can be expressed as:

$$R_{ij} = \frac{R_i^* + R_j^*}{2} + \Delta R_i + \Delta R_j + \frac{D_{v,ij} + D_{v,ji}}{2} + 10\log\frac{S_s}{\sqrt{S_i S_j}} \,,$$

$$L_{n,ij} = L_{n,ii} - \Delta L_i + \frac{R_i^* - R_j^*}{2} - \Delta R_j - \frac{D_{v,ij} + D_{v,ji}}{2} - 10\log\sqrt{\frac{S_i}{S_j}} ,$$

where R_i^* and R_j^* are sound reduction indices, referring to resonant transmission only of the elements considered (linings with ΔR_i, ΔR_j and ΔL_i); $D_{v,ij}$ is the vibration level difference between elements i and j, when element i is mechanically excited; S the element surfaces (S_s for the element separating the two rooms considered) and $L_{n,ii}$ the normalized impact sound level of element i.

An expression for the correction of measured sound reduction index R values that includes both resonant and forced transmissions has been proposed by the authors in [4-5]; it is based on the radiation efficiencies of the element obtained with an airborne excitation, denoted σ_a, and a structural excitation, denoted σ_s. It is given by

$$R^* = R + 10\log\left[\frac{\sigma_a}{\sigma_s}\frac{1-\sigma_s}{1-\sigma_a}\right] \approx R + 10\log\left(\frac{\sigma_a}{\sigma_s}\right),$$

This correction is more important at frequencies much smaller than the critical frequency of the element considered, i.e. in the low frequency range for lightweight elements. In the case of double elements with cavity, Equation above overestimates the correction at frequencies close to the cavity resonance.

This correction can be evaluated from measured radiation efficiencies on different type of lightweight elements (including floor and wall) [26], [27]. There is no standardized method available to determine these radiation factors yet. However, recent measurements, using the method proposed in [23], have indicated that in case of double elements with cavity the correction is small or negligible, while for elements without cavity (i.e. single leaf wall often framed elements), the correction seems to be reasonably independent of the type of element and around 8 dB below the critical frequency.

Thus, an estimate of the correction is given by the following:

- no correction for elements separated by one or two cavities;
- a correction of 8 dB for single, homogeneous or layered, wood or steel frame elements (i.e. without a cavity) below the critical frequency only.

The vibration level difference $D_{v,ij}$ between element i and j, when element i is excited, can be measured in-situ and also in laboratory for different types of junctions in order to have a data base. CSTB has proposed to implement classes of junction with average vibration level difference for use in the prediction model [26], [27]. Finite element modelling can also be utilized to determine the vibration level difference [31].

The normalized direction-averaged vibration level difference has been proposed as a new junction invariant; it is defined by

$$\overline{D_{v,ij,n}} = \frac{D_{v,ij} + D_{v,ji}}{2} + 10\log\left[\frac{l_{ij}l_0}{\sqrt{S_{m,i}S_{m,j}}}\right],$$

where l_{ij} represents the length of the junction between elements i and j, l_0 is the reference length of (l_0 = 1 m) and $S_{m,i}$ and $S_{m,j}$ are the measurement surface areas, equal or smaller that the elements i and j surface areas.

With this expression of the normalized direction-averaged vibration level difference, the flanking sound reduction index R_{ij} and the flanking impact sound level $L_{n,ij}$ from element i in the source room to element j in the receiving room can be rewritten as

$$R_{ij} = \frac{R_i^* + R_j^*}{2} + \Delta R_i + \Delta R_j + \overline{D_{vs,ij,n}} + 10\log\frac{S_s}{l_0 l_{ij}},$$

$$L_{n,ij} = L_{n,ii} - \Delta L_i + \frac{R_i^* - R_j^*}{2} - \Delta R_j - \overline{D_{vs,ij,n}} - 10\log\frac{S_s}{l_0 l_{ij}},$$

Specific data characterizing junctions between lightweight wood-based elements, i.e. the normalized direction-averaged vibration level difference, had to be introduced in the new version of the standard. An important particularity of lightweight buildings is the large variety of building elements (using different types of boards, studs, joists, etc…) and of junctions between these elements. Therefore, it has been proposed to group junctions between elements into a small number of categories for T and X junctions, characterized by mean values. The frequency dependency, showed in the collected data, is stronger than for heavy homogeneous elements, and has been taken into account in the empirical relations calculating the normalized direction-averaged vibration level difference. Junctions between Cross-Laminated Timber (CLT) building elements are also introduced. Although these junctions are characterized by the vibration reduction index, they are not rigid and the K_{ij} values are higher than for rigid junctions and show a significant dependency on frequency. The classification of such junctions has been presented in [32] and included in the new version of the standard.

2.3.1 Silent Timber Build

As mentioned in the version of the standard ISO EN 12354, it is recommended to gather data concerning junctions especially to fit specificities encountered in differents countries. In this project some measurements on junctions of CLT panels have been conducted. Indeed, measurements performed by Rothoblass allow to complete junction characteristics between CLT elements by evaluating the following aspects :

- 7 different CLT manufacturers
- L, T, X vertical and horizontal junctions
- influence of kind and number of screws
- influence of kind and number of angle brackets
- influence of kind and number of hold-downs
- use of resilient interlayers

All the data is available in the “Flanksound report” accessible on the following internet address http://www.rothoblaas.com/catalogues-rothoblaas and on www.silent-timber-build.com. In the future when the ISO EN 12354 is updated, these data will certainly be incorporated in the new version of the standard.

Furthermore, the results regarding modeling the walls and floors acoustic performance will be used in the evaluation of the building acoustic performance following the new ISO EN 12354 prediction method before the building is constructed and even before the walls and floors are tested in the laboratory to monitor their acoustic performance.

Moreover, the tools developed in the project will allow to evaluate the sound radiation factor which has an important role in the flanking transmission evaluation; if a measurement standard is in preparation it will be of importance to be able to predict it in order to avoid too many and too cumbersome measurements.

3 Results

3.1 FEM

3.1.1 Floor C1 from ISO 10140-5

Detailed vibration and acoustics measurements performed on lightweight reference floor C1 (see figure 3.1) from ISO 10140-5 by IBP within the AcuWood project have been made available to the Silent Timber Build project partners. Such design is representative of standard German prefabricated floors in single family houses, in which there is no requisite on sound insulation. As a first step, the results from the low frequency prediction models are compared to experimental data; a first model and comparisons were presented in [10].

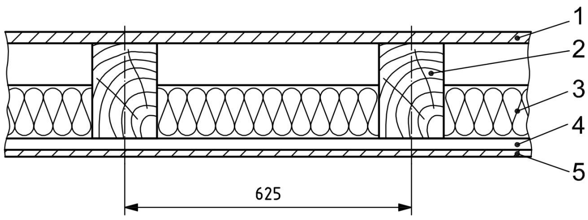

1: Floor plate wooden chip board with 22±2 mm thickness, screwed into beams every 300 ±50 mm
2: Wooden beams with 120 mm width and 180 mm height
3: 100 mm mineral wool, flow resistance between 5 and 10 kPa s/m² according to ISO 9053
4: Wooden battens with 24 mm width and 48 mm height and with 625 mm distance screwed into the beams
5: 12,5 mm plasterboard, densityity 800 ±50 kg/m³, screwed into the battens every 300 ±50 mm)

Figure 3.1: Sectional view of C1 floor (extracted from [6])

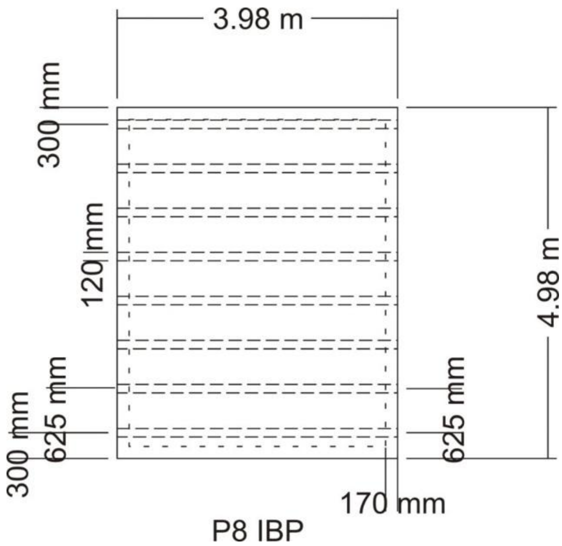

Figure 3.2: Top view onto the floor with wooden beams provided by IBP. The beams are drawn with dotted lines. The dotted line with short dots depict the concrete console, where the beams are supported (left and right side of figure)

Finite element model

A finite element model of the floor C1 is constructed using geometrical and physical data and constraints given in the figures 3.1 and 3.2. The modelling framework and associated choices and hypothesis can be summed up as follow:

- Linear homogeneous elastic, acoustic and porous domains
- Perfect idealized boundary and assembly conditions (no flexibility)
- Unknown elastic properties of structural materials chosen according to Refs. [1], [33]–[35]

Thus, physical properties for the different layers are chosen according to tables 3.1, 3.2 and 3.3. Moreover, the properties of the fibrous poroelastic materials are chosen such as por. 0.96, flow res. 7500 N.S/m^4, tort. 1.1, vcl 50 µm, tcl 150 µm and density 25 kg/m^3.

Chipboard and plasterboard layers are modelled as slender solids in using first order shear deformation theory (rotational inertia and transvers shear are taken into account) and a normal drilling degree of freedom. Wooden primary frame and battens are modelled as tridimensional elastic solids. Acoustic cavities are modelled as tridimensional acoustic fluids with pressure as primary variable. Fibrous poroelastic components are modelled as tridimensional equivalent fluids with limp frame, using pressure as primary variable. According to the results presented in [3], [36], [37] only the inertial effects of the fibrous skeleton are taken into account.

In terms of boundary conditions, lateral displacements of the chipboard and gypsum layers are blocked. Moreover, primary wooden beams lay (simply supported conditions) on a rigid support. Both chipboard and gypsum layers are punctually clamped (rigidly tied) to wooden frame elements every 300 mm.

ρ	El	Er	Et	Gtl	Glr	Grt	nu_{rt}	nu_{lr}	nu_{lt}
450 kg/m^3	10.9 Gpa	0.3 Gpa	0.3 Gpa	0.7 Gpa	0.7 Gpa	0.05 Gpa	0.1 Gpa	0.1 Gpa	0.1 Gpa

Table 3.1 : Wood frame chosen mechanical properties

ρ	E_x	E_y	nu_{xy}	G_{xy}	G_{yz}	G_{xz}
700 kg/m^3	2.88 Gpa	2.88 Gpa	0,3	1.1 Gpa	1.1 Gpa	1.1 Gpa

Table 3.2 : Chipboard chosen mechanical properties

ρ	E_x	E_y	nu_{xy}	G_{xy}	G_{yz}	G_{xz}
800 kg/m^3	2.8 Gpa	2.8 Gpa	0,2	1,16 Gpa	1.16 Gpa	1.16 Gpa

Table 3.3: 12.5 mm plasterboard chosen mechanical properties

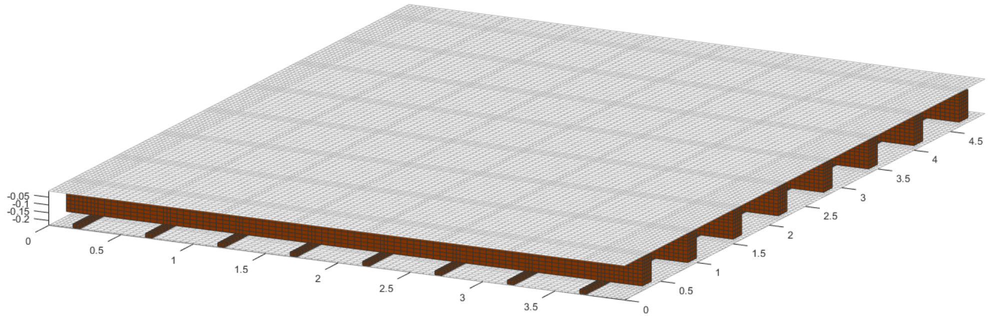

Figure 3.3 : Finite element mesh of the structural components

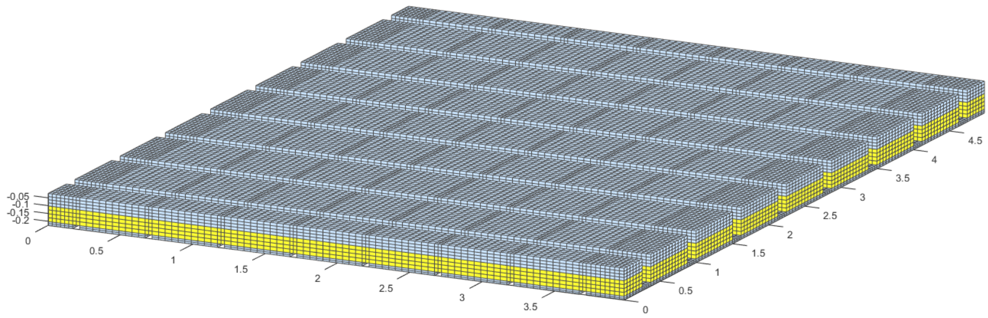

Figure 3.4 : Finite element mesh of the acoustic and poroelastic domains

Figures 3.3 and 3.4 display finite element meshes of structural, acoustic and poroelastic domains which are constructed in using the minimal criterion of 20 elements per meter.

Acoustic room model

According to the methodologies presented in Sections FEM\Airborne sound insulation and FEM\Impact sound insulation, laboratory facilities are modelled as rigid parallelepiped rooms. It is then possible to construct *ad hoc* acoustic excitation and to evaluate radiated pressure fields. Model parameters are then the room dimensions and a frequency dependent reverberation time such as given in Figure 3.5. The latter is used for the construction of acoustic modal damping factors in the laboratory rooms that are, as a first approximation, consistent with experimental damping.

(a)

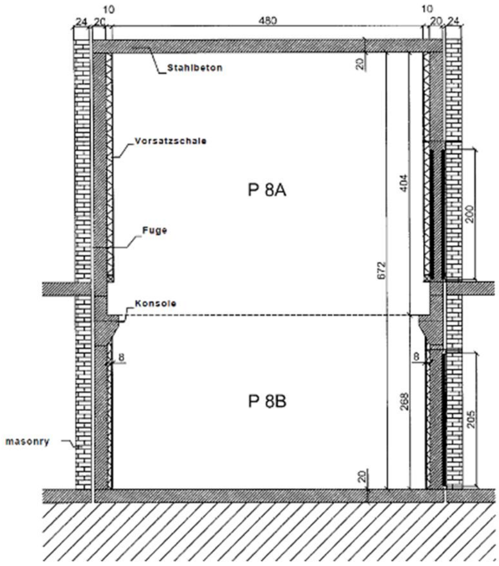

(b)

f [Hz]	t [s]	f [Hz]	t [s]
20	2,17	**400**	0,53
25	1,76	**500**	0,54
31,5	1,41	**630**	0,58
40	1,39	**800**	0,6
50	0,87	**1000**	0,65
63	0,46	**1250**	0,58
80	0,33	**1600**	0,61
100	0,53	**2000**	0,61
125	0,47	**2500**	0,59
160	0,51	**3150**	0,57
200	0,6	**4000**	0,56
250	0,52	**5000**	0,5
315	0,57		

Figure 3.5: (a) Sectional view of the laboratory P8 provided by IBP. The wooden floor construction was installed on the console, separating the laboratory into two rooms. (b) Reverberation times for the receiving room

Airborne sound insulation

According to the methodology introduced in section FEM\Airborne sound insulation the external excitation of the floor system is constructed in using a rigid parallelepiped room model in which monopoles can be successively introduced for the generation of a sound pressure field. Figure 3.5 gives the dimensions of test facilities and reverberation time that were used for the construction of the model. Due to the high sensitivity of predicted results to external excitation parameters (in particular source position) the evaluation of airborne sound insulation is performed in using 1000 source positions. A uniform probability distribution over the volumes is used for the source positions. Then, 98% confidence regions can be evaluated from the quantile method.

Figure 3.6 compares such confidence regions in narrow band and third octave band with experimental data in third octave band. It can be observed that confidence regions, resulting from varying source position, get narrower as frequency increases. Indeed, acoustic fields become more diffuse so that source localization loses importance. Interval width then go from up to 20 dB around 20 Hz to 10 dB past 100 Hz. Moreover, a strong modal behavior can be observed below 100 Hz on narrow band values as sound insulation promptly decreases near singular frequencies. Other than that, predicted and experimental magnitudes and tendencies appear as consistent with each other, at least past 100 Hz.

However, energetic averaging of predicted values over the various source positions cannot get close to experimental sound reduction values. Such average would in fact yield the lowest (but safe) bound of the confidence region.

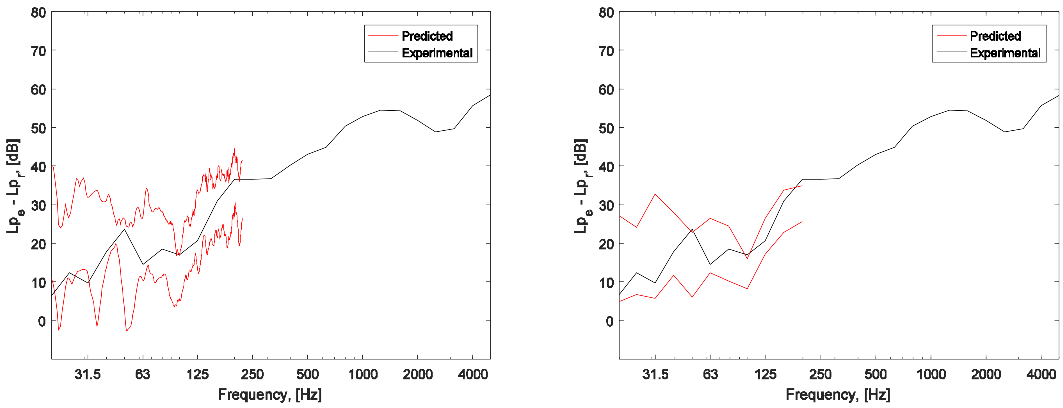

Figure 3.6 : Comparison of measured sound pressure level difference and computed confidence region obtained for 1000 uniformly distributed random source positions

Impact sound insulation

According to the methodology introduced in section FEM\Impact sound insulation the external excitation of the floor system is constructed in using a tapping machine model. Preliminary computations are then required in order to evaluate impact forces spectra at various hammer positions. Then, 100 tapping machine positions and orientations are randomly selected (uniform probability distribution) over the floor surface minus 50 cm from the boundaries, so that every tapping machine orientation is admissible. Then, the velocity field of the floor is then used in the rigid parallelepiped room model for the evaluation of impact sound level.

Figure 3.7 compares obtained confidence regions with experimental data in third octave band. It can be noted that below 50 Hz, the numerical prediction underestimate the effective impact sound level. Moreover, a prompt decrease of predicted sound pressure level can be observed in the 25 Hz octave band. In fact, a decrease is expected and corresponds to a minimum of magnitude for the overall tapping machine impact force. It was underlined in Section FEM\Impact sound insulation that the five impact hammers spectra were in phase every 10 Hz, consequently resulting in maxima of injected power at 20 and 30 Hz. However such a low level either means that 1) such a model is not good enough for the description of the mechanical excitation resulting from the standard tapping machine or there is some inaccuracy in 2) the floor model or 3) the room model. In particular, if the injected power is that low in reality, then mechanical or acoustical compliance should be higher to yield observed experimental values. Thus, it might be possible that in the model, not enough structural or acoustical resonances belong to the 25 Hz third octave band. Such resonance mispositioning can result from inadequate boundary conditions, assembly conditions or material properties.

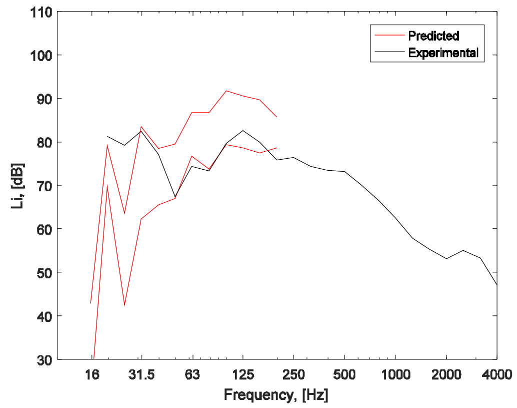

Figure 3.7: Comparison of measured sound pressure level and computed confidence region obtained for 100 uniformly distributed random tapping machine positions

Detailed measurements

In order to discriminate acoustic radiation and mechanical problems, local data (in the sense of spatially localised) was also provided by IBP. Thus, the aim is to validate the ability of the finite element model to predict the velocity distribution on top of the floor and on the ceiling for a given structural excitation, and in particular for the excitation constructed using the tapping machine model. Following, velocities were measured on various points of the floor system for a given position of the tapping machine. In particular, velocity levels were given in third octave band at 6 receiver positions on the top of the floor (in the sending room) and at 4 positions on the ceiling (in the receiving room). Figure 3.8 displays the respective positions of the tapping machine and accelerometers with respect to primary and secondary wood frame elements.

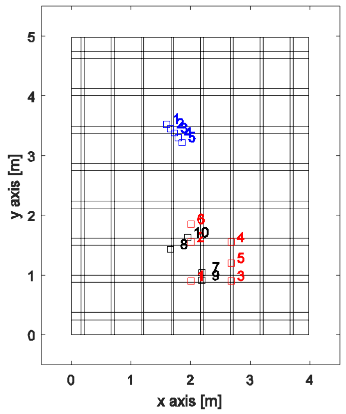

Figure 3.8: Tapping machine hammers (blue); accelerometers on top of the floor (red); accelerometers on the ceiling (black)

Figures 3.9 and 3.10 respectively compare predicted and measured velocity levels on top of the floor and on the ceiling. Globally, a 10 dB maximal difference can be observed. At this point, it should be noted that the finite element model was constructed in using *a priori* data (material properties, assembly conditions, boundary conditions etc) without updating. Moreover, the external excitation from the tapping machine was constructed from an *a priori* model (hammer mass, impact frequency, etc.). Finally, acoustic radiation was performed in using a rigid parallelepiped room model in which reverberation times were used, as a first approximation, to evaluate modal damping factors. Thus, given the complexity of the approach and the associated number of hypothesis, the prediction quality might be considered as satisfactory for a first step. In a future step, detailed narrow band information could allow to perform model updating and in particular to identify relevant boundary or assembly conditions.

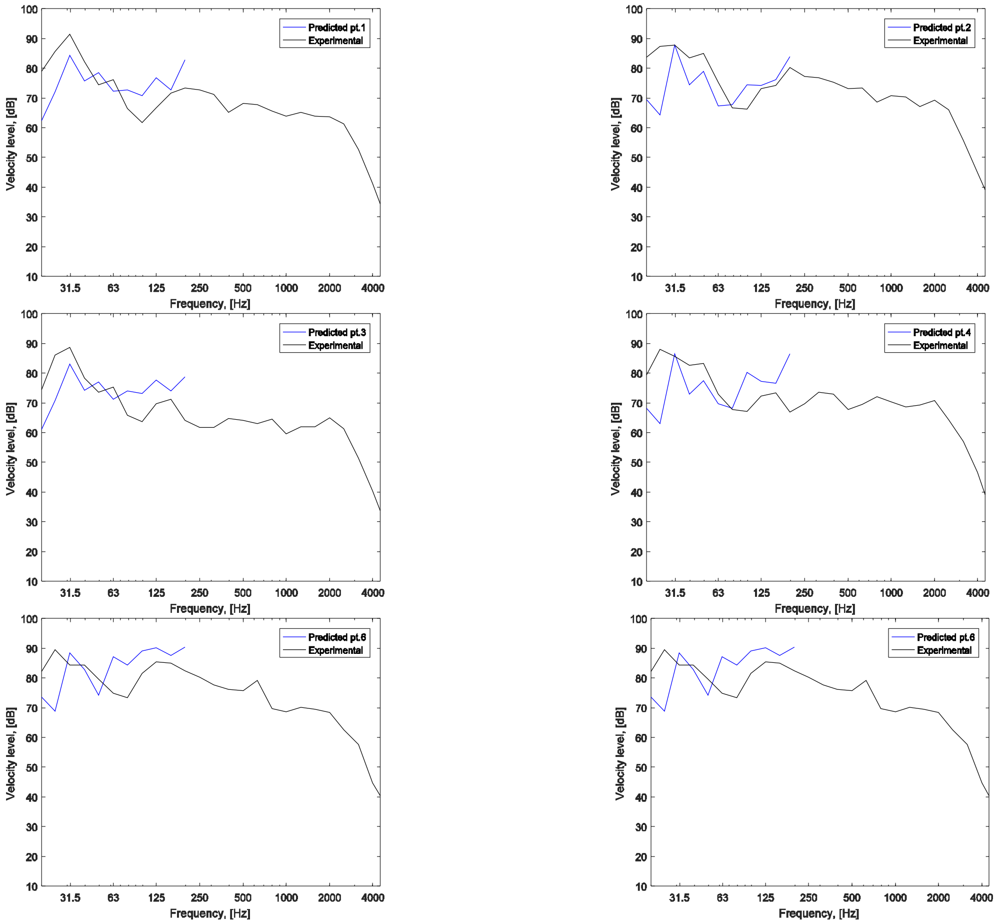

Figure 3.9: Velocity levels on top of the floor (ref. 8e-8 m/s)

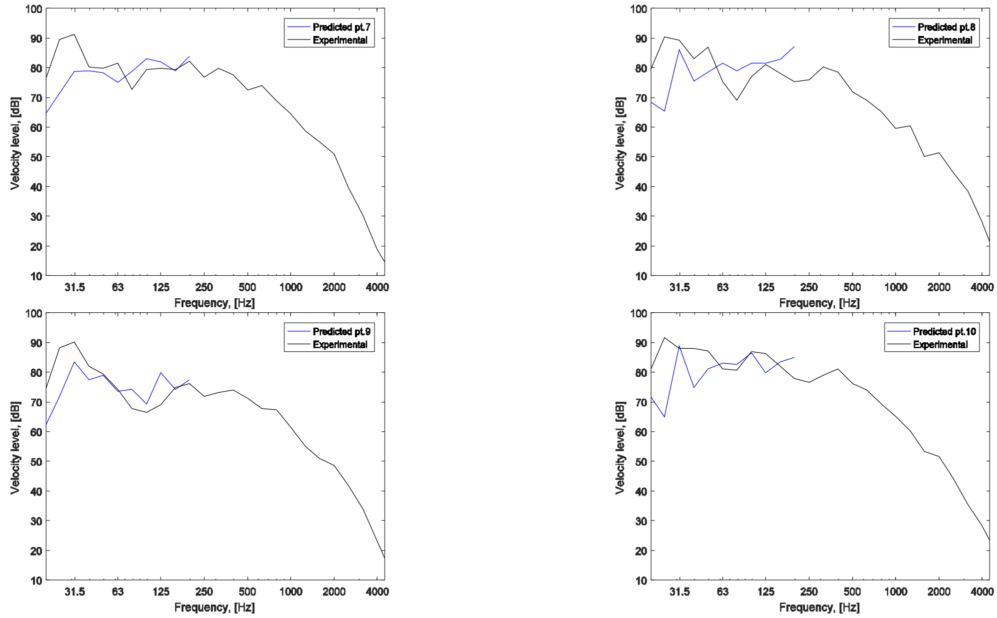

Figure 3.10 : Velocity levels on top of the ceiling (ref. 8e-8 m/s)

3.1.2 Bauer Holzbau floor series

In the following, four closely related floor designs are modelled. System complexity is increased step by step, going from the raw load bearing structure to a complex system including floating floor and ceiling. Indeed, few information is available for the direct construction of a relevant numerical model for a complex system. The knowledge of material properties, component connections or boundary conditions is incomplete and subjected to conjectures. Then, a step by step modelling process with experimental comparisons is of great help to discriminate the influence of hypothesis and unknowns. In the following, acoustic quantities as well as point velocities are compared to experimental values.

Moreover, identical hypothesis and treatment of boundary conditions, assembly conditions and structural damping are chosen between the modelling of the C1 floor and the present floor series. Indeed, a modelling process that aims to yield a predictive methodology should be repeatable and consistent from one problem to another. It should be noted that those modelling choices result in fact from a feedback process. Several modelling hypotheses were compared for the different systems (free/simply supported/clamped boards, surface/line/point board connections between boards and beams etc.) and only the one set that was the most consistent with experimental values was retained.

Raw floor

The 4 m x 5 m raw floor made up of an OSB layer on top of wooden beams is the core of every other floor provided by project partner Bauer Holzbau. Thus, in order to be able to model floors of quickly increasing structural complexity it appeared as necessary to first consider the raw structure. Indeed, few information is available for the direct construction of a relevant numerical model. The knowledge of material properties, component connections or boundary conditions is incomplete and subjected to conjectures. Then, a step by step modelling process with experimental comparisons is of great help to discriminate the influence of hypothesis and unknowns.

Moreover, the discretization process requires fewer degrees of freedom due the structural simplicity of this floor. The numerical complexity is lowered and it is possible to solve the vibro-acoustic problem at higher frequencies in using the finite-element method. Herieinafter, airborne and impact problems are solved up to 400 Hz.

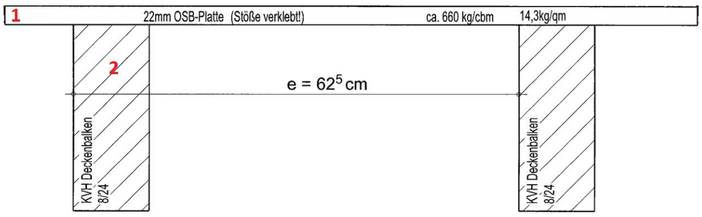

1: Floor plate OSB with 22 mm thickness, density 660 kg/m³
2: Wooden beams with 80 mm width and 240 mm height, distance between beams 625 mm

Figure 3.11: Sectional view of the raw floor

Finite element model

A finite element model of the raw floor is constructed using geometrical and physical data and constraints given in figure. 3.12. Thus, physical properties for the different layers are chosen according to tables 3.4 and 3.5. Oriented strand boards are modelled as slender solids in using first order shear deformation theory (rotational inertia and transvers shear are taken into account) and a normal drilling degree of freedom. Wooden beams are modelled as tridimensional elastic solids. In terms of boundary conditions, lateral displacements of the strand board layer are blocked. Moreover, wooden beams lay (simply supported conditions) on a rigid support. OSB layer is punctually clamped (rigidly tied) to wooden frame elements every 300 mm.

ρ	El	Er	Et	Gtl	Glr	Grt	nu_{rt}	nu_{lr}	nu_{lt}
450 kg/m^3	10.9 Gpa	0.3 Gpa	0.3 Gpa	0.7 Gpa	0.7 Gpa	0.05 Gpa	0.1 Gpa	0.1 Gpa	0.1 Gpa

Table 3.4 : Wood frame mechanical properties chosen for the simulation

ρ	E_x	E_y	nu_{xy}	G_{xy}	G_{yz}	G_{xz}
650 kg/m^3	5 Gpa	5 Gpa	0,14	2.19 Gpa	2.19 Gpa	2.19 Gpa

Table 3.5 : OSB mechanical properties chosen for the simulation

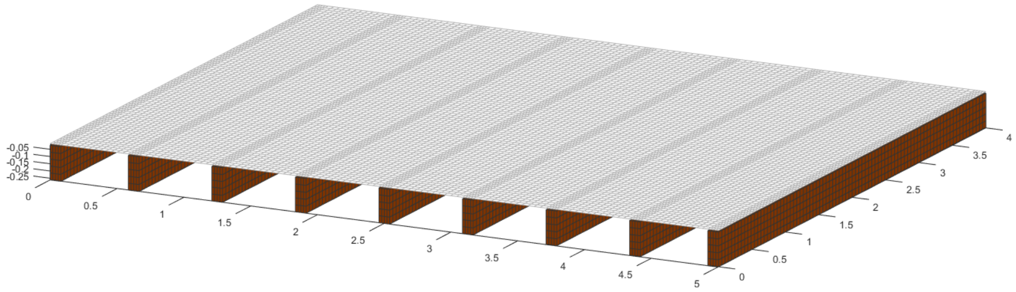

Figure 3.12 : Finite element mesh of the structural components

Figure 3.12 displays the finite element mesh of structural components, which is constructed in using the minimal criterion of 20 elements per meter.

Acoustic room model

The laboratory setup for Bauer Holzbau's measurement series is similar to the one deployed for the standard C1 floor. However reverberation time was measured and provided by IBP for each tested configuration. In the present case it is and given in Figure 3.13 and used in following applications for the evaluation of rooms modal damping.

(a)

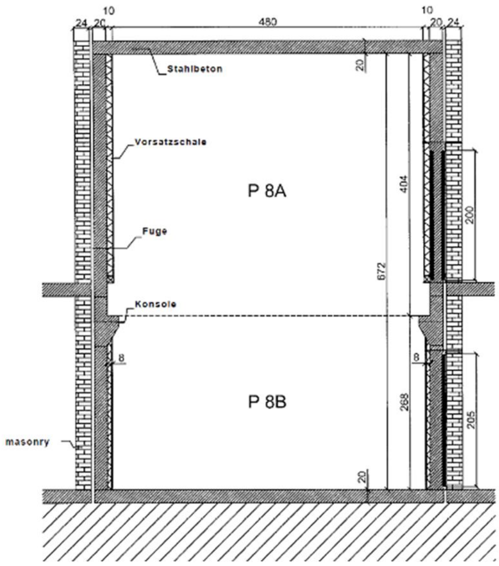

(b)

f [Hz]	t [s]	f [Hz]	t [s]
20	2,25	**400**	1,23
25	2,52	**500**	1,36
31,5	3,13	**630**	1,20
40	2,04	**800**	1,24
50	0,89	**1000**	1,12
63	1,05	**1250**	1,08
80	0,68	**1600**	1,12
100	0,90	**2000**	1,12
125	1,35	**2500**	1,10
160	1,10	**3150**	1,03
200	1,08	**4000**	0,89
250	1,40	**5000**	0,83
315	1,51		

Figure 3.13: (a) Sectional view of the laboratory P8 provided by IBP. The wooden floor construction was installed on the console, separating the laboratory into two rooms. (b) Reverberation times for the receiving room

Airborne sound insulation

According to the methodology introduced in section FEM\Airborne sound insulation the external excitation of the floor system is constructed in using a rigid parallelepiped room model in which monopoles can be successively introduced (1000 source positions) for the generation of a sound pressure field. Then, it is possible to construct confidence regions for the evaluated performance indicator.

Figure 3.14 compares such confidence regions in narrow band and third octave band with experimental data in third octave band. It can be noted that the first insulation dip (corresponding to the coincidence in frequency of the first room and floor resonances) is well predicted. However, the next two dips appear to be predicted at lower frequencies in comparison with experimental values. Assuming that they correspond to the very same phenomena, this could be interpreted as a lack of stiffness or a surplus of mass in the numerical model. Moreover, the shift is more and more apparent as frequency increases. This illustrates well known model uncertainty propagation problems in the medium frequency range [38]. Overall, a satisfactory level of prediction is achieved below 200 Hz for the given amount of input information.

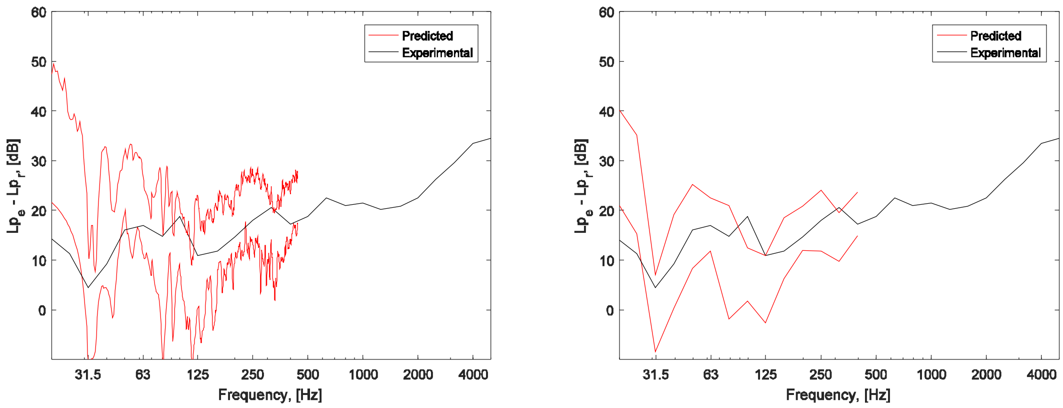

Figure 3.14 : Comparison of measured sound pressure level difference and computed confidence region obtained for 1000 uniformly distributed random source positions

Impact sound insulation

According to the methodology introduced in section FEM\Impact sound insulation the external excitation of the floor system is constructed in using a tapping machine model and 100 randomly selected tapping machine positions. Then, the velocity field of the floor is then used in the rigid parallelepiped room model for the evaluation of impact sound level.

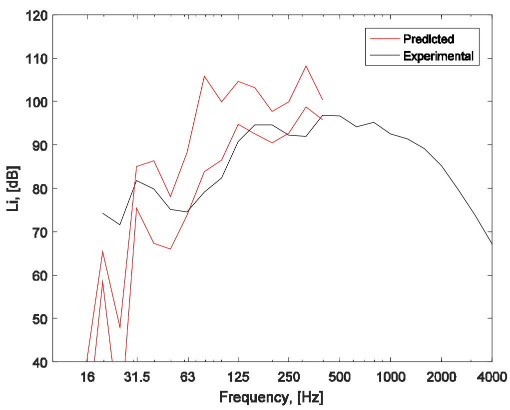

Figure 3.15: Comparison of measured sound pressure level and computed confidence region obtained for 100 uniformly distributed random tapping machine positions

Figure 3.15 compares obtained confidence regions with experimental data in third octave band. As for the C1 floor (Figure 3.7), the impact noise level is underestimated at very low frequencies (20 and 25 Hz third octave bands). However, the shift towards low frequencies of predicted peaks, in comparison with experimental values, is consistent with the observations made for airborne sound insulation. Suitable updated model (regarding boundary conditions for example) would consequently equally improve the prediction quality for airborne as well as impact sound insulation.

Detailed measurements

Detailed measurements were provided in order to enrich the knowledge about the purely mechanical behavior of lightweight floor systems. In particular, input and transfer mobility were measured, as well as velocity of given points under tapping machine excitation. Figure 3.16 gives shows accelerometers as well as tapping machine hammers positions.

As a first step, predicted input and transfer mobilities are compared to experimental values. In particular, input mobilities were provided for point 1, 2 and 3, that is to say two points on OSB right on top of a beam and one in between. Figures 3.17 (a), (b) and (c) show the comparison of predicted and experimental input mobilities. Thus, the numerical model underestimates the input mobility on top of beams but gives a rather accurate level for the point between beams. This means that, despite having considered point connections between boards and beams, the local board stiffness is overestimated. This, however, has few influence on transfer mobilities between an excitation on top of a beam and an observation between beams as shown with Figures 3.17 (g) and (i).

Moreover, it can be observed that below 31.5 Hz, mobilities are systematically underestimated. Then, it can be understood that, for any acoustic or structural excitation, velocity levels below 31.5 Hz will be underestimated. This observation is consistent with the performance overestimation obtained in such very low frequency range. It can be suspected that the simply supported boundary conditions of the beams in the model yield too much stiffness and that an appropriate mounting flexibility could improve the prediction at very low frequencies.

The most interesting output from those narrow band measurements is perhaps the high modal density and damping that can be observed below 200 Hz. Indeed, below 50 Hz, it can be seen that the first global modes are in fact very damped/little responding. Thus, it can be imagined that structural connections are not stiff enough to yield an actual global modal behavior. In fact, the simple raw floor, which is made up of quite stiff structural load bearing components, doesn't display a strongly marked modal behavior even in the lowest frequency range. Then, increasing complexity will mostly add mass and damping thus definitely settling the system in a "medium frequency like" behavior.

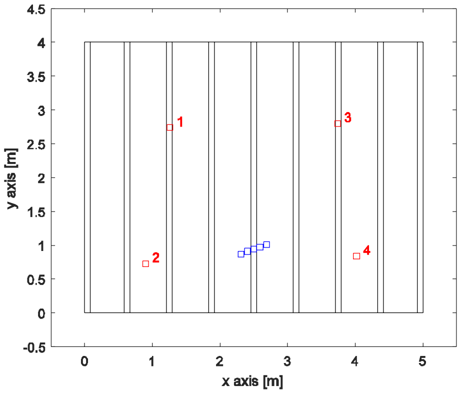

Figure 3.16 : Tapping machine hammers (blue); accelerometers on top of the floor (red); accelerometers on the ceiling (black)

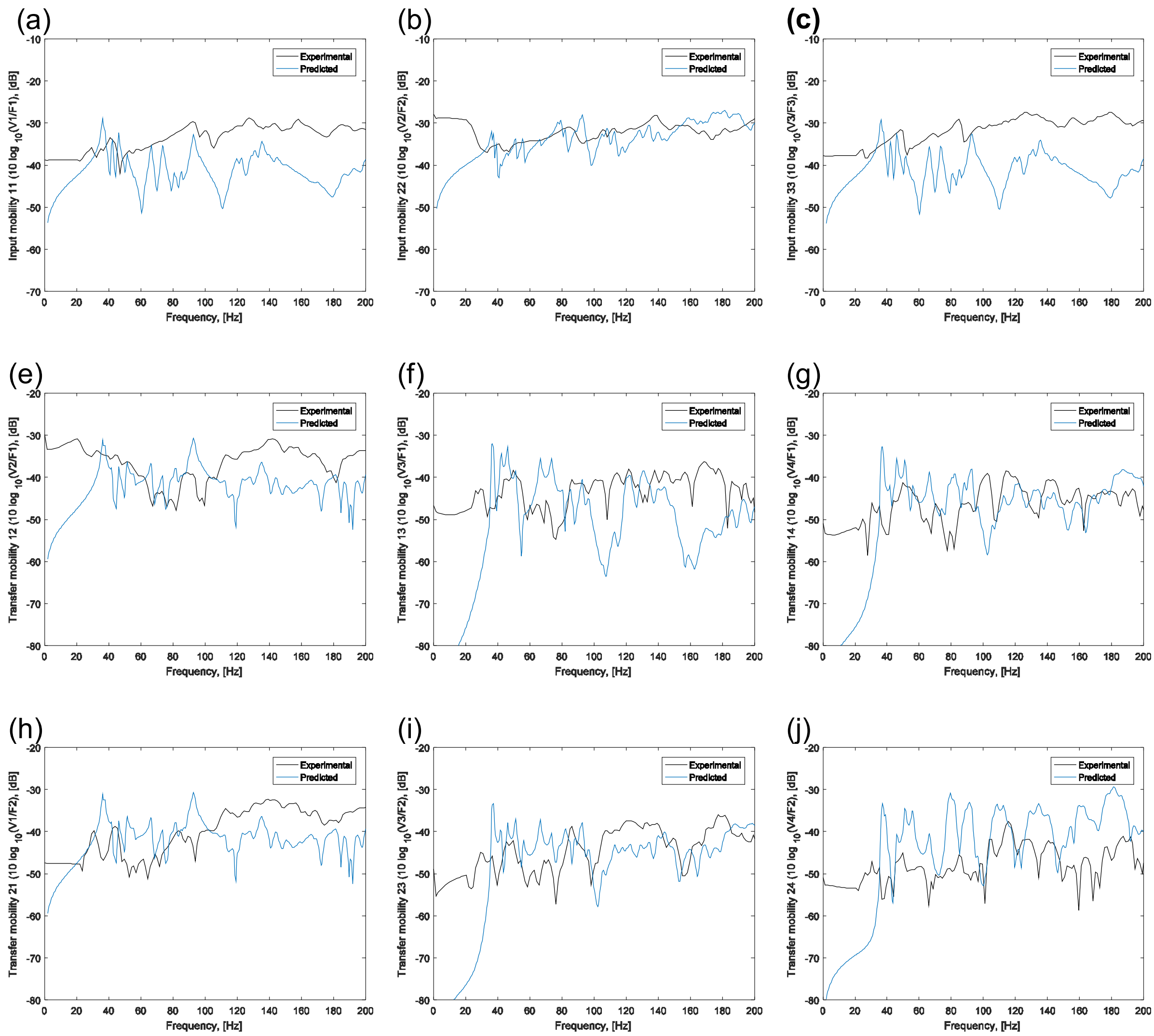

Figure 3.17: Comparison of measured and computed mobilities for various points over the floor

For a given tapping machine position, velocities were measured on 4 receiver positions on the top of the floor (in the sending room). Two points are located on joists and two points in between. Figure 3.16 displays the respective positions of the tapping machine and accelerometers with respect to primary wood frame elements.

It can be observed from figure 3.18 that above 25 Hz, predicted velocities are consistent with experimental data for the points 1 and 3 located over the beams. For the two others, velocity levels are overestimated. This could be an issue as areas located between beams account for the majority of sound radiation.

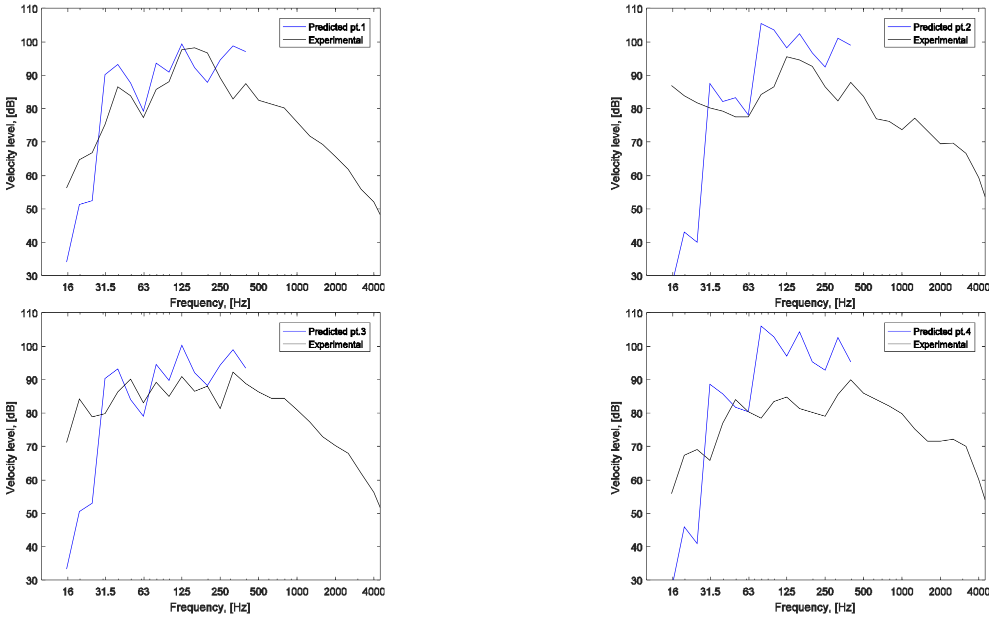

Figure 3.18: Velocity levels on top of the OSB (ref. 5e-8 m/s)

Raw floor and ceiling

A ceiling is added to the raw floor. It is made up of a single 12.5 mm plasterboard mounted on metal profiles. The latter are strongly connected to wooden beams but with resilient material in between. Moreover, mineral wool fills the created internal cavities. Details of the mounting are given in Figures 3.19 and 3.20.

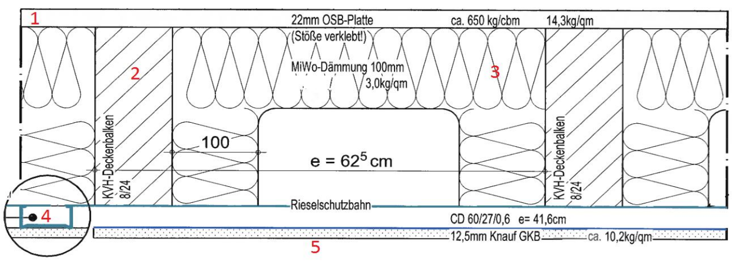

1: Floor plate OSB with 22 mm thickness, density 650 kg/m³
2: Wooden beams with 80 mm width and 240 mm height, distance between beams 625 mm
3: Mineral wool, density 30 kg/m³
4: CD metal profile, 60/27/0.6, 22 mm thickness, distance between profiles 416 mm
5: 12.5 mm plasterboard, density 816 kg/m³

Figure 3.19: Sectional view of the raw floor with ceiling

Figure 3.20 : CD Profile with clip connectors. The clip connector in the rear is covered with a resilient interlayer which will be ultimately perforated by the screws for the connection with wooden beams

Finite element model

A finite element model of the raw floor with ceiling is constructed using geometrical and physical data and constraints given in Fig. 3.19. Chosen physical properties for the different layers are given in tables 3.4, 3.5 and 3.6. Mineral wool properties are chosen such that por. 0.96, flow res. 7500 N.S/m^4, tort. 1.1, vcl 50 µm, tcl 150 µm and density 30 kg/m^3. Steel properties are chosen such that Young mod. 200 GPa, Poisson coef. 0.3 and density 7500 kg/m^3.

Oriented strand boards, plasterboards and metal profiles are modelled as slender solids in using first order shear deformation theory (rotational inertia and transvers shear are taken into account) and a normal drilling degree of freedom. Wooden beams are modelled as tridimensional elastic solids. In terms of boundary conditions, lateral displacements of the strand board and plasterboard layers are blocked. Moreover, wooden beams lay (simply supported conditions) on a rigid support. The OSB layer is punctually clamped (rigidly tied) to wooden frame elements every 300 mm and the plasterboard layer is punctually clamped (rigidly tied) to steel frame elements every 300 mm. The latter are modelled, in the low frequency range, as rigidly tied to wooden beams as the resilient material is perforated by the screws and squeezed between beams and profiles such that structural coupling remain strong. Figure 3.21 displays the finite element mesh of structural components, which is constructed in using the minimal criterion of 20 elements per meter.

ρ	E_x	E_y	nu_{xy}	G_{xy}	G_{yz}	G_{xz}
816 kg/m^3	3 GPa	3 GPa	0.14	1.31 GPa	1.31 GPa	1.31 GPa

Table 3.6 : Plasterboard mechanical properties

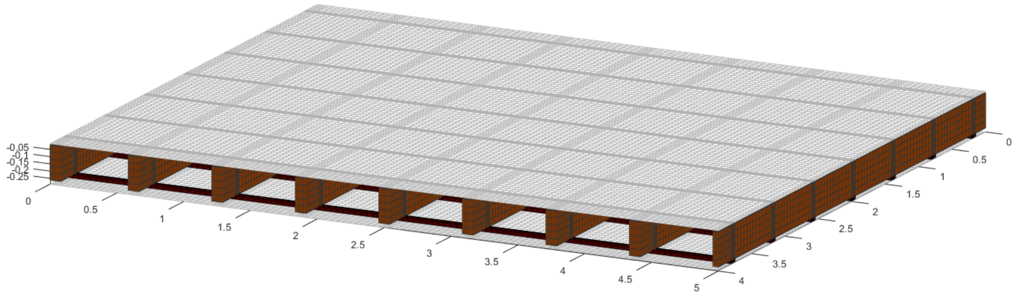

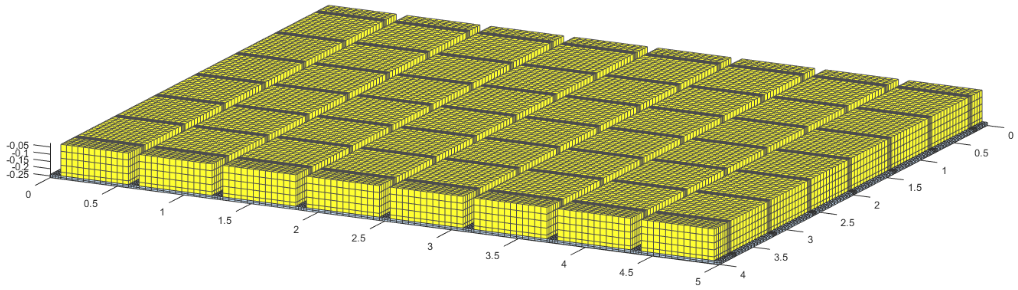

Figure 3.21 : Finite element mesh of the structural components (top) and of the poroelastic and acoustic domains (bottom)

Acoustic room model

The laboratory setup for Bauer Holzbau's measurement series is similar to the one deployed for the standard C1 floor However reverberation time was measured and provided by IBP for each tested configuration. In the present case it is and given in Figure 3.22.

(a)

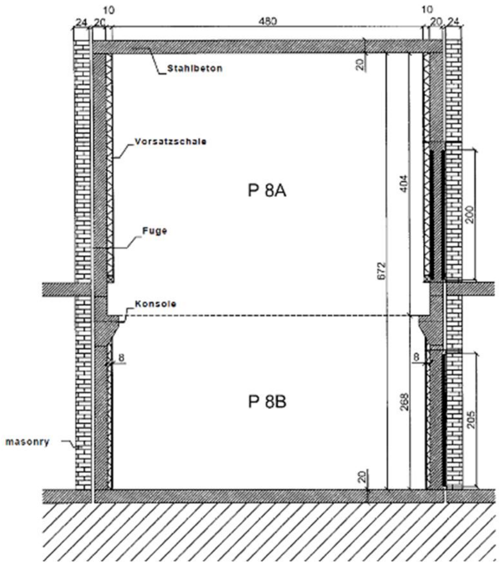

(b)

[Hz]	t [s]	f [Hz]	t [s]
20	1,60	**400**	1,63
25	1,10	**500**	1,52
31,5	0,93	**630**	1,41
40	0,67	**800**	1,40
50	0,48	**1000**	1,41
63	0,51	**1250**	1,42
80	0,50	**1600**	1,43
100	0,94	**2000**	1,40
125	1,28	**2500**	1,37
160	1,06	**3150**	1,19
200	1,40	**4000**	1,11
250	1,69	**5000**	1,11
315	1,60		

Figure 3.22: (a) Sectional view of the laboratory P8 provided by IBP. The wooden floor construction was installed on the console, separating the laboratory into two rooms. (b) Reverberation times for the receiving room

Airborne sound insulation

Figure 3.23 compares experimental data in third octave band with predicted confidence regions for sound pressure level differences in narrow band and third octave band. It can be observed that overall, above 31.5 Hz, the increased slope (see Fig. 3.14) resulting from the addition of the ceiling to the raw floor is well predicted by the model. As it was observed for previous airborne sound simulations (see Figs. 3.6 and 3.14), experimental data is close to the highest bound of the confidence region above 31.5 Hz meanwhile the model overestimates the airborne sound insulation below 31.5 Hz.

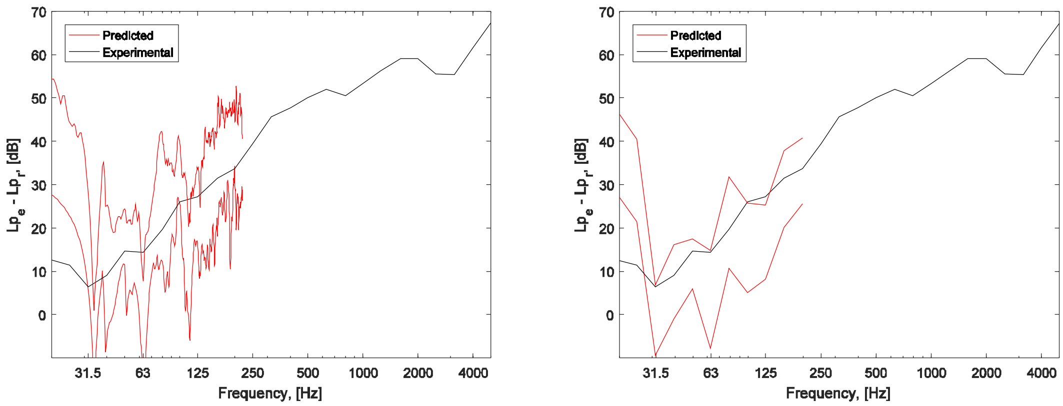

Figure 3.23: Comparison of measured sound pressure level difference and computed confidence region obtained for 1000 uniformly distributed random source positions

Impact sound insulation

Figure 3. 24 compares predicted confidence region in narrow band and third octave band with experimental impact sound level in third octave band. The substantial decrease in sound pressure level of around 15 dB in comparison with the raw floor (see Fig. 3.15) is well predicted by the model. Again, as it was observed for previous impact sound simulations (see Figs. 3.7 and 3.15), experimental data is close to the lower bound of the confidence region above 31.5 Hz meanwhile the model overestimates the impact sound insulation below 31.5 Hz.

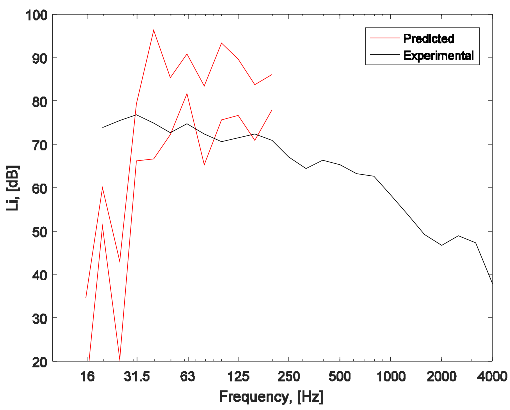

Figure 3.24 : Comparison of measured sound pressure level and computed confidence region obtained for 100 uniformly distributed random tapping machine positions

Thus, above 31.5 Hz, confidence regions for airborne and impact sound performance are conservative with respect to measured values: overall predicted performance is prone to be inferior to the effective one. However, as it was already observed for the raw floor, the predicted performance below 31.5 Hz is systematically superior to experimental values.

Floor 1, Bauer Holzbau

A floating system made up of a dry cement screed, and OSB layer, a plastic interlayer, a mineral wool layer and a wood wool/cement board is added on top of the raw floor.

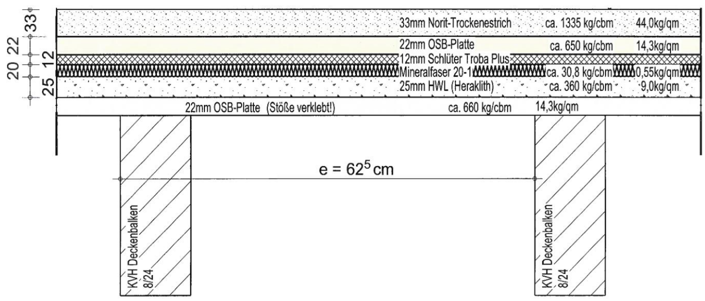

1: 33 mm dry cement screed, density 1335 kg/m³
2: 22 mm thick OSB, density 660 kg/m³
3: Plastic interlayer, mass per unit area 0.76 kg/m²
4: 20 mm thick Mineral wool, density 30.8 kg/m³, dynamic stiffness < 50 MN/m³
5: 25 mm thick wood wool/cement board, density 360 kg/m³
6: 22 mm thick OSB, density 660 kg/m³
7: Wooden beams with 80 mm width and 240 mm height, distance between beams 625 mm

Figure 3.25: Sectional view of floor 1

Such a system attempts to decouple the top layers from the raw structural elements past a so called mass-spring-mass frequency, which is fully determined by the mineral wool stiffness and the masses of adjacent components. A key point in the modelling is to have a good enough evaluation of the mineral wool stiffness (or “spring”) for the decoupling to occur in the correct frequency range. Moreover, this multi-layer system includes a plastic interlayer or drainage plate which is particularly stiff but has low mass per unit area.

Finite element model

A finite element model of the floor 1 is constructed using geometrical and physical data and constraints given in Figs. 3.25. Chosen physical properties for the different layers are given in tables 3.4, 3.5 and 3.7. The dry cement screed is very stiff and is modelled as a slender solid (it is assumed that no significant in plane deformation happens in the considered frequency range). The plastic interlayer is discarded from the model at it is quite stiff, provides very little mass to the system and no dynamic stiffness information is provided. The mineral wool is modelled as an equivalent isotropic solid, whose elastic modulus was constrained to be inferior to 1 MPa according to manufacturer information recalled in Fig. 3.25. A value of 0.1 MPa gave the best results, is consistent with available information and is consequently chosen. Finally, the wood wool/cement board is modelled as an equivalent elastic solid. Structural dissipation resulting from the increased complexity of the system is taken into account through modal damping, corresponding to a constant structural damping factor $\eta = 0.05$ over the whole frequency band of interest. No boundary conditions are imposed on the edges of the various added layers which simply lay on top of another with sliding contacts. The boundary conditions of the raw floor are kept the same as they were in previous models.

Figures 3.26 displays the finite element mesh of structural components, which is constructed in using the minimal criterion of 20 elements per meter. In particular, 6 elements are used in the thickness of the mineral wool layer modelled as an elastic solid.

	ρ	E	Nu
Dry cement screed	1335 kg/m^3	20 GPa	0.1
Mineral wool	30 kg/m^3	0.1 MPa	0.1
Wood wool/cement board	360 kg/m3	10 MPa	0.1

Table 3.7 : Mechanical properties for the multi-layer components

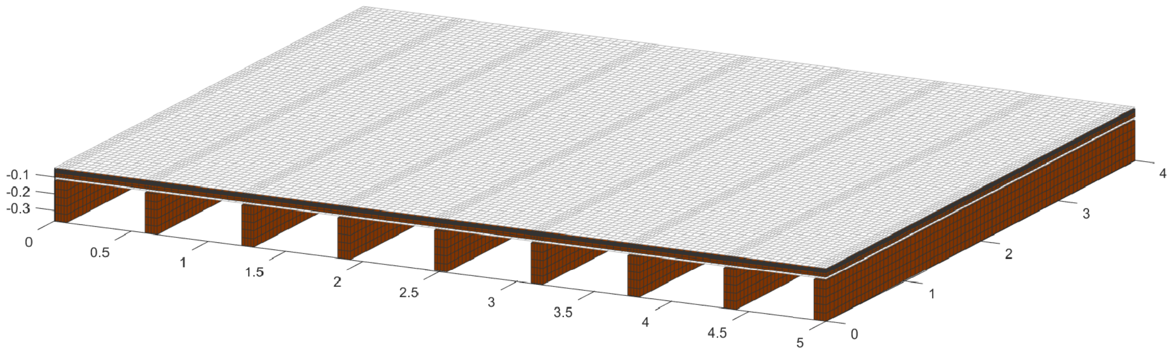

Figure 3.26 : Finite element mesh of the structural components

Acoustic room model

Reverberation time was measured and provided by IBP and is and given in Figure 3.27(b).

(a)

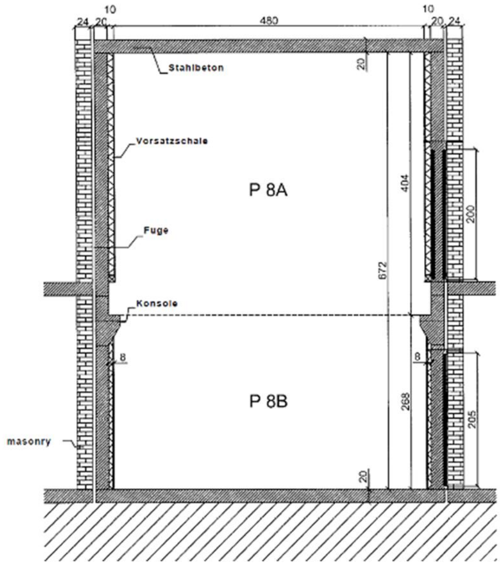

(b)

f [Hz]	t [s]	f [Hz]	t [s]
20	1,40	**400**	1,05
25	1,48	**500**	1,28
31,5	2,2	**630**	1,17
40	2,06	**800**	1,11
50	1,16	**1000**	1,05
63	1,27	**1250**	1,08
80	0,54	**1600**	1,07
100	0,57	**2000**	1,08
125	1,04	**2500**	1,08
160	0,72	**3150**	1,0
200	0,81	**4000**	0,92
250	1,17	**5000**	0,84
315	1,21		

Figure 3.27: (a) Sectional view of the laboratory P8 provided by IBP. The wooden floor construction was installed on the console, separating the laboratory into two rooms. (b) Reverberation times for the receiving room.

Airborne sound insulation

The comparison of Figs 3.14, 3.23 and 3.28 shows that below 1000 Hz, the addition of the multilayered system on top of the floor improves airborne sound insulation nearly as much as the addition of the ceiling and with the same slope. It can be noted that the substantial augmentation of mass in the model, resulting from the addition of the floating floor, is such that the first structural resonances appear earlier. It can be understood that the system leaves its stiffness controlled state, in which boundary conditions have a major influence, way quicker. Then, the model is not overestimating airborne insulation performance as much as before.

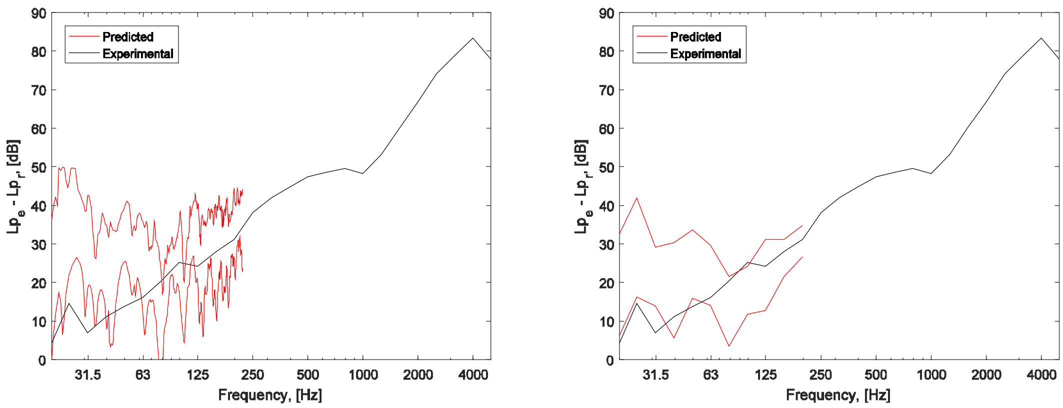

Figure 3.28 : Comparison of measured sound pressure level difference and computed confidence region obtained for 1000 uniformly distributed random source positions

Impact sound insulation

The comparison of Figs 3.15, 3.24 and 3.29 yields the same comments than within the previous paragraph. Measured impact sound pressure level in the 20 Hz third octave band is now closely approached by the predicted confidence region. Above 31.5 Hz, the prediction still is conservative as the effective values are close to the lowest bound of the confidence region.

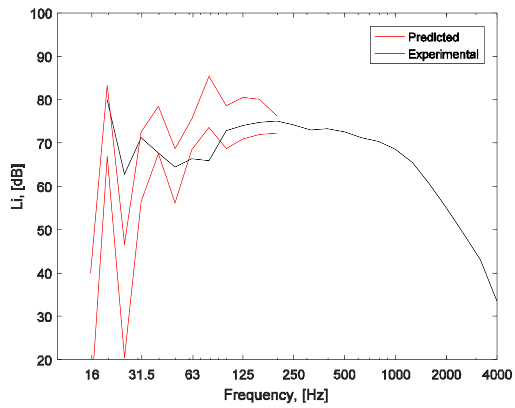

Figure 3.29: Comparison of measured sound pressure level and computed confidence region obtained for 100 uniformly distributed random tapping machine positions

Floor 2, Bauer Holzbau

The floating floor solution is now combined with the ceiling solution. The finite element models respectively constructed in previous sections are then simply combined such that hypothesis, material properties, boundary conditions etc. are kept identical.

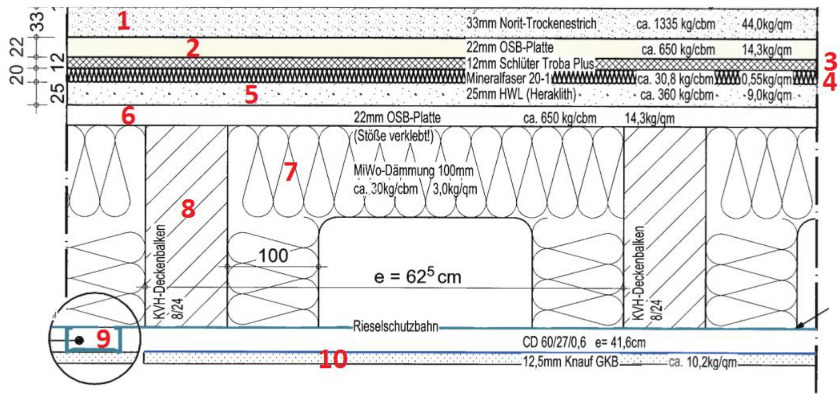

1: 33 mm dry cement screed, density 1335 kg/m³
2: 22 mm thick OSB, density 660 kg/m³
3: Plastic interlayer, mass per unit area 0.76 kg/m²
4: 20 mm thick Mineral wool, density 30.8 kg/m³, dynamic stiffness < 50 MN/m³
5: 25 mm thick wood wool/cement board, density 360 kg/m³
6: 22 mm thick OSB, density 660 kg/m³
7: Mineral wool, density 30 kg/m³
8: Wooden beams with 80 mm width and 240 mm height, distance between beams 625 mm
9: CD metal profile, 60/27/0.6, 22 mm thickness, distance between profiles 416 mm
10: 12.5 mm thick plasterboard, density 816 kg/m³

Figure 3.30 : Sectional view of floor 2

Airborne sound insulation

As it can be seen in Fig. 3.31, the overall slope associated with airborne sound insulation is consistent between predicted and measured quantities. Indeed, effective sound pressure difference belong to the predicted confidence region for the whole frequency range of interest (<200 Hz). Moreover, it can be noted that the confidence region got tighter as the system complexity and performance increased. That is to say that in the model, source position or laboratory conditions lost some importance or at least that fluctuations in source position of laboratory conditions did not propagate as much as before to airborne sound insulation performance indicators.

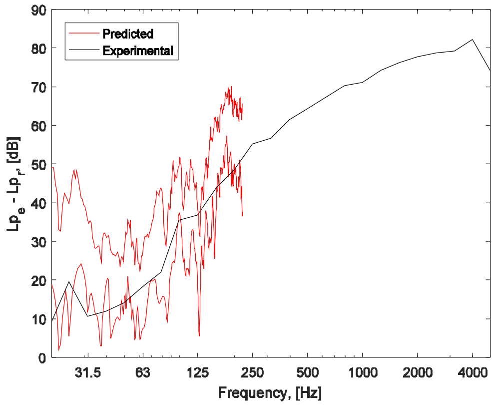

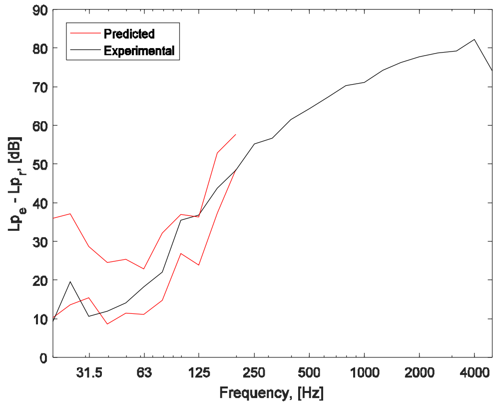

Figure 3.31: Comparison of measured sound pressure level difference and computed confidence region obtained for 1000 uniformly distributed random source positions

Impact sound insulation

The comparison of Figure 3.32 with Figures 3.24 and 3.29 shows that, above 31.5 Hz, the net decrease of impact sound level resulting from the combination of the floating floor and ceiling solutions is well predicted by the model. Measured performance is still close to the lowest bound of the confidence region, which is conservative. However, in the 20 Hz third octave band, the performance is still slightly overpredicted.

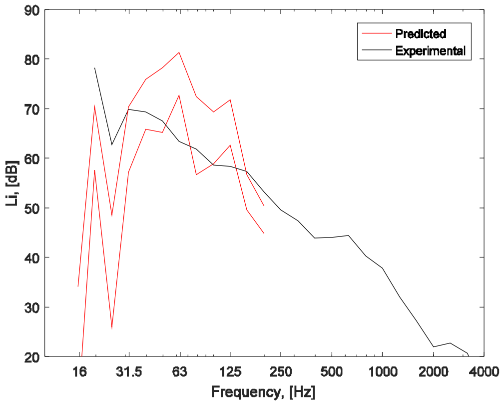

Figure 3.32: Comparison of measured sound pressure level and computed confidence region obtained for 100 uniformly distributed random tapping machine positions

3.1.3 Summary FEM

Airborne sound as well as impact sound measurement were undertaken at critical assembly stages of an *in fine* complex wood based floor. Such measurements allowed to test various modelling hypothesis at each stage in order to be able to draw the contour of a systematic modelling approach. Finite element modeling was performed for these floors at different assembly stages. Below 31.5 Hz it was shown that simple boundary conditions do not allow to accurately model the vibroacoustic behavior of such systems. Simply supported conditions of the structure seemed to maintain the system in a stiffness controlled behavior that did not correspond to experimentally observed phenomena. However, above 31.5 Hz the accuracy level of the prediction was quite satisfactory. The construction of confidence regions using varying test conditions allowed to get close to measured values. Moreover, obtained confidence regions were systematically conservative with respect to effective performance. Past 31.5 Hz, predicted performance was markedly prone to be inferior to measured performance. In order to tackle very low frequency problems below 31.5 Hz, thorough investigations of boundary and mounting conditions of the load bearing structure might be necessary.

3.2 SEA

3.2.1 Software implementation

SEA method can couple any resonating systems like acoustic cavities, elastic flat panels or curved panels under different kinds of loads:

- point or distributed forces,
- coherent or incoherent acoustic pressure fields

and through many types of cross-connections:

- line or points between structures or
- surface coupling between structure to acoustic or
- between acoustic -to-acoustic

It is required to code in a software all functionalities needed to build the SEA matrix and solve for energies and derive the physical quantities we are interested in:

- the acoustic pressure in fluid volume or
- the velocity in structures.

For covering the audio range typically from 100 Hz to 10 kHz, most of the calculation relies on solving analytical operators describing the subsystems. Analytical formulations of subsystems do not authorize describing small details that affect their dynamic.

For that, SEAWOOD software adds the capability of generating SEA parameters from deterministic meshed model based on FEM technique. Thank to FEM local modelling of heterogeneity, all small details of the geometry affecting the dynamical behavior are captured within the SEA parameters, which traduce the mean behavior of each subsystem. This technique of transforming FEM into SEA has been called Virtual SEA and is very convenient for scaling analytical simplified SEA models from more exhaustive FEM models which capture the 3D geometrical effects.

3.2.2 Adapting SEA method to timber-framed structures

Working on timber framed systems implies to adapt classical methods of calculating SEA coefficients to

- the complexity of wood materials: 3D orthotropic character of elastic parameters and dispersed values due to wood cut, age of wood, humidity, et.c.
- the complexity of junctions: ill-defined boundary conditions, variability of manufacturing.

Cross-Laminated-Timber (CLT) structures are a good example of this required adaptation. CLT boards are made of superimposed glued wood layers oriented at 90° relative to each other.

The wood fibers are oriented along the board plane. The full CLT board is then highly non-homogeneous depending on directions. The dynamic stiffness is very high along the in-plane direction (x and y-axis) as there are always half of the layers with their fibers parallel to it. Reversely dynamic stiffness along z-axis normal to the CLT board is quite low as, for all layers, fibers are perpendicular to it.

Due to this low z-stiffness, the layers during the bending motion are submitted to inter-layer shear forces, influencing the sound transmission in the high frequency range. For improving CLT description, SEAWOOD implements a specific extended orthotropic material, within (x, y) plane with different out-of-plane Young's and shear moduli. At the end the CLF board is modeled as an anisotropic panel with dynamic laminate cross-section specific to SEAWOOD and made of the several elementary layers of wood, each of them with a specific orientation.

3.2.3 Coupling SEA subsystems and transfer matrix approach

To improve acoustic insulation properties of timber-framed structures, acoustic materials such as porous or fibers are either fixed on to the walls or are separating constructive layers made of thick wood, concrete, plaster in floors, ceilings and walls.

SEA theory does not allow splitting of those individual layers into SEA subsystems without any physical consideration. First acoustic layers by themselves are most of the time highly dissipative and do not exhibit a marked modal behavior as required by SEA (a modal density is necessary for a subsystem).

Second the various layers (acoustic or structural) are most often strongly coupled to the supporting elastic based panel such as concrete or wood floor. Due to of its strong stiffness, the supporting panel may generally be simulated as an SEA subsystem as it shows some marked modal dynamics. The additional acoustic or structural layers mounted on the base panel are at low frequency generally producing additional resonances from their strong coupling with it.

To model such a system, the stiffest elastic layers showing modal resonances as standalone dynamical objects, are chosen as effective subsystems and are then modelled as elastic orthotropic plates in SEAWOOD. Then it is possible to introduce some mechanical coupling (if any) between the SEA subsystems. Let's now take the example of figure 3.37, the floor is made of two panels separated by a fiber acoustic layer and are maintained by studs. Thickness of layers are respectively 30 mm for OSB, 50 mm for fiber and 50 mm for concrete. Stud cross-section is 50mm height x 30mm width and are spaced by 600 mm.

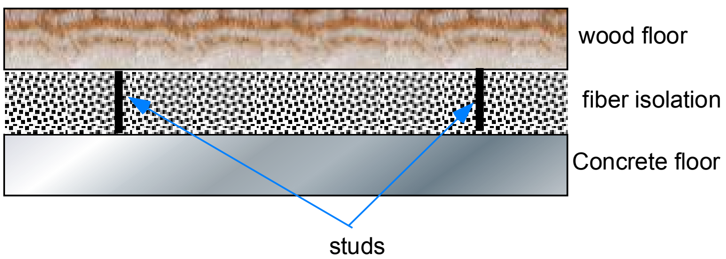

Figure 3.33: Concrete-wood floor example

Each of the two different panels in concrete and wood will be modelled as SEA subsystems. The choice of SEA systems is intimately related to targeted frequency range of the simulation as the dynamical behavior of each SEA subsystem requires at least five modes per frequency band to get stable average and mean value such as a rms spectrum. For complex systems as given in figure 3.33, some numerical tools like the VSEA solver of SEAWOOD may be required for deriving the subsystem partition from a side FEM model. However, analytical SEA may also be directly use for a priori selecting a usable subsystem partition as SEA calculation is fast and provide interactively the subsystems parameters when created. The criterion of five modes per frequency band is checked in real time when manually defining the subsystems.

The structure borne sound power flow that will cross this assembly will be modeled in SEAWOOD following the sketch shown in figure 3.34: an emission room containing the noise source (modeled as an SEA reverberant cavity) is coupled to the OSB floor plate. The latter is coupled to the concrete floor panel by a mechanical junction including the studs. The concrete floor is next allowed to radiate its vibrational energy in the receiving room (a second reverberant acoustic cavity).

The studs themselves are not considered as SEA subsystems here. Studs are very stiff structures (when isolated) and hence, only resonating in the high frequency range. In the low and mid frequency, they just act as an intermediate spring between the OSB and concrete panels. Therefore, in this frequency range they don't need to be explicitly modelled as SEA subsystems. The spring effect will be included as a boundary condition in the connection between the two upper and lower floors.

Adequate SEAWOOD junction model for this junction is a SEAWOOD line junction connecting OSB and concrete floor plates. This junction insures continuity of forces and displacement between the various wave types that are propagating in the plates. Flexural energy is coupled to in-plane energy (due to shear and extensional waves) due to the stud rotational motion. In the junction, the stud behavior is taken into account by the insertion of a joint defined as *Compact* or *Flexural* that simulates the stud cross-coupling effect of the different plate energies. *Compact* and *Flexural* refer to two SEAWOOD types of joints defined by their specific 4 x 4 static elastic spring matrix as the spring must connect shear, extensional, flexural stresses and displacements at plate interfaces. As there are three wave types in the wood floor coupled to three wave types in the concrete floor, the coupling matrix has 6 x 6 components. The diagonal are the 6 wave-DLF not accounted in the junction transmission. It remains 30 CLF spectra that describe the junction behavior. The resulting CLF's of the line junction are given in figure 3.35.

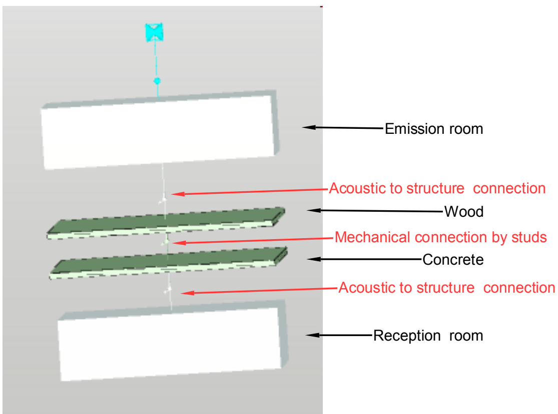

Figure 3.34: Modeling sketch of structure borne sound in SEAWOOD and related TL in dB

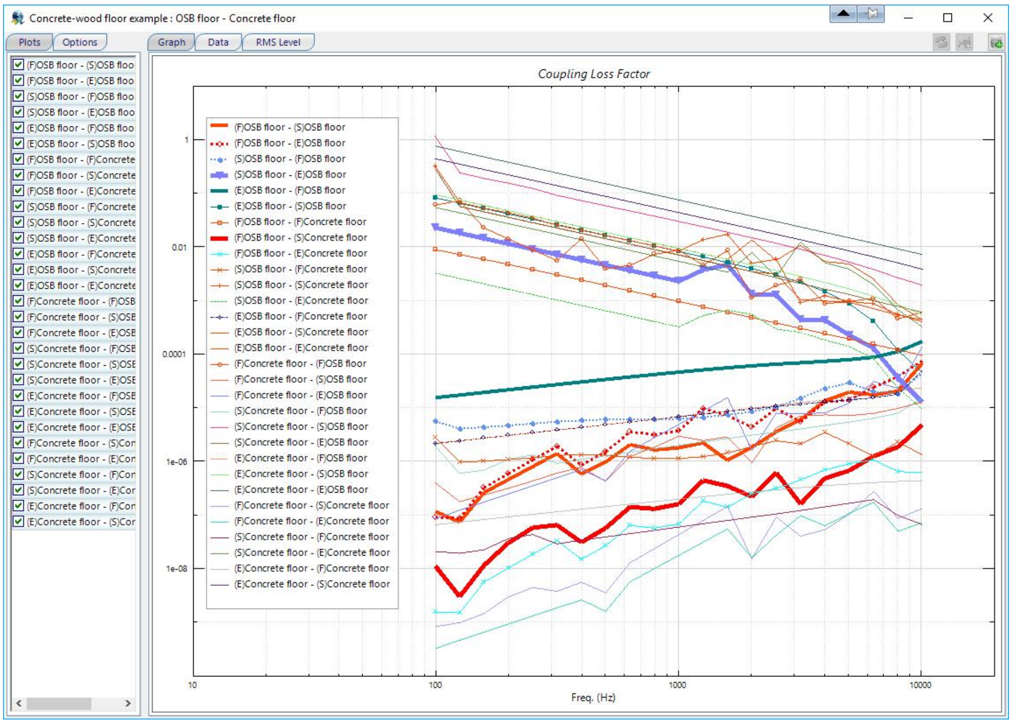

Figure 3.35: SEA Coupling Loss Factors at mechanical junction between wood floor and concrete floor

The panel sound transmission is characterized by the Sound Transmission Loss index (STL or TL) which is, by definition, equal to the logarithmic ratio of acoustically radiated power over incident power on the panel, due to incoming acoustic waves. It is expressed as follows (in dB):

$$TL(f) = -10Log\left(\frac{P_{rad}(f)}{P_{inc}(f)}\right)$$

High TL values corresponds to low radiated power and low TL values to high radiated power as incident power is most often a normalized constant term.

The TL index from previous structure borne sound transmission example is computed by SEAWOOD pre-assuming 0.01 constant internal loss factor for all panels. The result is displayed in figure 3.40 (in dB). The TL is calculated to approximately 25 dB at 100 Hz and increases up to 80 dB at 10 kHz.

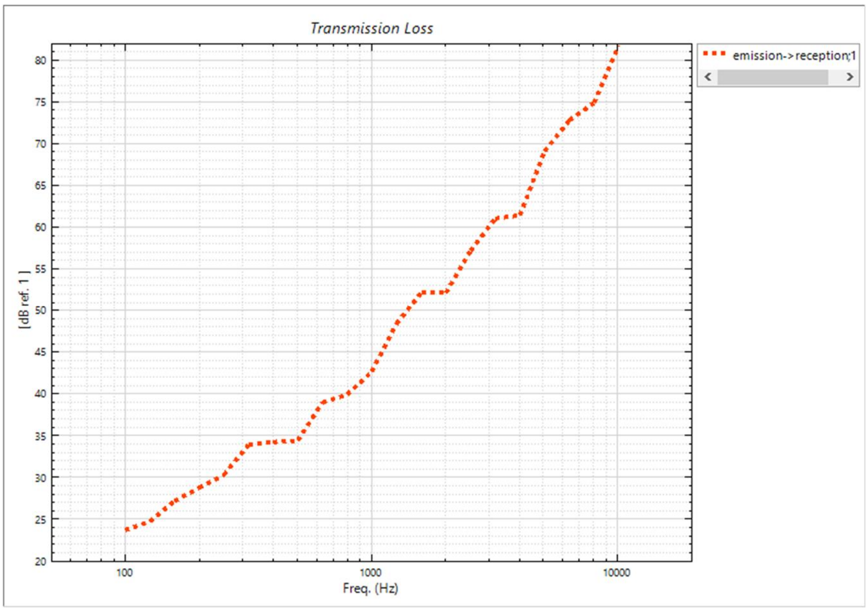

Figure 3.36: Structure borne sound TL from example Figure 3.38

Now after the structure borne sound TL is known, the airborne energy path has to be modelled in an appropriate manner.

In SEAWOOD models, acoustic layers are theoretically described by the "Transfer Matrix Method" (TMM). TMM method couples the various layers (including the supporting SEA panel considered as the first elastic layer) assuming continuity of stress and displacement at layer interfaces. Solving the TMM problems provides the Insertion Loss coefficient due to the acoustic treatment and the added damping of the treatment to the supporting panel.

Related SEA parameters of the supporting panel in the SEA network are modified by the acoustic treatment. Below in bullet points there are illustrations showing how this is effectively achieved in SEAWOOD. First, two TMM matrices need to be created:

- Fiber-wood matrix

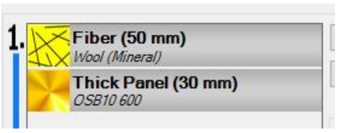

This matrix is computed by TMM from properties of fiber and OSB layers

- Fiber-concrete matrix

This matrix is computed by TMM from properties of fiber and concrete layers. These matrices are corresponding in SEAWOOD GUI to two objects of type *Trim,* which are attached to the concrete and the floor panel respectively.

When attached to a panel, their action is to filter the radiated power of the panel into the adjacent fluid by the Insertion Loss of the trim computed by TMM solver. Since two panels are present in the SEA network, two matrices are required.

The wool-concrete trim filters the radiation of the wood floor in the adjacent fluid and simulate the acoustic screening effect of fiber and concrete material presence. Similarly, the fiber-wood trim filters the concrete floor plate radiation.

TMM matrices also modify the state of their attached panel by adding to it some extra damping loss factor and mass. In particular, added mass by the trim modifies the modal density of the base panel as well as its wavenumber, influencing its radiation characteristics. As displayed in figure 3.40, the SEA model of the airborne sound contribution corresponds to two propagation paths from the source to the receiver fluid:

- Emission room to wood floor followed by radiation of wood floor in receiving room through the "fiber-concrete" trim filter (blue arrows in figure 3.37)
- Emission room to concrete floor through the "wood-fiber" trim filter followed by radiation of concrete floor in receiving room (red arrows in figure 3.371)

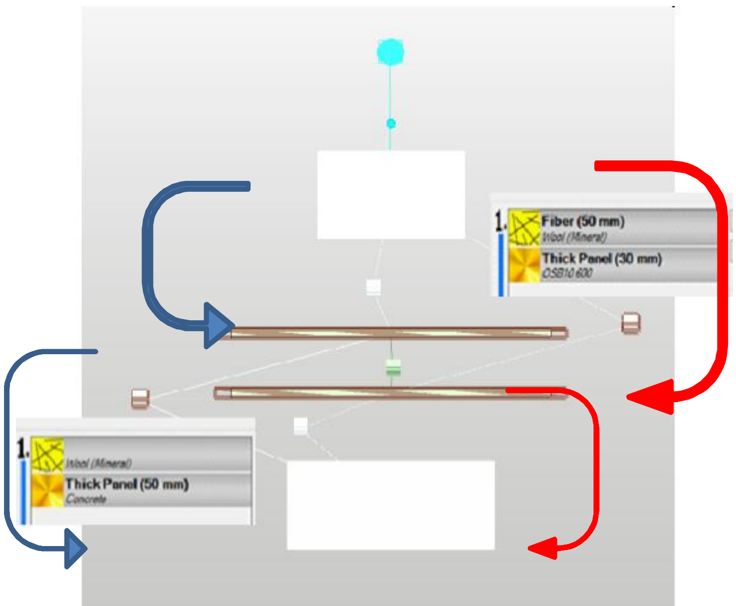

Figure 3.37: Adding airborne sound contribution to structure borne sound in example Figure 3.34

The SEA model now includes all propagation paths from the emission room to the receiving room. Total TL index can now be computed from the SEA model. The rank of transmission paths is conveniently performed by disabling or enabling the mechanical coupling between the concrete and OSB panels.

Two TL's are then predicted,

- "AirborneTL" corresponds to the case where the mechanical junction is disabled (no energy transmitted through this junction)
- Airborne + Structure borne TL" corresponds to the case where the mechanical

junction is enabled (energy is transmitted through this junction)

The two TL results are given in figure 3.38. It is clear that the energy path mostly contributing to the acoustic energy of the receiving room is the structure-borne path except below 150 Hz and in the1/3 – octave band centered at 1000 Hz.

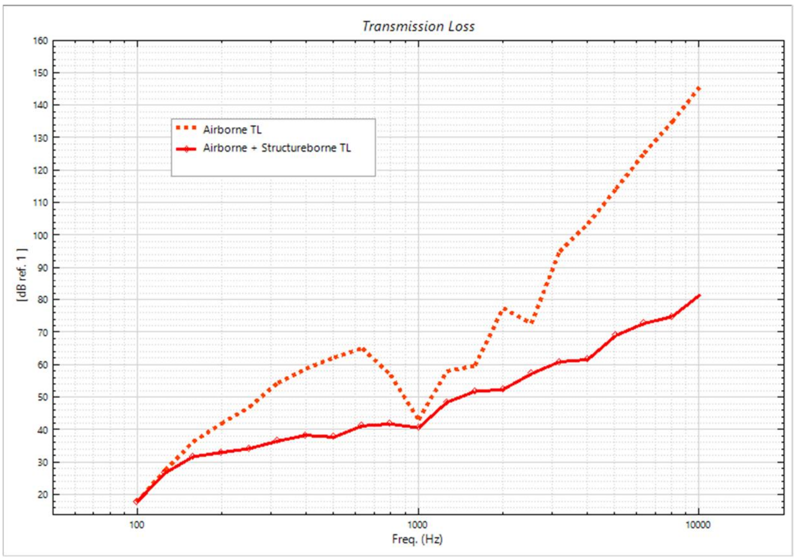

Figure 3.38: Comparison of TL due to airborne and to sum of airborne and structure borne paths

Vibrational energy inside a SEAWOOD model are not only sorted in function of propagation paths but also in function of the kind of energy stored in the subsystem.

Each subsystem mode is storing most of its energy around its resonance bandwidth. Under random load exciting this band, potential and kinetic energies in the band are equal. The sum of them is the total resonant energy stored by the modal oscillator. However, the random load has generally a wide broadband spectrum and excites the mode far from its resonance.

As shown in figure 3.39, the modal energy is split into 3 parts:

- the White energy is the energy stored within the resonance bandwidth.
- the Black energy is made of only kinetic energy and is stored in the frequency domain below the resonant bandwidth.
- the Red energy is made of only potential energy and is stored above the resonant bandwidth.

If the subsystem has distributed resonance frequencies over the whole frequency range, for a selected band of analysis (i.e. Octave or 1/3rd octave), the White, Black and Red energies may be summed up separately per analysis band.

Per analysis band, SEAWOOD calculates all three kinds of structural modal energy for each structural subsystems. As illustrated in figure 3.40, when a diffuse cavity excites a panel, the applied wall-acoustic pressure generates White, Black and Red energies in the panel at various degrees depending of the frequency of analysis.

These panel energies are then radiating in the receiver cavity with different radiation efficiencies, as the structural wavenumbers associated to the different energy types are different in the analysis frequency band.

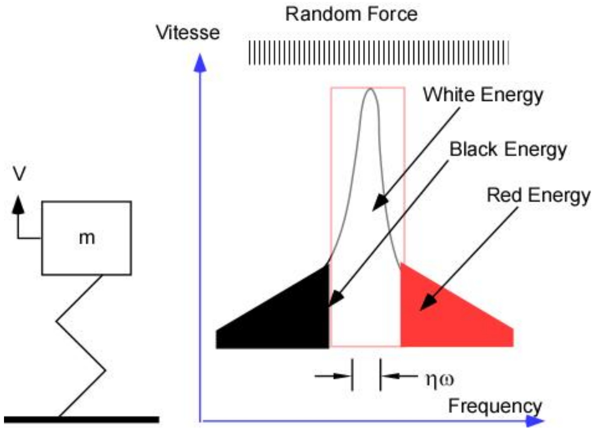

Figure 3.39: Modal oscillator response excited by broadband random force

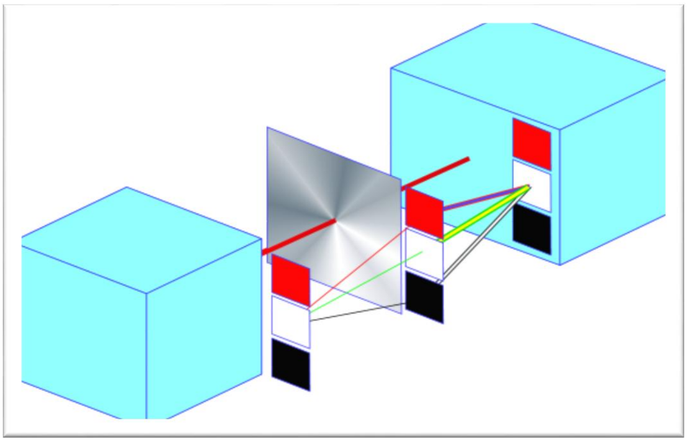

Figure 3.40: Transmission of White, Black and Red energies through a panel

Classical SEA deals with only White energy in structure. Other kinds are neglected. This is mainly because Black and Red energies are non-dissipative and cannot be included in the power balanced equations of SEA. Sound transmission between fluid and structure is most often driven by non-dissipative kinetic energy exchange in the low and mid-frequency.

It follows that Black energy is playing an important role in fluid-structure interactions and is definitively needed to get any accuracy in predicting sound transmission.

In SEAWOOD, calculating Black and Red energies along with the White SEA energy variables, is achieved by adding specific constraint equations to the SEA power balanced equations. These constraints are propagated along junctions by iterative solves of the extended SEA matrix (Loss matrix coefficients + constraint relationships).

The Black energy concept replaces in SEAWOOD the traditional Mass Law transfer of energy between two cavities separated by a panel modeled as an SEA coupling loss factor. Mass Law is usually used in acoustic SEA models to take into account non-resonant transfer of energy by by-passing panel resonant transmission. The related Mass Law connection traduces a direct power flow from emission room to receiving room between two resonant acoustic cavities (i.e. between resonant modes of cavities) resulting from the excitation and the radiation of non-resonant structural modes.

Mass Law energy exchange is then simulated by a junction connecting the two cavities and traduced by a CLF term relating the two cavity energies in the Loss matrix of the power-balanced equations.

The inconvenience of theoretical Mass Law – and related CLF expression - is in its limited validity. It is only valid for homogeneous infinite flat panels inserted between two reverberant cavities. Mass Law transmission has to be corrected for taking into account the finite-sized aspect of the transmission between the two cavities.

In our example, both Mass Law and Black energy transmissions are valid concepts and can be compared, since SEAWOOD also implements the Mass Law connection. As shown in figure 3.41, both Black energy and Mass Law theories give nearly same resulting TL index. In this calculation, the mechanical connection has been disabled as it drives the TL level.

Non-resonant energies provide more information on energy exchange in the system for better engineering practice: total vibrational energy of panels is split into White, Black and Red sub-energies allowing more insight in controlling panel vibration by either mass, stiffness or damping.

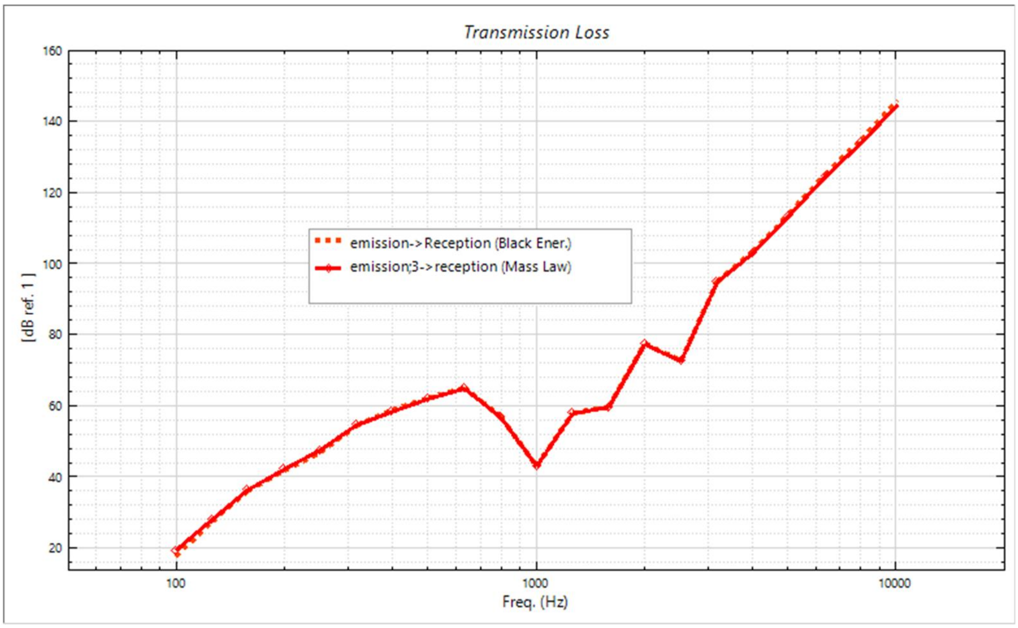

Figure 3.41: Comparison of TL due to airborne transmission using Mass Law or Black Energy theories for evaluating non resonant transfer of energy between emission room and receiving room

Now, thanks to model, the origin of power radiated into the receiving room can be split into its various components for full understanding of key-control parameters. In figure 3.42, the total power radiated into the receiving room is mainly due to the radiation of the concrete floor. OSB floor radiation is efficiently screened out except in the 1000 Hz frequency band.

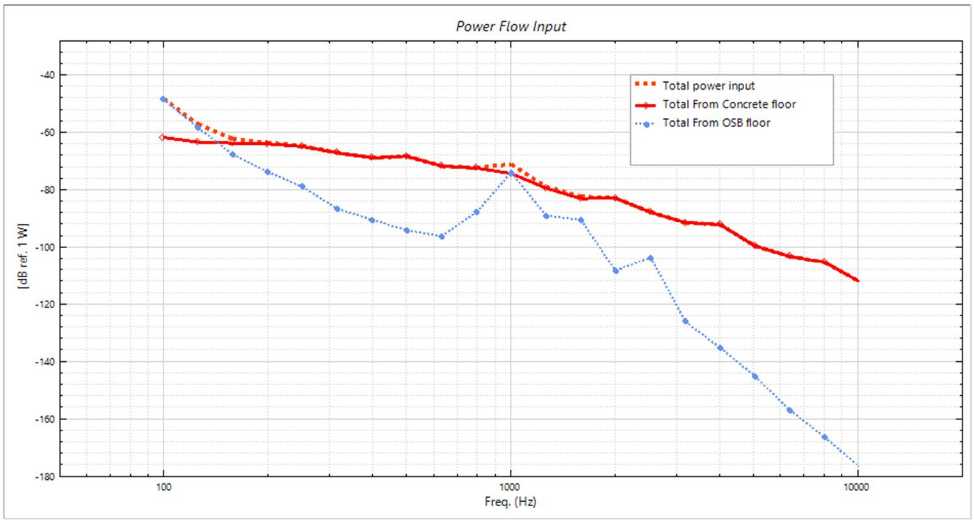

Figure 3.42: Power Level decomposition injected in receiver room (airborne + structure-borne paths)

The power injected into the concrete floor is provided by the OSB floor.

OSB floor energy itself can be decomposed into different components as shown in figure 3.43. Here the various “tags” are related to energy types as follows;

- tag “(F)” for flexural waves power;
- tag “(E-S)” for in-plane power driven by shear and extensional waves;
- tag “(B)” for flexural Black power;
- finally tag "(R)" for Red power of flexural waves. The predominant injected powers originate from the “(F)” energy above 400 Hz and by “(B)” energy below.

Mechanical conversion of energy through studs appears to be the most important mechanism in sound transmission. When changing the junction type in the concrete-to-OSB connection from *Line* type to *Multipoint* the related TL increases as shown in figure 3.44.

The *Multipoint* connection is weaker than the *Line* one. Line junction insures continuity of translation AND rotation at both concrete-stud and OSB-stud interface, leading to bending moment transmission emphasizing the flexural wave transmission. Multipoint junction transmits mainly translation and not rotation, reducing flexural energy transmission.

To conclude, this example of sound transmission simulation shows the importance of mechanical coupling between upper and lower elastic panels of a floor. The related coupling loss factors are highly dependent on the assembly technique of studs to panels. Due to potential on-site variability of the assembly, actual values of the connection might need to be measured and the results would have to be imported into the SEA model for accurate SEA TL simulation. Controlling inputs parameters leads to reliable estimates of TL thank to SEA models by fixing upper and lower limits of the simulation and, hence provides valuable engineering basis for improvements of the assembly.

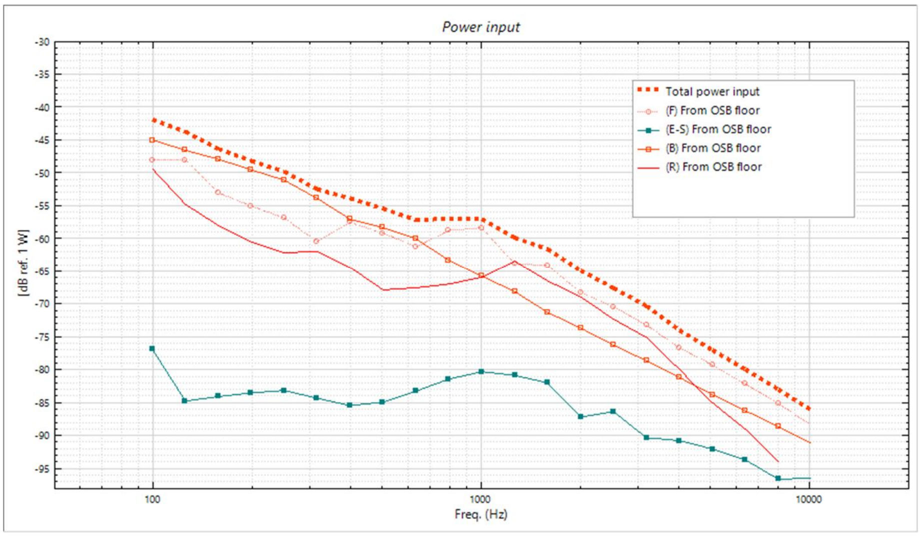

Figure 3.43: Origin of injected power in concrete panel

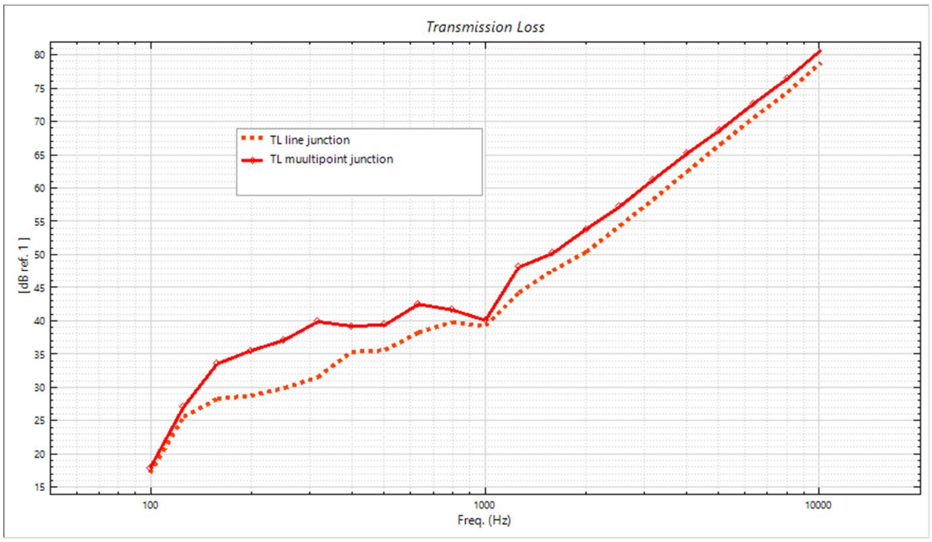

Figure 3.44: TL evolution when changing mechanical boundary conditions from line to multipoint

3.2.4 Application of SEAWOOD on a typical CLT floor assembly

Figure 3.49 shows typical CLT floor assembly used in many European countries. In figure 3.50 the related SEAWOOD model is shown (in right picture). The model comprises four effective SEA subsystems: two air cavities for simulating emission room and receiving room separated by the floor and two elastic plates for simulating the floor modes. The gravel and the fiber layers are not modelled as SEA subsystems but instead incorporated in the acoustic "trims", applied to SEA panels as described hereafter.

- The strong coupling induced by the concrete plate and the intermediate acoustic layers (gravels and fiber) on the CLT plate is simulated by a "trim" (i.e. by the associated TMM problem coupling all floors layers) applied to the CLT plate.

- Inversely, the strong coupling effect induced on the concrete plate by the CLT plate and the related acoustic damping layers, is simulated by the reverse "trim" applied to the concrete floor.

  The content of the two trims is also shown in figure 3.46 in the two left pictures.

When applying a trim to an SEA plate, the coupling loss factors of the connection with the SEA cavity are automatically attenuated by the insertion loss predicted from TMM trim modeling. The acoustic radiation of the CLT panel in the receiving room is then "screened" by the presence of the concrete plate, the gravel layer and the fiber layer. The concrete floor is radiating freely in the receiver room.

The SEA model provides a fast and efficient calculation process of the sound transmission of the entire floor, divided into airborne and structure borne sound transmission paths, the latter through direct mechanical connection between the CLT and Cement elastic SEA panels (Red arrow in figure 3.46). Airborne and structure borne sound transmission paths, are implicitly assumed being uncorrelated.

Figure 3.47 shows calculated results of the TL for two different assumed behaviors of gravel; TL (Gravel as Mass) assumes gravel layer behaving as a distributed mass; TL (Gravel as limped foam). assumes gravel layer behaving as a limped foam. As in the previous floor example the main transmission path is through the mechanical link as shown in figure 3.48.

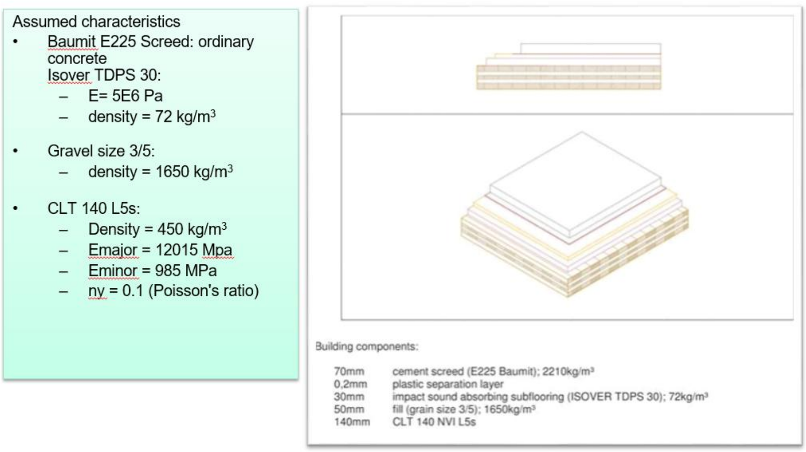

Figure 3.45: Composite floor (Concrete 70 mm on top separated by gravel and fiber layers for CLT 140 mm)

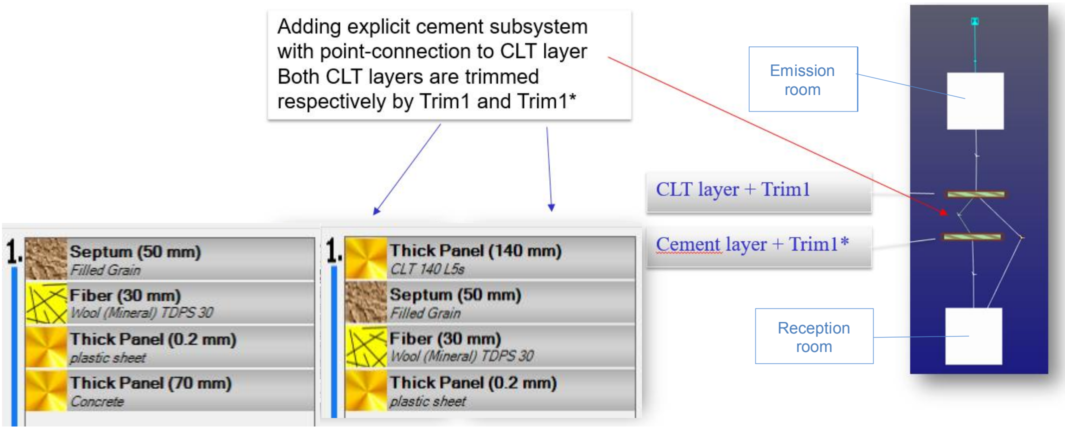

Figure 3.46: SEAWOOD model of Figure 3.42 floor configuration

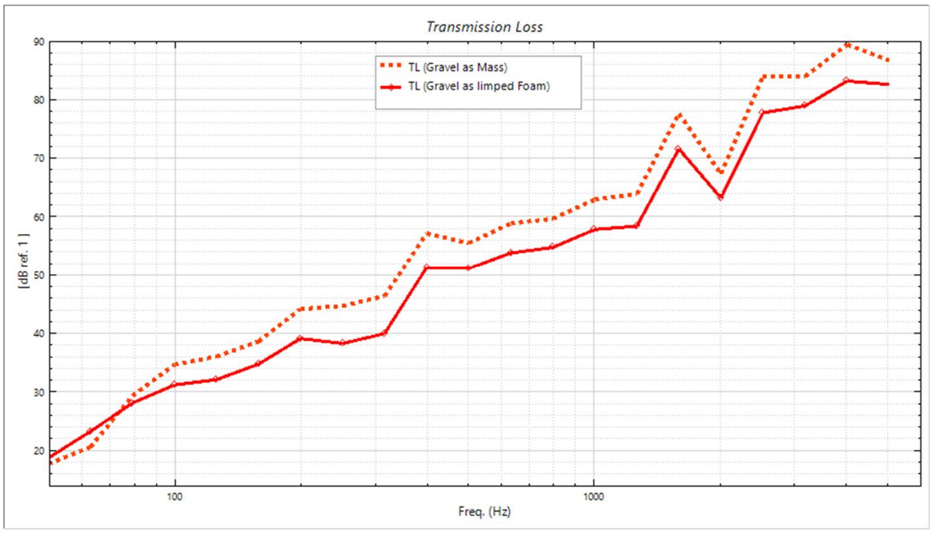

Figure 3.47: Comparison of TL simulation of composite CLT floor with two assumed behavior for the gravel layer

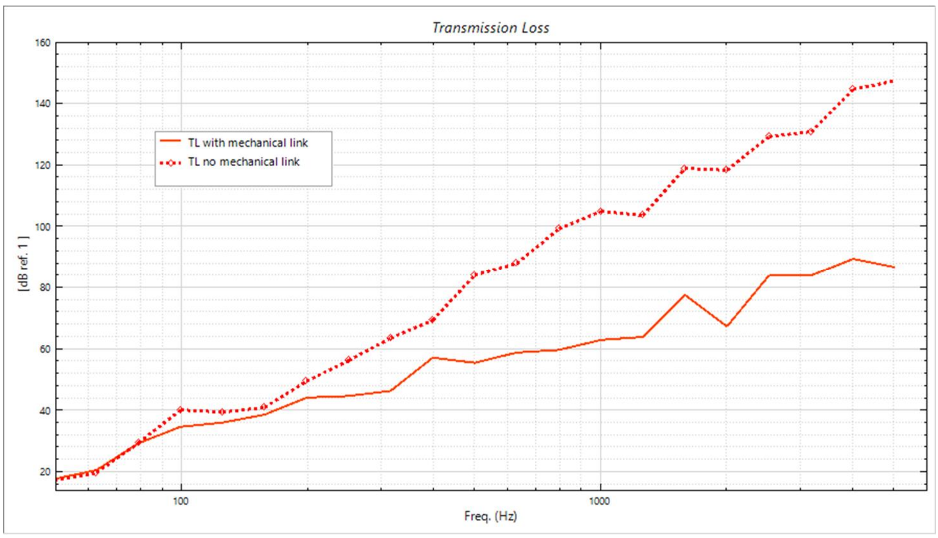

Figure 3.48 Simulation of TL of composite CLT with and without mechanical link

3.2.5 An example of direct sound transmission through a CLT 140 element

CLT panels as described in previous section, are made of orthotropic glued wood layers oriented at 90° from each other. The related CLT panel is made of 5 layers of 28-mm thickness oriented at 90 ° from each other. The local x-axis of each layer is oriented along the wood fiber, direction of maximal stiffness. When assembled, the wood stiffness of the various layers is then spread rather uniformly in all directions of the x-y plane in the global axis of the CLT assembly. Panel size is set to 3.5 m x 3 m.

To model the dynamical behavior of the assembly in SEAWOOD, several options are available and best modeling practice, if not obvious, has to be scaled on laboratory test results (i.e. with TL measurements in that case).

From this observation, four possible SEA models of a CLT panels are modelled and solved, corresponding to four different configurations A, B, C, D.

A. CLT cross-section is Uniform. An equivalent material is used
B. CLT cross-section is orthotropic with ratio 12 between x and orthogonal y axis
C. CLT cross-section is built using Static Laminate (LSTAT) available in SEAWOOD which should give similar result as if using the Uniform one
D. CLT cross-section is built using Dynamic Laminate (LDYN) available in SEAWOOD.

   LDYN model takes into account the degrees of freedom of each individual layers and cross-couples them into a single matrix from which are extracted eigenvalues and eigenshapes of the assembly for retrieving evolution of modal density, mass and damping loss factor of the assembly vs. frequency, the assembly being considered as a whole.

In practice, the elementary internal CLT layers are submitted to shear forces at their interfaces inducing distortion of the section rotation due to bending. The dynamical behavior of each individual CLT layer is calculating assuming the material is described by its orthotropic matrix of elasticity. Nevertheless, the vertical z-direction, normal to the plane of the plate behaves differently as z is always orthogonal to the fiber direction, meaning the elastic parameters are here 12 times smaller than in the fiber direction.

The elementary CLT material is finally described in the LDYN (“Dynamic Laminate”) model by an orthotropic elastic matrix extended by two other elastic parameters Ez and Gz, corresponding to Young's modulus in z-direction and shear modulus along the in-plane xy directions. Related CLT material description is given in figure 3.49. The default damping loss factor for panels in all configurations is shown in figure 3.50.

As structure borne path has been seen in previous example as the dominant paths, most of the energy transfer may be driven by the White energy of the panel, controlled by the equivalent modal DLF. As no measurement is available for this system, DLF is assessed to some decaying DLF spectrum, structural DLF being most often decaying as A / f^{β} with *f* the frequency, β the exponent laying between 0.5 and 0.7 and *A* as scaling factor.

All A, B, C and D configurations share the same DLF spectrum. TLs provided by the four models are compared in figure 3.51 with room acoustic measurement of the CLT panel. The most sophisticated model D, exhibit the best prediction in the HF range.

The measured TL curve shows a plateau above 2000 Hz. This plateau is only reproduced but rather imperfectly by the model D. The appearance of a TL plateau in HF is explained by the increase of driving point mobility of the panel above 3000 Hz as shown in figure 3.52. The panel is less stiff at high frequency due to internal shear motion at layer interfaces and apparent mass of the panel is lower, decreasing the sound transmission as the internal layers are mechanically decoupled in these frequency ranges.

As elastic parameters are all chosen from literature, significant differences with tested panel properties should be expected, especially for Gz and Ez, the new parameters that condition the CLT behavior in the LDYN model D, as they are not generally measured.

It gives an open door to extra measurements on CLT material. Measurement of driving point mobility on such structures would also help in calibrating elastic parameters of specific tested CLT materials.

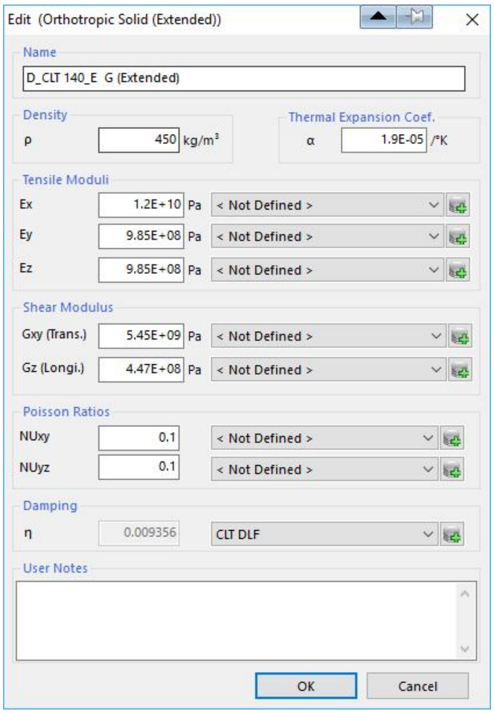

Figure 3.49: CLT layer material with extended elastic properties Ez and Gz for configuration D_LDYN

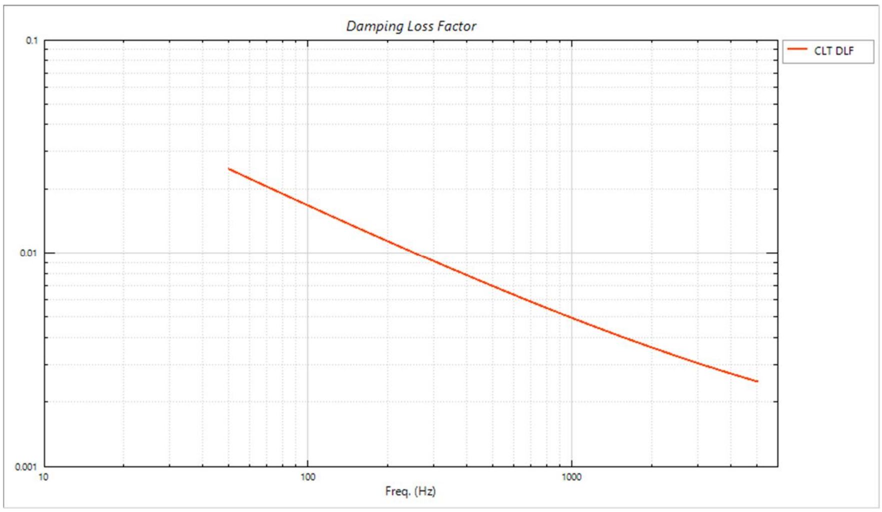

Figure 3.50: Default DLF spectrum for the four CLT140 SEA panel configurations

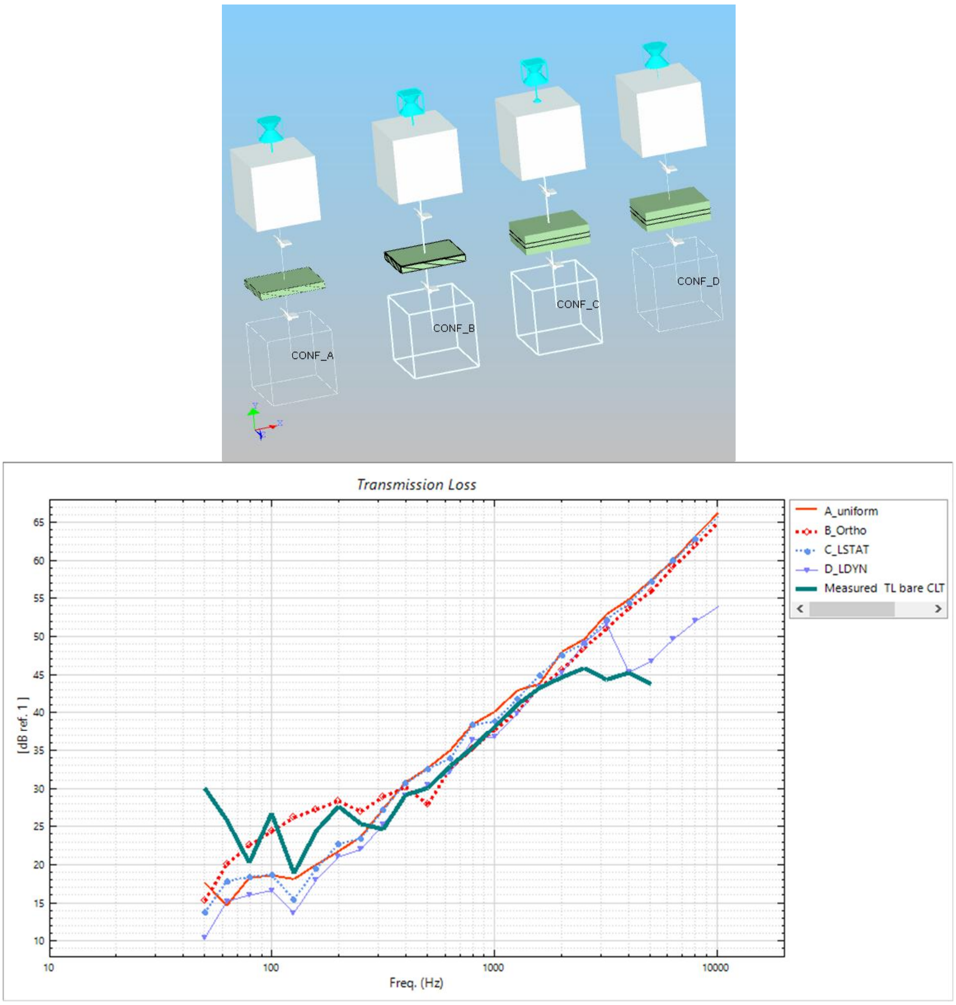

Figure 3.51: Simulation of the four TL configurations compared with measurement for CLT 140 standalone panel

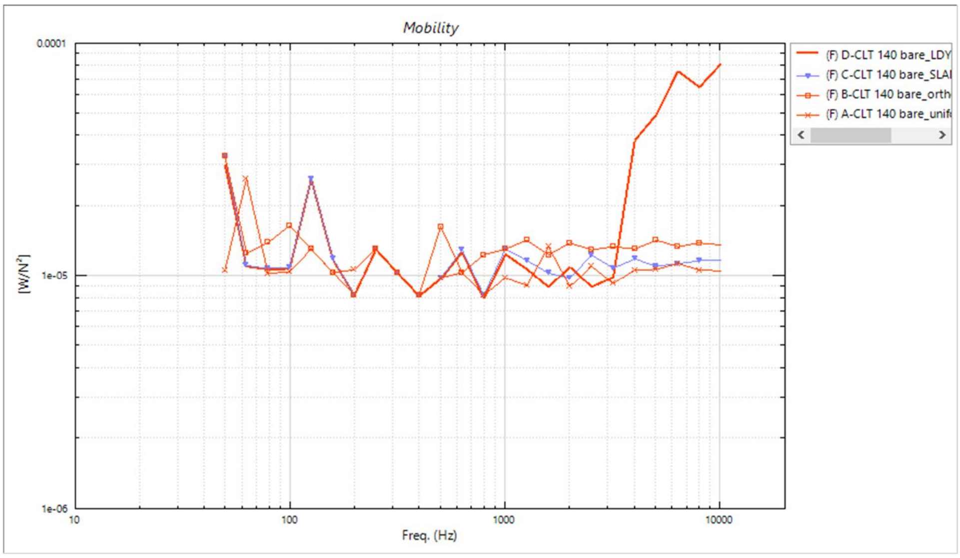

Figure 3.52: Real part of driving point mobility of simulated CLT140 panels in the four configurations

3.2.6 Application to composite wall partition

Below is discussed an example of SEAWOOD modeling of a doubled-wall partition with separated studs made of OSB plates and plaster board layers as described in figure 3.53.

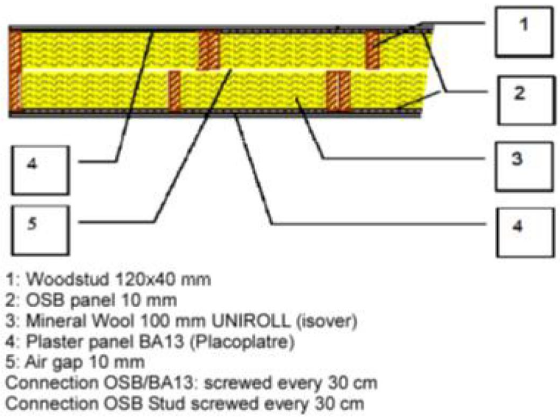

Figure 3.53: Double-wall partition with separated studs

This partition is used as an example since it has been measured between two reverberant chambers in FCBA laboratory for determining its TL performance. A laboratory set up example is shown in figure 3.54.

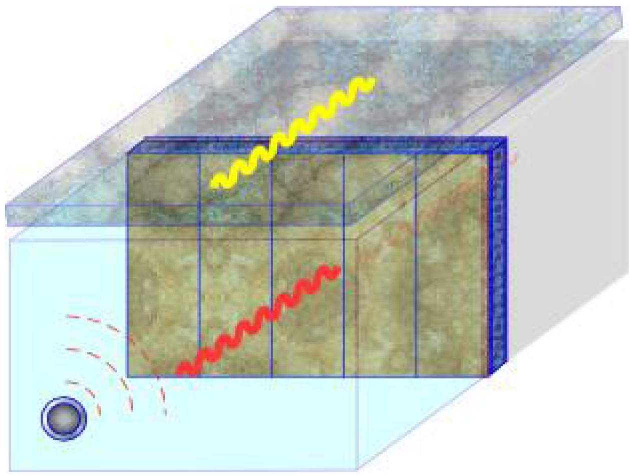

Figure 3.54: Double-walled partition tested in reverberant test chamber

The sound transmission of the whole wall as defined in figure 3.53, is performed by considering the two outer plaster plate are two elastic subsystems on which act the trims made of all other layers.

Figure 3.55 illustrates the SEA decomposition into the two elastic plaster panels to which is allocated a corresponding trim made of all remaining layers. Note that a thin air gap is separating plaster and OSB layers. Because as they are nailed together and not everywhere in contact, there is in-between some residual air that dissipates energy through air pumping. These features are modeling the airborne path from emitter cavity to receiver one.

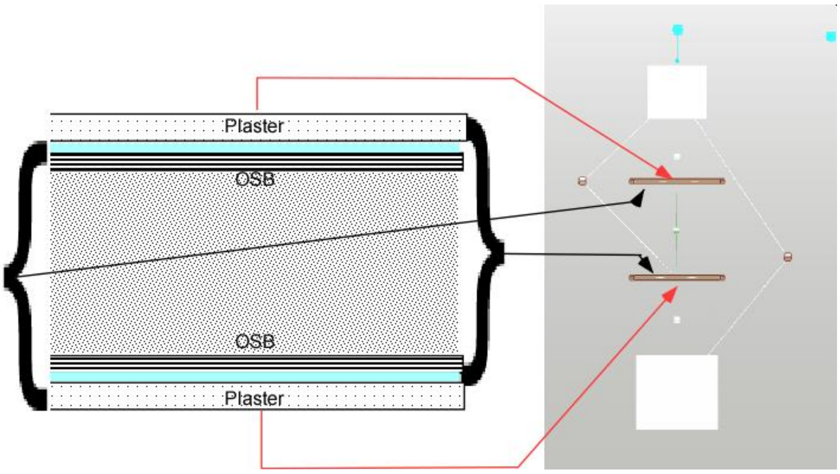

Figure 3.55: Double-walled partition decomposition into SEA subsystems

Both plaster panels are initially assumed to be mechanically uncoupled, since the layers have no direct mutual connection.

A comparison of the predicted TL using model sketched in figure 3.55 is performed with the measured TL in figure 3.56. A large TL difference is observed with different TL slopes vs. frequency. Only mechanical coupling may explain such a difference and some way of modeling this path has to be introduced in the SEA model.

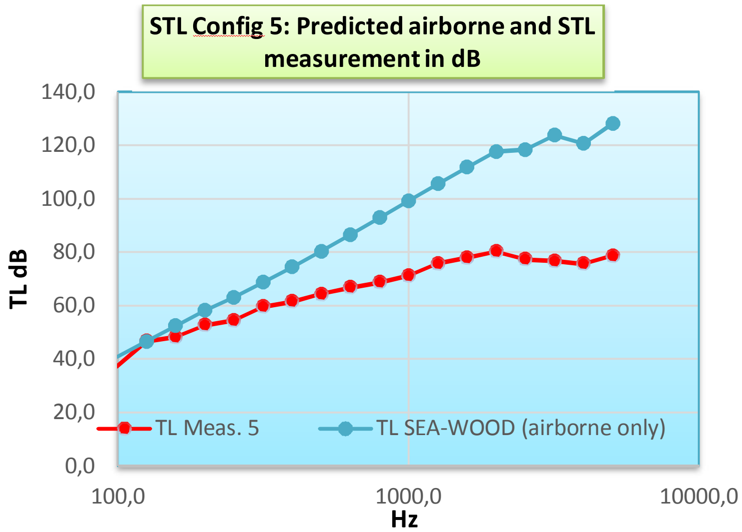

Figure 3.56: Comparison of simulated TL with only airborne and measurement

The wall is mounted in the same room and then plaster and OSB panels both sides of the wall are indirectly connected through joint to the concrete floors and walls of the test room. The wall thickness of the test room is 1-m thick concrete. No significant bending motion is expected from such a thick wall and if any mechanical coupling exists with the measured partition, energy would need to travel within the concrete of the test room, most probably through surface waves (so-called Raleigh's waves).

SEAWOOD does not provide analytical model for predicting surface waves in thick 3D solid system as SEA is dedicated to the modeling of soft thin shell dynamical systems. However, a 3D solid elastic system is easily modeled by the finite element method and SEAWOOD incorporates a specific solver (SEAVirt), based on the Virtual SEA method [41, 46, 47], offering the capability to convert FEM dynamic information into a set of SEA parameters directly usable in SEAWOOD GUI.

The aim is now to simulate the mechanical coupling between the two wall partitions using FEM modeling (using NASTRAN-NX software) and converting the output of this model into usable SEA parameter through the VSEA solver.

The FEM model complexity is reduced to a minimum by only considering the two OSB10 layers glued on a 1-m thick wall modeled with FE-solid elements. OSB10 layers are modeled using FE-plate elements. The corresponding FEM model after meshing is seen in figure 3.57 (top picture). The dynamic of the FEM model is given by an FRF matrix, each complex FRF of velocity/force type being synthesized between pair of reference nodes in limited number and randomly selected between available FEM nodes. Real global eigenvalues of the FEM model are extracted using NASTRAN solver to cover the frequency range of interest as seen in the middle picture of figure 3.57. All modal amplitudes at all selected reference nodes are exported to SEAWOOD and required FRF matrix is synthesized thank to the VSEA solver. The VSEA solver automatically performs a partition into weakly subsystems by scanning the FRF matrix and sorting the reference nodes per effective found subsystems.

The SEA parameters such as modal density, mass and CLF between subsystems are identified by the inverse VSEA solver from the given subsystem partition and the FRF matrix input. Here our concern is only about getting the CLF between the inner panels of the SEA model (i.e. the OSB layers). The SEA CLF as provided by the VSEA model (see bottom figure 3.57) is imported in the SEAWOOD model and allocated to the mechanical junction that is added between the two trimmed plaster panels. With this mechanical connection the SEA model now predicts the measured TL correctly (see bottom graph in figure 3.58).

To conclude, double-wall panels with high acoustic insulation performance are very sensitive to mechanical coupling and therefore the coupling with the test room facilities cannot be neglected in the simulation. A seen in the double-wall example, SEA modeling simulates with high accuracy all primary paths as soon as they are correctly characterized by their CLF.

CLF may be directly simulated with analytical available SEAWOOD library or be predicted using side FEM model (with back conversion into SEA parameter) or if the physics of the coupling is difficult to assess by experimental characterization of CLF using Experimental SEA method (ESEA, also called inverse SEA method). Virtual SEA method as used in this example is a specific instance of inverse SEA method where input data are synthesized using FEM mode shapes and eigenfrequencies of the FEM dynamical system.

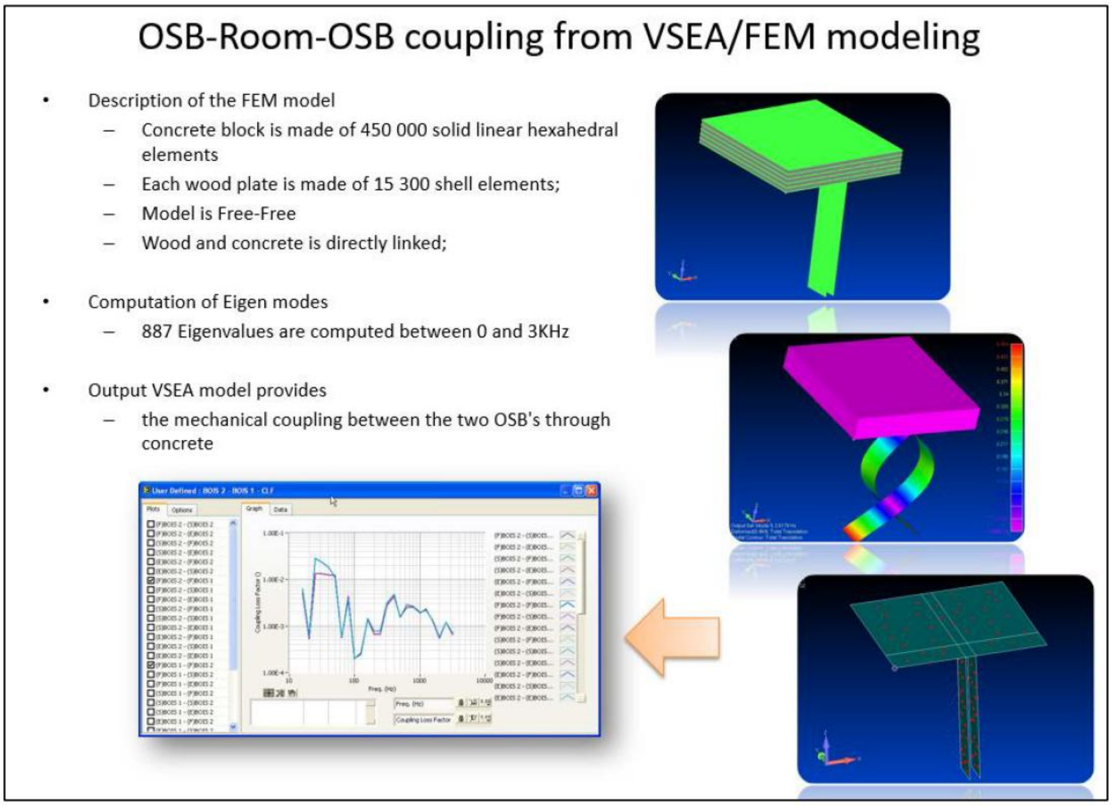

Figure 3.657: Simulating OSB panel to room concrete floor using SEAWOOD Virtual SEA method

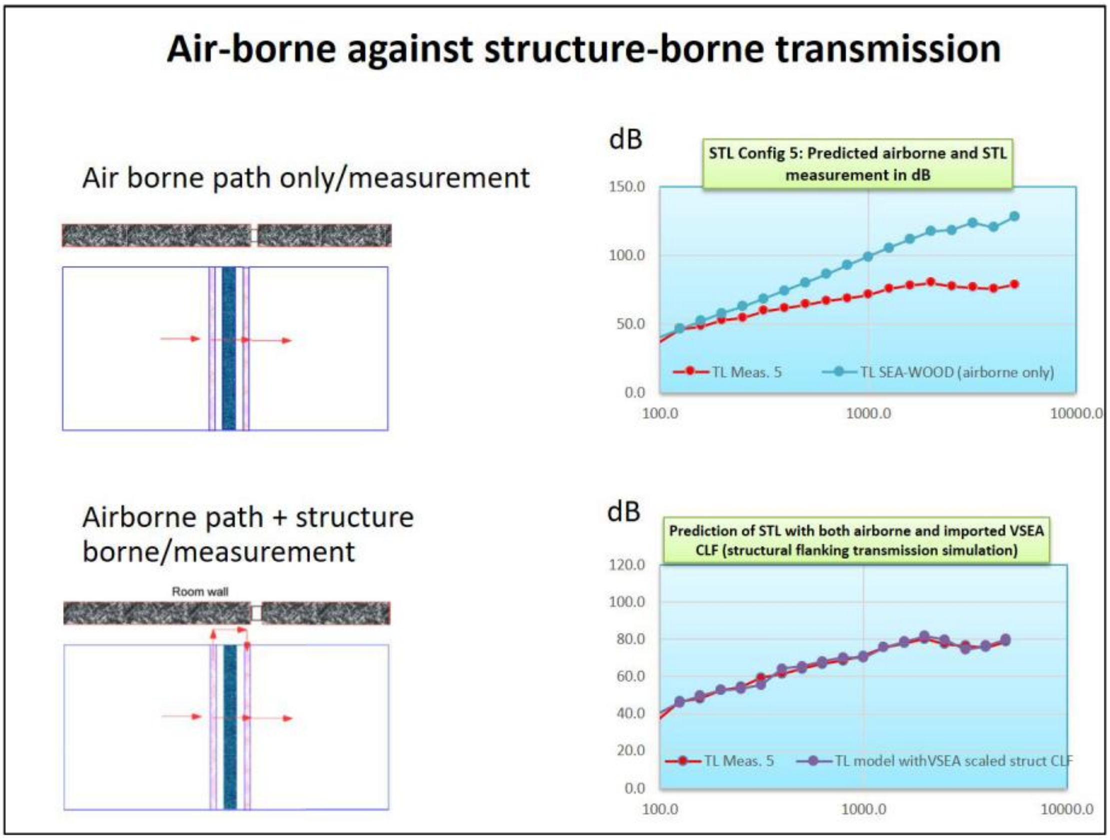

Figure 3.58: Comparing TL measurement of double-walled panel with simulated SEA TL with and without VSEA CLF between the two walls

3.2.7 Modelling impact noise

Experimental investigations followed by numerical SEA-based simulations have been undertaken on several types of floors using a shock machine. Each investigated floor is split into subsystems as shown in figure 3.59. Subsystems are limited by the underlying presence of studs that create wave reflections at their boundary confining the energy from source into the local modes of each region (the subsystems).

The shock machine is delivering power to the floor. The most critical task is to predict this injected power from measured vibrational descriptor. From the record of the floor velocity, *v,* in the nearfield of the cylindrical taps of the shock machine, the injected power is calculated as

$$P_{inj} = \frac{v^2}{Y}$$

where *Y* is the actual real part of complex driving point mobility of the floor at the tapping impact location.

In SEAWOOD this quantity is approximated by the theoretical real part of the spatial average of the driving point mobility of the floor. Injecting this power in the SEA model of the floor (here an OSB 18) allows predicting the mean floor velocity thanks to related SEA theoretical model shown below in figures 3.59 and 3.60. Predicted and measured velocities are in close agreement validating the interest in using SEA model for floor transmission prediction as seen in figure 3.61.

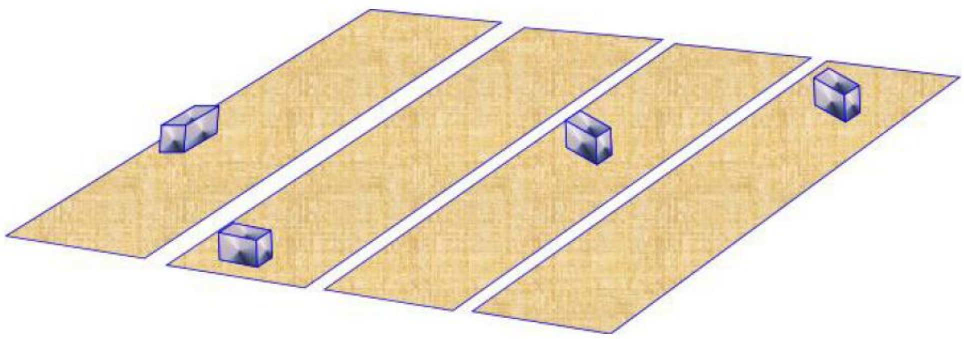

Figure 3.59: Dividing a floor into subsystems

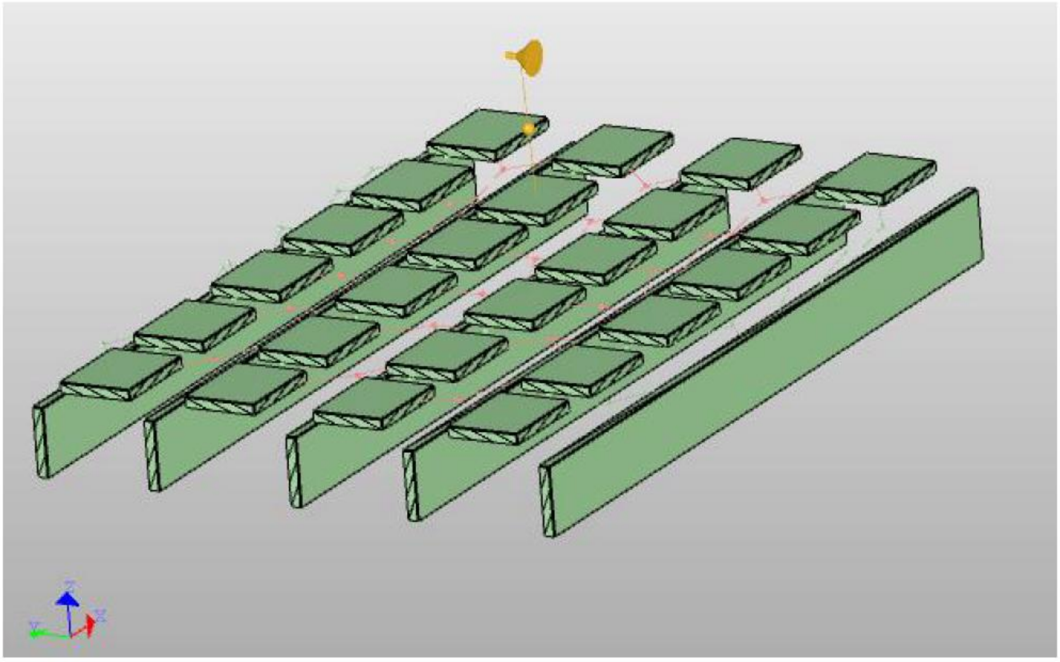

Figure 3.60: The SEA model of the floor for shock response calculation in SEAWOOD

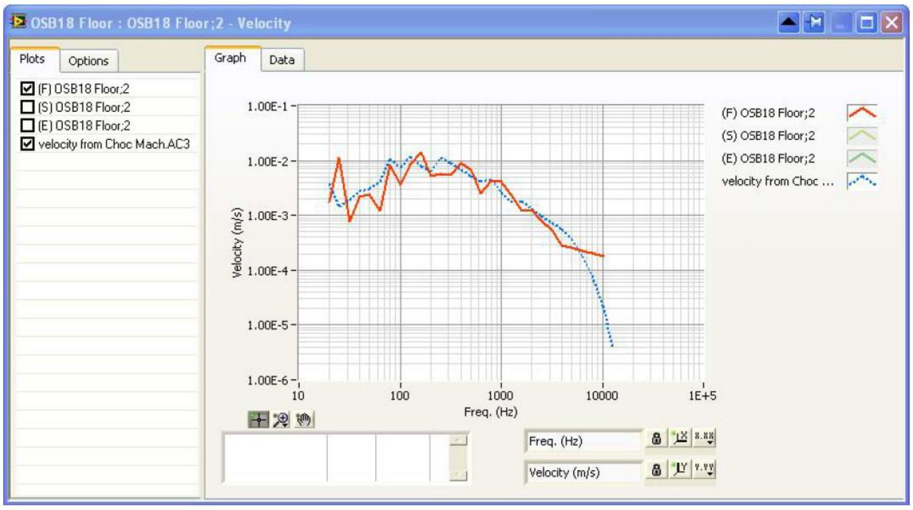

Figure 3.61: Predicted (red) and measured (dashed blue) mean rms velocity of the OSB18 panel under shock machine load

It is also possible to reconstruct floor vibration from SEA modeling, not only in frequency domain but also in time domain. For this, the SEA-Shock module, available in SEAWOOD as an extra calculation library, can build a representative time response from predicted real-valued frequency response functions (FRF) delivered by the SEA model of the Floor. As SEA deals with energy, all phase information is lost in the SEA model. However, SEA-Shock, thanks to its LMPR (local Modal Phase Reconstruction) algorithm, adds to the SEA FRF an artificial phase making it invertible from frequency to time domain. This technology has been specifically developed for Aerospace industry originally for predicting shock responses events due to separation of rocket stages during the flight [48].

As pyrotechnical devices are used for cutting rocket stage structures, it generates high levels of vibrations, instantaneous acceleration exhibiting peak responses of several thousands of g's. Predicting expected acceleration time histories in order to qualify rocket equipment to the shock event is thus a vital task in a launch vehicle program. SEA-Shock dedicated functions for predicting injected power from rocket separation devices were not directly usable to predict injected power from the tapping machine. It was still possible to scale some predefined time history taken in the databank of SEA-Shock to evaluate the tapping machine force in order to synthesize by numerical SEA simulation the mean time history of the floor acceleration. As shown in figure 3.62, simulated time responses from SEA-Shock are very similar to measured ones.

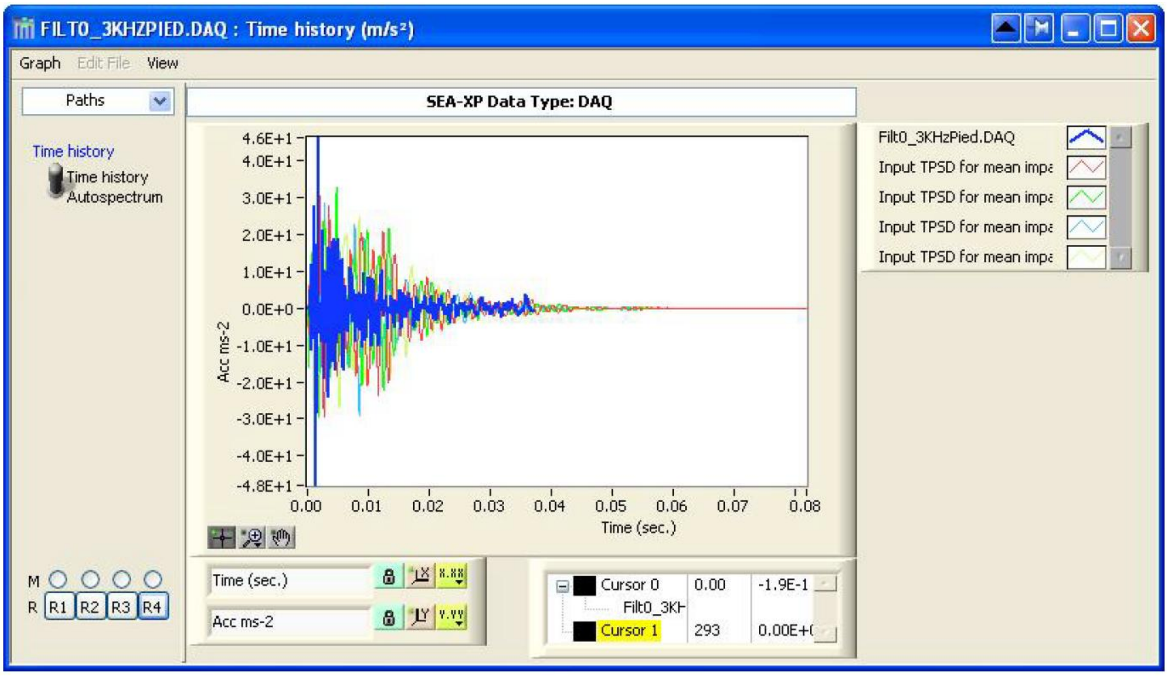

Figure 3.62: Synthesized and measured acceleration pulse (blue) when impacting the concrete floor

The identified forces are intended to feed input of a further theoretical SEA model of a building in order to predict noise annoyance resulting from such a source.

3.3 Use of standardized methods (Kij), Input EN 12354

3.3.1 Reverse SEA to predict flanking transmission in timber framed constructions

A common model to predict flanking transmissions is based on Statistical Energy Analysis (SEA), it has been elaborated for monolithic concrete walls forming a ‘T’ or a cross junction: EN 12354, [1], [2], [3]. In the standardized model each sub-system represents a wall. It has been shown that this model is accurate for heavy, homogenous and low damped structures such as concrete. The simplified theory can’t be applied for lightweight timber construction where walls are composed of double leaf ribbed panels and the junction composed of inhomogeneous assembly. A modified model was proposed to overcome this complexity.

In this chapter, we present a methodology using Reverse SEA with no simplification, where all parts of the construction is represented in the model. Through a progressive procedure, based on measurement, we build a hybrid prediction model composed of both experimental approach but also on experience. The experimental approach was carried out on Cross Laminated Timber (CLT) structure. The reason for that is due to an extensive expansion of the market for this type of building systems. CLT is more and more used and it fits well to high rise buildings in wood. Hence, it has opened a new capacity for wood to be used for multi-storey buildings.

3.3.2 Flanking transmission prediction

Flanking transmission in buildings contribute to large extent to sound transmission through partitions, often up to 50% of the total transmission. Flanking transmission has been studied a lot over the years and several calculation approaches are available in the literature. The more common model is based on a simplified SEA application.

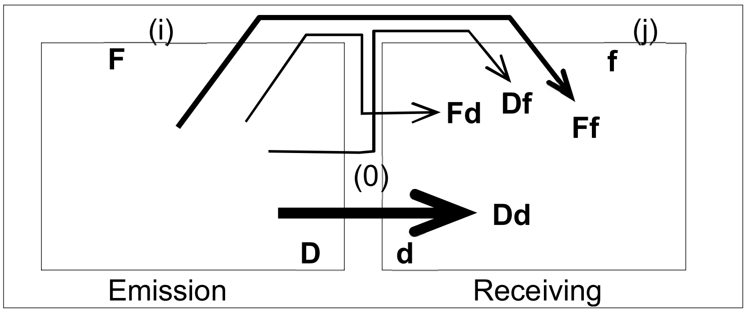

Figure 3.63: Conventional designation of direct and flanking transmissions

For homogeneous walls perfectly assembled a T junction creates an SEA model of 5 sub-systems: 2 cavities (rooms) and 3 walls forming the junction. Each path corresponds to a noise reduction:

$$\tau_{ij}=\sqrt{\left(\tau_i \tau_j d_{ij} d_{ji} \frac{S_j S_i}{S_0^2}\right)}$$

with R = 10 Log ($1/\tau$):

$$R_{ij}=\frac{R_i}{2}+\frac{R_j}{2}+\frac{D_{ij}+D_{ji}}{2}+10\log\frac{S_0}{\sqrt{S_i S_j}}$$

In case of light weight constructions, the vibration transmission through double walls, implies that the model used must be different. In year 2000, the European standard EN12354 was published, and this calculation model uses:

R, Sound transmission loss of wall and floors,
T_s, Structural reverberation time,
K_{ij}, Vibration reduction index.

K_{ij} is specific to junction type. It is for homogeneous heavy weight structures

$$K_{ij}=\frac{D_{ij}+D_{ji}}{2}+10\mathrm{Log}\frac{l_{ij}}{\sqrt{a_i a_j}}$$

With an equivalent absorption length:

$$a_i=\frac{2.2\pi^2 S_i}{c_0 T_s}\sqrt{\frac{f_{ref}}{f}}$$

For lightweight walls and floors the method proposes K_{ij} formulas, since they are strongly damped:

$$K^{"}_{ij}=\frac{D_{v,ij}+D_{v,ji}}{2}+10Log\frac{l_{ij}l_0}{\sqrt{S_i S_j}}$$

and

$$R_{ij}=\frac{R_i}{2}+\frac{R_j}{2}+K^{"}_{ij}+10\log\frac{S_0}{l_{ij}l_0}$$

In 2007, a new network of researchers within wood started. The network was organized within COST, in the action FP0702 aiming at developing the tools for use of wood in multi storey buildings. One working group, working group 1 (WG 1) was working on prediction tools The working group aimed at finding more appropriated prediction method adapted to timber framed construction. The group studied a number of approaches using FEM, SEA, Reverse SEA and Virtual SEA, and the outcome from the COST action opened for several new research ideas and created a new generation of projects, such as Silent Timber Build.

$D_{v,ij}$ (vibration reduction level) is measured in situ through junctions. The measurement method is normally based on a uniform mechanical excitation using several hammer or shaker positions. $D_{v,ij}$ are measured using 12 transducers positions.

The sound transmission loss resulting of all passes is calculated with:

$$R'=-10\log\left[10^{-\frac{R}{10}}+\sum_{ij}10^{-\frac{R_{ij}}{10}}\right]$$

And finally, the sound standardized level difference is obtained with R':

$$D_{nT}=R'-10\log\frac{0.16\ V}{T_0 S_s}$$

In the following, an SEA method for direct prediction is presented and also a reverse

SEA for determination of the characteristics.

3.3.3 SEA theory for lightweight building prediction

Statistical Energy Analysis theory involves subdividing the structure into subsystems and decomposing the frequency spectrum into third-octaves or octaves. In this way, the exchange of energy flow in the substructures can be analyzed. The parameters that decides the power flow vibrational transmission between subsystems are the damping and the coupling loss factors, and they are identified experimentally by reversing the direct SEA problem as exposed in next paragraphs.

Using Direct SEA, the modeling starts by decomposing the system into a set of components (the subsystems). For each of them the dynamical behavior is predicted by SEA. Each subsystem is classically defined by:

- a modal density, N, that represents the statistical local resonances of the subsystem,
- a damping loss factor, η or DLF, which represents the fraction of power loss in steady-state.

The exchange of vibrational power between two coupled subsystems i and j is described by a pairs of coupling loss factors (η_{ij} and η_{ji} or CLF) related by a reciprocity relationship:

$$\eta_{ij} N_i = \eta_{ji} N_j$$

The total vibrational energy in a subsystem, can be derived from its spaced and frequency averaged velocity v^2 (the measurable engineering quantity and its total mass m) by the relationship:

$$E = mv^2$$

E represents the total energy stored in resonant modes in a given frequency band of analysis which will be assumed to be centered around a radian frequency ω and the acoustic pressure is related to velocity in cavities by

$$p = \rho c \cdot v$$

In this band, SEA states that the exchange of power between coupled subsystems can be expressed as

$$P_{ij} = \omega\left[\eta_{ij} N_i \varepsilon_i - \eta_{ji} N_j \varepsilon_j\right] = \omega N_i N_j \beta_i^j \left[\varepsilon_i - \varepsilon_j\right]$$

Where β_i^j is the mean modal coupling loss factor between one pair of local modes of subsystems i and j and ε_i the mean modal energy. From this,

$$\eta_{ij} = \beta_{ij} N_j$$

Knowing all modal densities, DLF and CLF, it is possible to predict the energy state of the fully coupled system excited by external forces by writing a set of energy balanced equations traducing the energy conservation in each subsystem:

$$\frac{P_i}{\omega} = \eta_i E_i + \sum_{\mathrm{j}}^{\text{All j coupled to i}} \left\{ \eta_{ij} E_i - \eta_{ij} E_j \right\}$$

where P_i is the power delivered in subsystem i by its applied external forces.

This theory, “**Direct SEA**”, is used to predict energy flow between subsystems. The energy is converted into pressure level for cavities or rooms and into vibration levels for flexural plates.

To predict flanking transmission it is necessary to create substructures of the building in a safe manner and then introduce the accurate DLF and CLF of flexural plates and junctions. Below, it is described how DLF and CLF can be determined by testing the structure, using **Reverse SEA**.

3.3.4 Reverse SEA used to determine CLF and DLF SEA theory for lightweight building prediction

When the structure is divided into substructures it is possible to measure damping and coupling loss factors corresponding to the physical studied structure, by using the theory “Reverse SEA”. The methodology is well known, but currently not used to large extent. The testing is time consuming if a Reverse SEA software is not available for use. In Silent Timber Build approach, the Experimental SEA software developed by InterAC in Toulouse was used. To determine [η], DLF and CLF matrix energy and power injected are measured.

Experimental methodology

(1) Power is injected sequence by sequence in each subsystem of the structure

(2) Equilibrium of each configuration – power injected – is written

(3) n equations are derived,

Below we show the methodology for two subsystems:

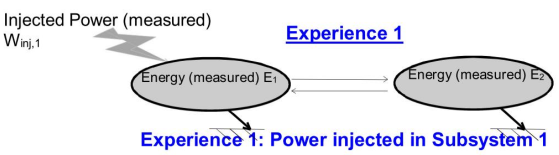

Experience 1: Power injected in Subsystem 1

$$\begin{bmatrix} -\eta_1 * & \eta_{21} \\ \eta_{12} & -\eta_2 * \end{bmatrix} \begin{pmatrix} E_{11} \\ E_{21} \end{pmatrix} = \begin{Bmatrix} \dfrac{-W_{inj,1}}{\omega_0} \\ 0 \end{Bmatrix}$$

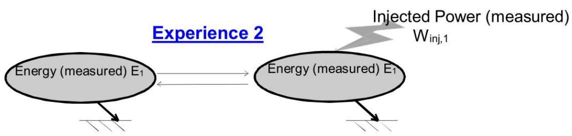

Experience 2: Power injected in Subsystem 2

$$\begin{bmatrix} -\eta_1 * & \eta_{21} \\ \eta_{12} & -\eta_2 * \end{bmatrix} \begin{pmatrix} E_{12} \\ E_{22} \end{pmatrix} = \begin{Bmatrix} 0 \\ \dfrac{-W_{inj,2}}{\omega_0} \end{Bmatrix}$$

Figure 3.64: Experimental methodology for Reverse SEA

Combining both equations, it becomes as follow:

$$\begin{bmatrix} -\eta_1 * & \eta_{21} \\ \eta_{12} & -\eta_2 * \end{bmatrix} \begin{pmatrix} E_{11} & E_{12} \\ E_{21} & E_{22} \end{pmatrix} = \begin{Bmatrix} \dfrac{-W_{inj,1}}{\omega_0} & 0 \\ 0 & \dfrac{-W_{inj,2}}{\omega_0} \end{Bmatrix}$$

Then the [ηij] matrix coefficient determination is done:

$$\begin{bmatrix} -\eta_1 * & \eta_{21} \\ \eta_{12} & -\eta_2 * \end{bmatrix} = \begin{Bmatrix} \dfrac{-W_{inj,1}}{\omega_0} & 0 \\ 0 & \dfrac{-W_{inj,2}}{\omega_0} \end{Bmatrix} \begin{pmatrix} E_{11} & E_{12} \\ E_{21} & E_{22} \end{pmatrix}^{-1}$$

For n subsystems:

$$\begin{bmatrix} -\eta_1^* & \eta_{21} & . & . & \eta_{n1} \\ \eta_{12} & -\eta_2^* & & & . \\ . & & . & & . \\ . & & & . & . \\ \eta_{1n} & . & . & . & -\eta_n^* \end{bmatrix} = \begin{Bmatrix} \dfrac{-W_{inj,1}}{\omega_0} & 0 & & 0 \\ 0 & \dfrac{-W_{inj,2}}{\omega_0} & & 0 \\ & & . & 0 \\ 0 & 0 & 0 & \dfrac{-W_{inj,n}}{\omega_0} \end{Bmatrix} \begin{pmatrix} E_{11} & E_{12} & . & E_{1n} \\ E_{21} & E_{22} & . & \\ . & & . & \\ E_{n1} & & & E_{nn} \end{pmatrix}^{-1}$$

This testing methodology for different types of building systems were conducted within the project: double leaf timber framed wall, I beam framed floors, T junction of 3 framed walls and a cross junction between 4 apartments composed of 2 walls and 2 floors.

CLF and DLF govern the energy flow in the structure. With measured CLF and DLF we can construct a SEA model to predict the transmitted vibration in a junction. With local physical characteristics we can calculate global vibration levels of a wall and thus determine the $D_{v,ij}$ vibration transmission factor between two walls or between a wall and a floor, depending on the structural junction. And thus coupling and damping loss factors can be converted into $D_{v,ij}$ and further to K_{ij}.

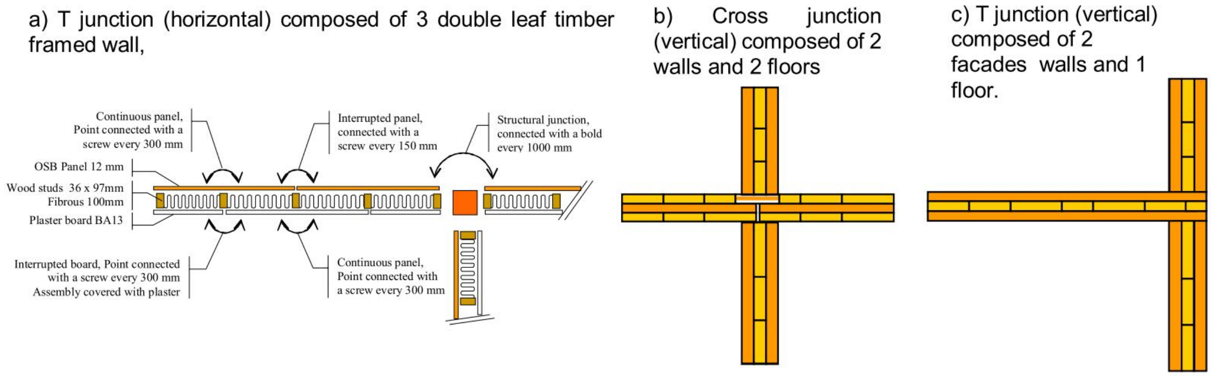

Figure 3.65: Example of three tested building systems

Results for a cross junction are presented below, both using Reverse-SEA and the standardized method of EN 12354.

3.3.5 Measurement of coupling and damping on a CLT building

In order to characterize junctions in real buildings, Silent Timber Build has collected measurements through the industrial partner Rothoblaas, see figure 3.69, but also specifically measured in-situ in some different buildings erected by French building companies (Woodeum / PROMICEA). It is planned to proceed at different stages during structural implementation, however in this report only the first stage carried out in February 2016 in Ris-Orangis, France, is presented. The measurements were made on the structure without lining. The campaign took place during night due to the need of quietness on a structure composed of Cross Laminated Timber (CLT) panels for walls and floors, see figure 3.65; b) and c).

Figure 3.66: Tested building systems, CLT walls and floors

For analyzing the measurements and to extract the results, the software SEA-XP® developed by the project partner InterAC, was used. The tool is very convenient to use, Reverse SEA generates hundreds of files comprising: recorded force, acceleration, mobility, power injected, FRF, Each hammer shock is recorded with all associated accelerations. First step is to measure the mobility for the power injected calculation. Second step, is to measure acceleration to identify energy flow between subsystems.

In this report results are presented on a cross junction composed of 4 subsystems:

- subsystem 1 = floor of apartment 1,
- subsystem 2 = separative wall between apartment 1 and 2,
- Subsystem 3 = floor of apartment 2,
- Subsystem 4 = separative wall between apartment 1 and 2 of lower storey,

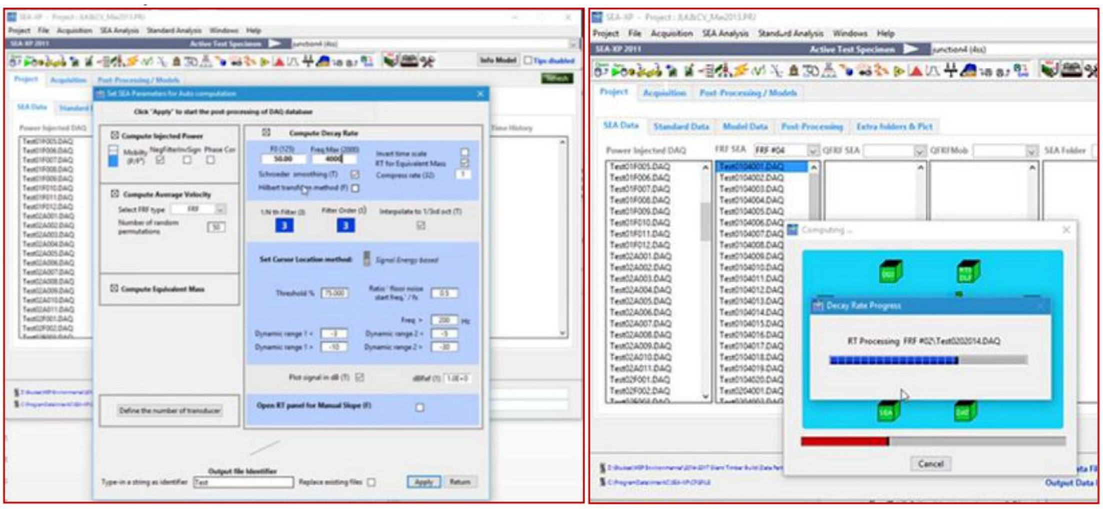

Figure 3.67: Processing from data acquisition to reverse SEA

The software guides the operator team during the measurement and then it manages all files recorded in order to extract CLF and DLF. The testing of each junction takes 2 hours for measurement (preparation and acquisition). We start with data acquisition: hammering the subsystems surface (1 to 4), all measurement are stored and labelled automatically. After the data acquisition on the four subsystems, the tool reverses the Energy matrix * Power injected resulting on DLF and CLF matrix.

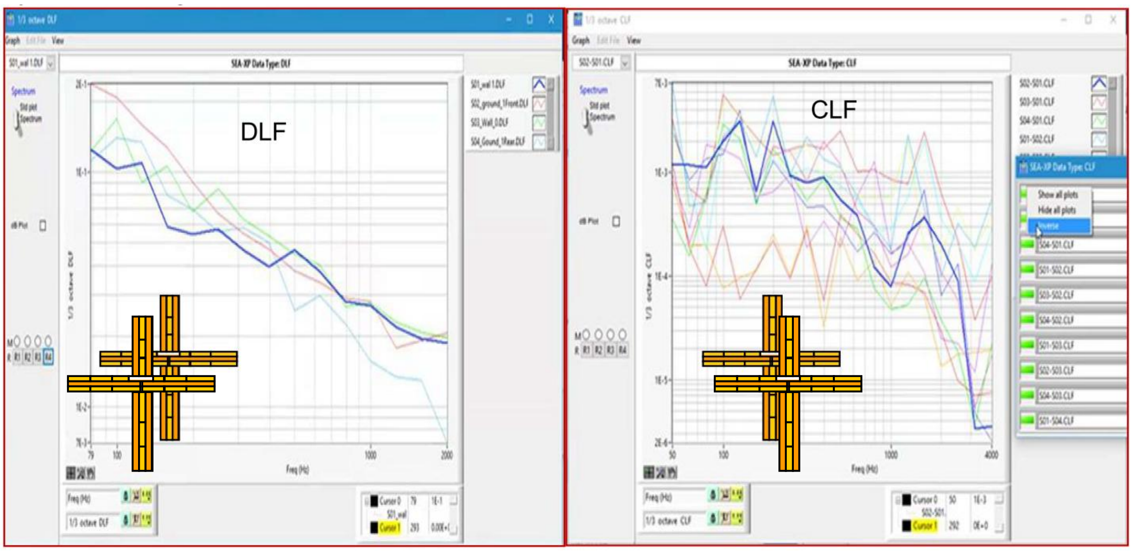

Figure 3.68: DLF and CLF measured on a CLT cross junction of 2 walls and 2 floors

As described earlier the experimental procedure ends up with CLF and DLF that can be implemented into a model in order to calculate transmission through various junctions. The model composed of deterministic and measured couplings is dedicated only for vibration energy flow analysis. For acoustical usage, acoustical cavities are added into the model in order to represent emission rooms and receiving rooms as well as cavities between panels in double wall. With this approach it is then possible to calculate the different sound transmission losses R_{ij}, both direct paths and flanking paths.

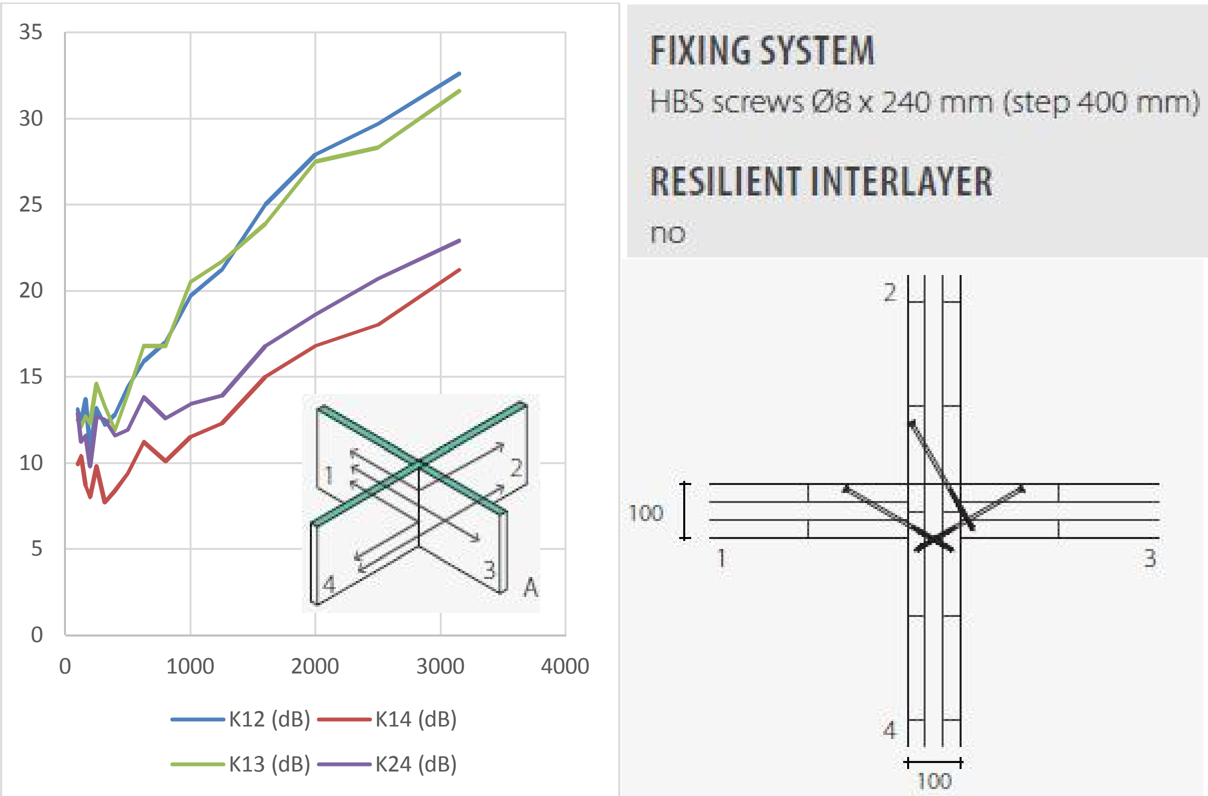

Figure 3.69: Kij, Vibration Reduction Index, measured on a CLT cross junction of 4 walls

3.3.6 Conclusions

The prediction method, using SEA for evaluating the flanking transmissions of mass timber wood based structures (CLT walls and floors) has been presented. SEA is the theory framework that fits for homogeneous construction. However, considering more complex constructions, such as lightweight timber framed structures, the simplified SEA theory is not appropriate. In that case an original methodology using subsystem identification and reverse SEA to model a typical junction, is proposed.

Reverse SEA method opens up interesting perspectives for acoustic engineering and its results are directly appropriate for the construction industry. All the modeling expertise, characteristics, CLF and DLF database, are being implemented in SEAWOOD model, where typical cases for building modeling are studied within the Silent Timber Build Project.

Further work would be to group all measurements on flanking transmissions performed on wood structures in order to create a database. This would be convenient for building design. Today one can find easily sound transmission loss measurements as well as impact nose reduction measurements. But still building design needs also vibration reduction indexes to perform calculation using the European standard EN 12354.

4 Analysing input power

This section describes experimental investigations and related post-processing for identifying mechanical forces exerted by a typical tapping machine on a floor. The identified forces are intended to provide input for a more precise theoretical SEA model. This is necessary in order to correctly predict noise annoyance due to impact sound in a building.

4.1 Characterizing Tapping Machine

The tapping machine used as exciter during the testing is the Bruel&Kjaer machine type 3207 equipped with five hammers as shown in figure 4.1.

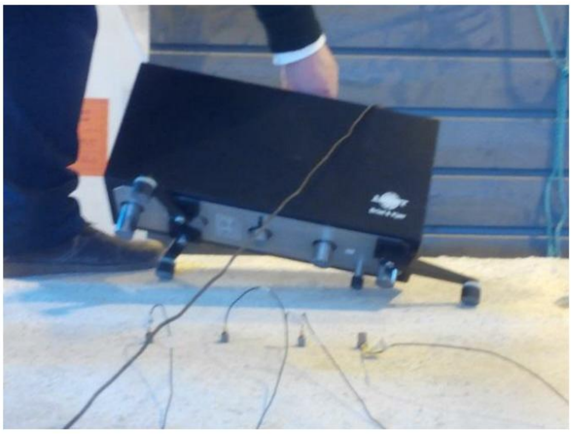

Figure 4.1: B&K tapping machine used as exciter

4.1.1 Impact hammers

In order to excite the floors with a known vibrational power, two impact hammers equipped with force cells were used. The first one is a mid-sized Kistler hammer for mid and high frequencies (InterAC equipment) and the second a Dytran large-sized hammer (FCBA equipment) for exciting low frequencies. The Kistler hammer is shown in figure 4.2.

Figure 4.2: Operating power injection measurement with the Kistler hammer

4.2.1 Transducers

When actuating the impact hammers, their forces are recorded thanks to their built-in force transducers. Simultaneously, the acceleration is recorded at various predefined points on floors using different types of ICP accelerometers: one Kistler 50 mV/g, three B&K 100 mV/g and one B&K 10 mV/g.

Acquisition system

Data are acquired by a National Instruments 4-channel USB board connected to a notebook and driven by SEA-XP 2014 acquisition software from the project partner InterAC, dedicated to experimental SEA measurements, see figure 4.3. Transfer functions and time histories under the applied force of the impact hammer are recorded. The length of the time windowed signals was set to 4k-samples at 50 kHz rate. Time histories under shock machine excitation are recorded with time windowed signals of 32k-samples at 25 kHz rate.

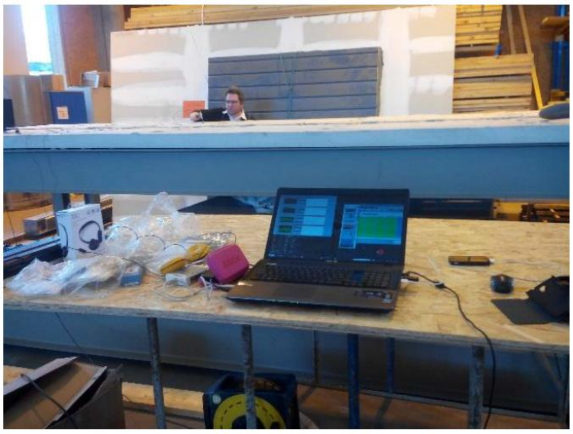

Figure 4.3: Notebook and card driven by SEA-XP software

Tested floors

The first test series is performed on a concrete floor (typically 1 m x 6 m flat piece of 9 cm concrete supported by metallic I-beams). The concrete floor is shown in figure 4.4.

Figure 4.4: Concrete floor with accelerometer and shock machine in extreme right position

A second test series was performed on a flat panel of OSB18 supported on two resilient layers. The OSB floor setup is installed on top of the concrete slab.

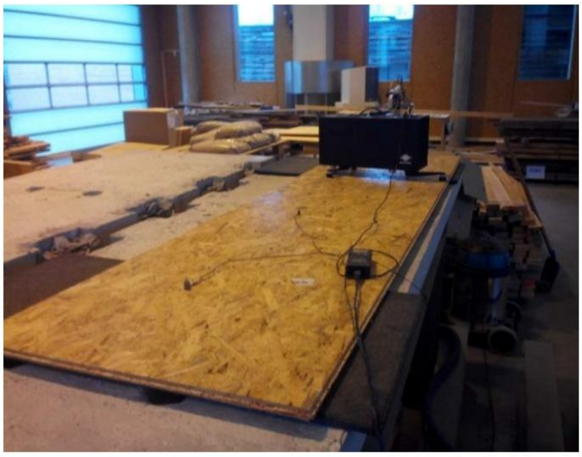

Figure 4.5: OSB 18 panel mounted on resilient layers and tapping machine in extreme right position

Test sequences

Concrete floor test sequences

The concrete floor behavior is first investigated by measuring transfer frequency responses functions under the impact hammers (see section 4.1.1). The aim is to estimate the damping loss factor (DLF) of the concrete floor, its driving point mobility and the mean transfer squared velocity under this controlled input. Since the concrete floor is very stiff, the two impact hammers are successively used, the large hammer giving better noise/signal ratio in LF range (but with cut-off frequency around 1 kHz) while the mid-sized hammer is providing response ranging between 500 Hz up to 3000 Hz. Additionally, the tapping machine is placed in four different positions on the floor and simultaneously four transducers are attached in the middle of the concrete floor

Figure 4.6: The four fixed location accelerometers used when the tapping machine is placed on the floor

OSB floor test sequences

Identical sequences are “reiterated” as the OSB floor is added, while skipping the large hammer sequence since the signal to noise ratio is normally satisfactory using the mid-sized hammer on this light-weighted floor when attached as described earlier.

Figure 4.7: OSB floor during hammer test using mid-sized hammer

4.2 Post-processing data

4.2.1 Concrete floor analysis

The response is analyzed under mid-sized and large-sized impact hammers

Post processing of recorded data is performed by the SEA-XP software. SEA-XP generates the SEA parameters from the measurements described previously. SEA-XP provides:

- The conductance *Y* (injected power/unit force) computed in frequency domain as real part of mean FRF V/F at driving point

- The mean squared transfer velocity $<v^2>$ computed in frequency domain from modulus $|V/F|^2$ averaged over various locations of accelerometer and hammer impact over the floor domain

- The mean reverberation time in the floor (computed from FRF impulse response) and transformed into apparent DLF and equivalent mass
- From previous data, the experimental SEA model of the floor (1-subsystem model) is generated and solved. On output, it gives a DLF computed as: $\eta(\omega) = \dfrac{Y}{\omega m \left\langle v^2 \right\rangle}$

The two hammers show different validity bandwidth: large-sized hammer gives a correct response up to 800 Hz and the mid-sized hammer up to 2500 Hz. Between 100 and 800 Hz, data from large and mid-hammers are geometrically averaged as both measurements are valid but still depending on location due low modal density of the concrete floor. Below 100 Hz only large hammer data are retained and symmetrically above 800 Hz only mid-hammer data are retained. Measured and averaged conductance spectra are given in third octave bands in figure 4.8. DLF averaged over tests is given in Figure 4.11: Mean damping loss factor (DLF) of the concrete floor averaged over LH and MH tests

4.9. DLF is approximately 10% at 100 Hz and shows a decaying slope (5% value at 1000 Hz).

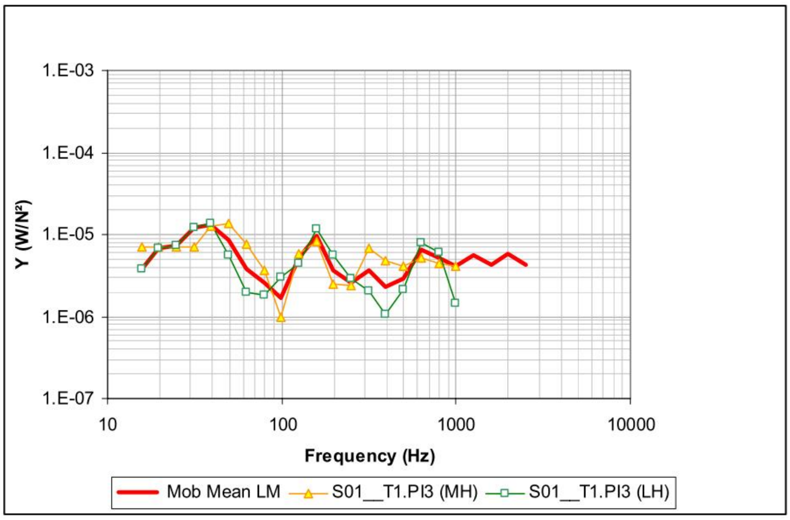

Figure 4.8: Conductance measured at driving points with large (LH) and mid-hammers (MH) and averaged

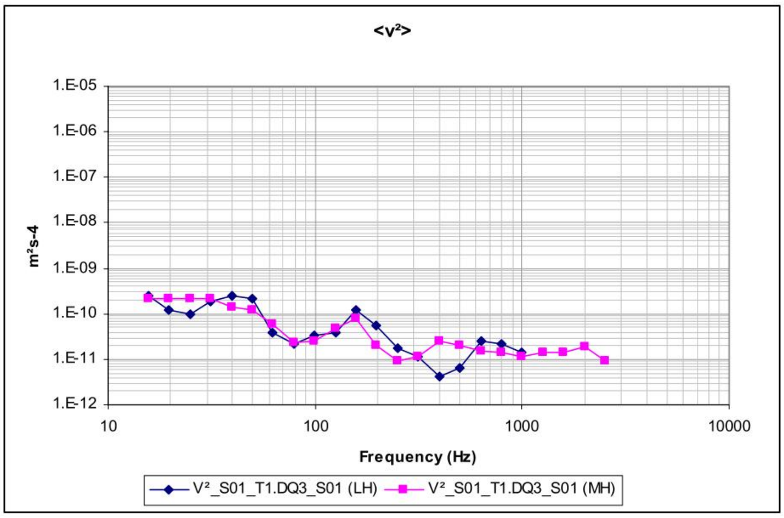

Figure 4.9: Mean squared velocity of the floor under impact measurement with large and mid-hammers

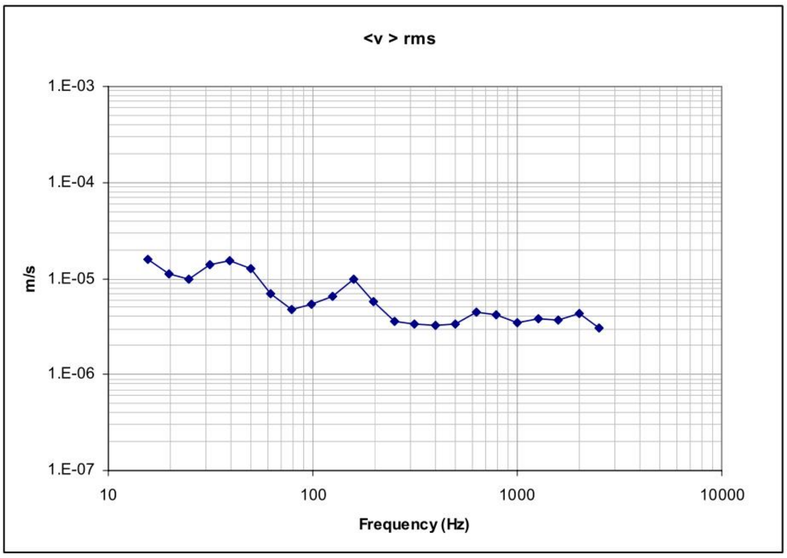

Figure 4.10: Mean rms velocity of the floor averaged over LH and MH results

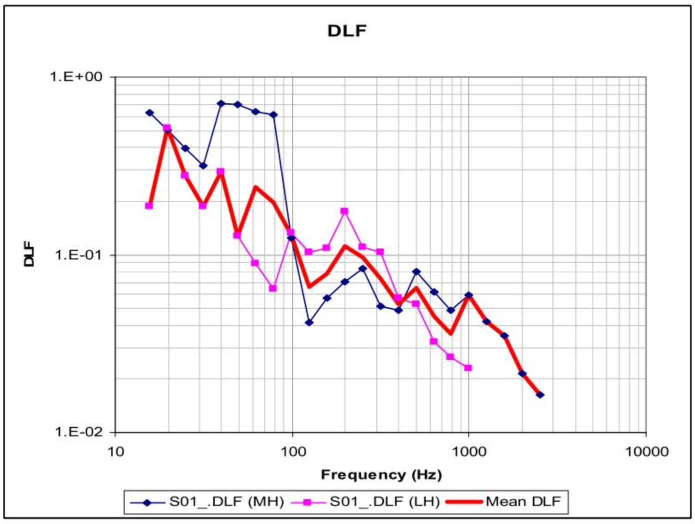

Figure 4.11: Mean damping loss factor (DLF) of the concrete floor averaged over LH and MH tests

Analyzing response under B&K shock machine

The tapping machine response is recorded from 4 different source positions. Peak time histories are dropping by a factor of 3 between position 1 and 4, see figure 4.12.

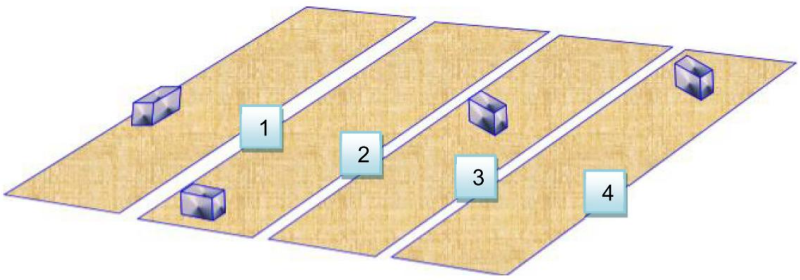

Figure 4.12: Shock machine in last position and the four accelerometers at fixed location

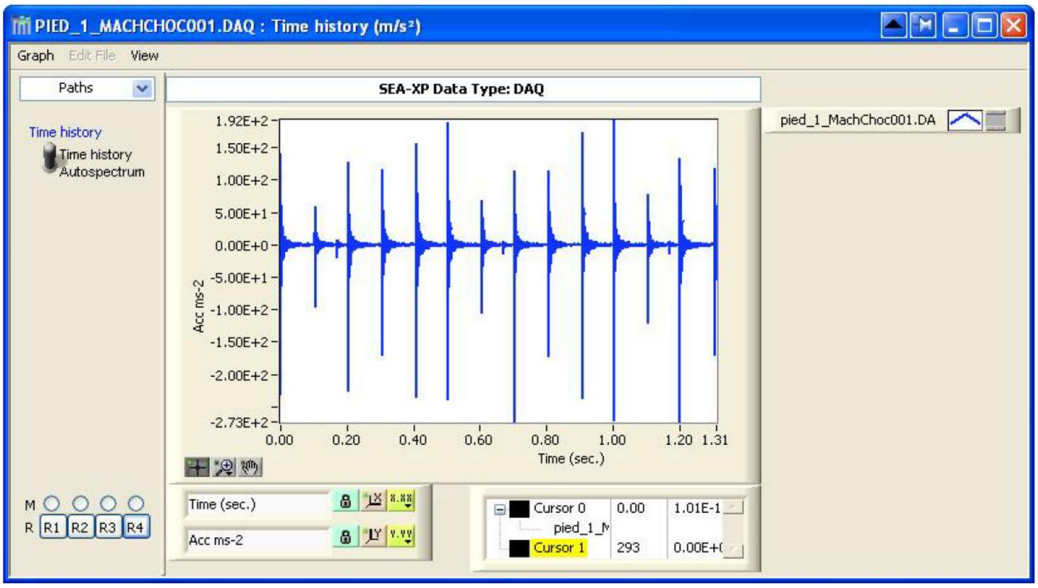

Figure 4.13: Acceleration time history of first accelerometer in nearest position from shock machine (about 20 cm)

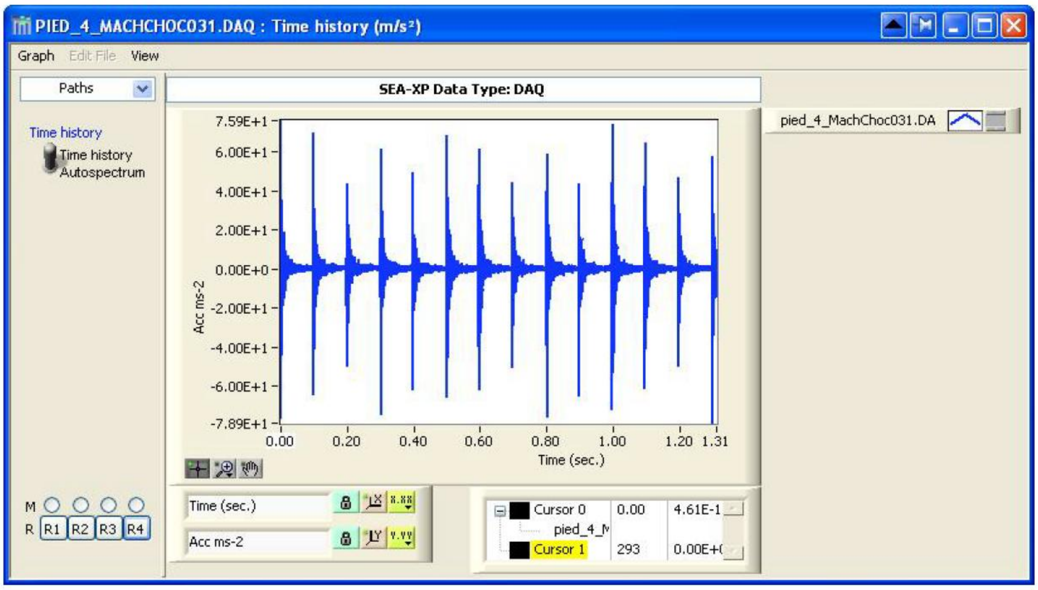

Figure 4.14: Acceleration time history of first accelerometer in furthest position from shock machine (about 20 cm)

The mean autospectrum Svv is computed in narrow band from all recorded time histories and for all positions and the results are shown in figure 4.15.

Figure 4.15: Autospectrum of the mean acceleration response to shock machine computed from all recorded time histories

The mean rms velocity of the concrete floor to the shock machine excitation is calculated from:

$$\langle v^2(f,\Delta f)\rangle = \sqrt{\frac{1}{\omega_c^2}\int_{\Delta f} S_{vv}(f)df}$$

Related spectrum is shown in Figure 4.16: Mean velocity rms response of the concrete floor to shock machine (in 1/3rd octave band A

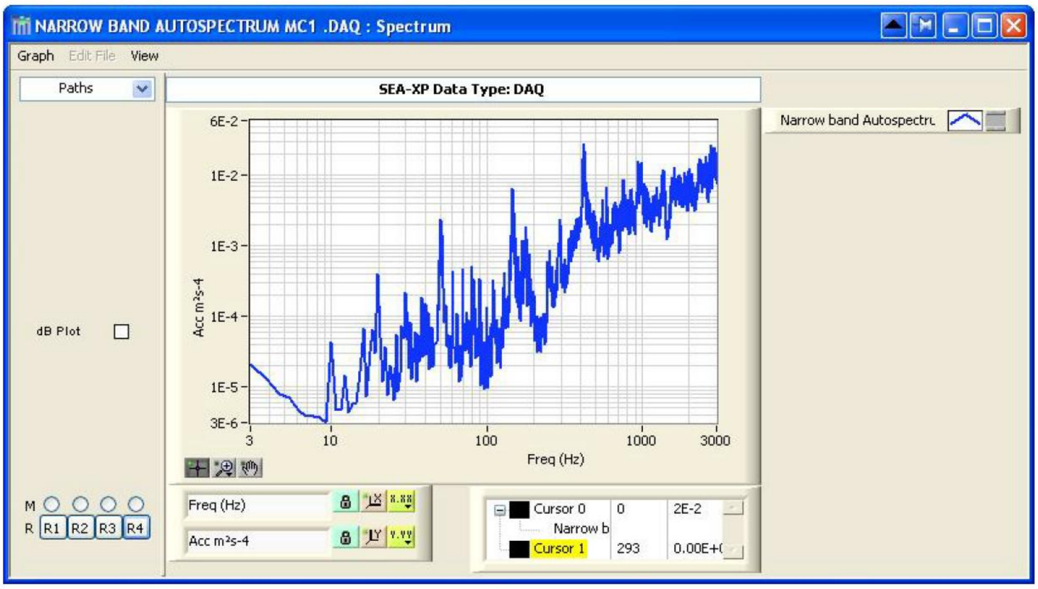

Figure 4.15: Autospectrum of the mean acceleration response to shock machine computed from all recorded time histories

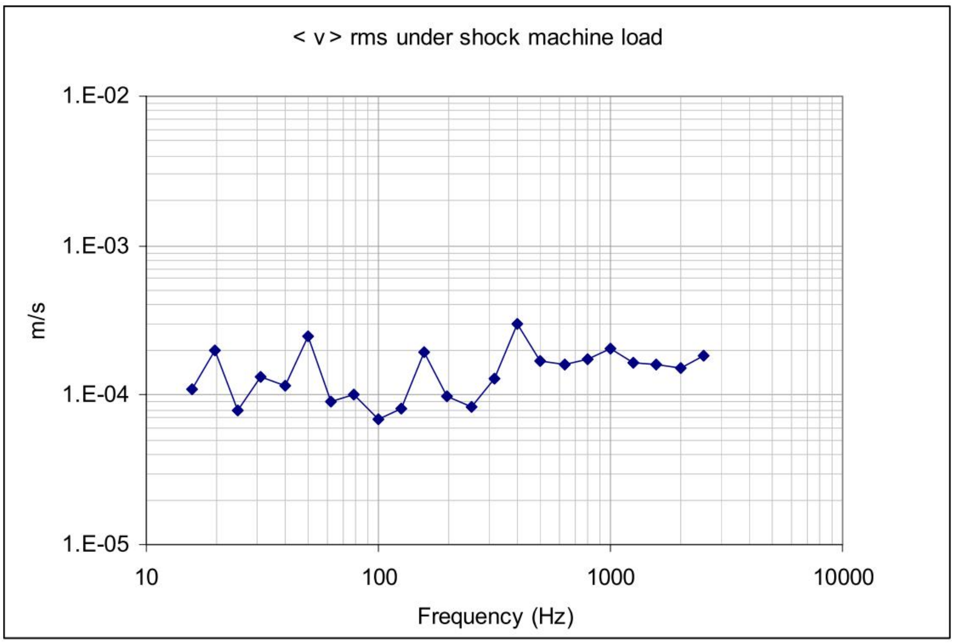

Figure 4.16: Mean velocity rms response of the concrete floor to shock machine (in 1/3rd octave band A

Equivalent force exerted by tapping machine on the concrete floor [1]

To extrapolate the force exerted by the tapping machine, the transfer $H_1 = <v^2>_1 / Y_1$ is first estimated from impact hammer tests in which Y_1 (the driving point mobility) was measured.

The transfer $H_2 = <v^2>_2 / P_2$ when the tap machine is acting on the floor is assumed to be very similar to H_1. It comes:

$$H_1 = <v^2>_2 / P_2 \Rightarrow P_2 = <v^2>_2 / H_1$$

where $<v^2>_2$ is the mean squared velocity response of the concrete floor. Assuming the tapering hammers generates a driving point mobility close-by Y_1, the rms spectrum of the equivalent tap machine force is then obtained from:

$$F_2 = \sqrt{P_2 / Y_1}$$

This is a reasonable estimate as soon as the time histories of the tapping machine hammers are well separated in time and do not interfere. The rms force spectrum calculated by this mean, is shown in figure 4.16.

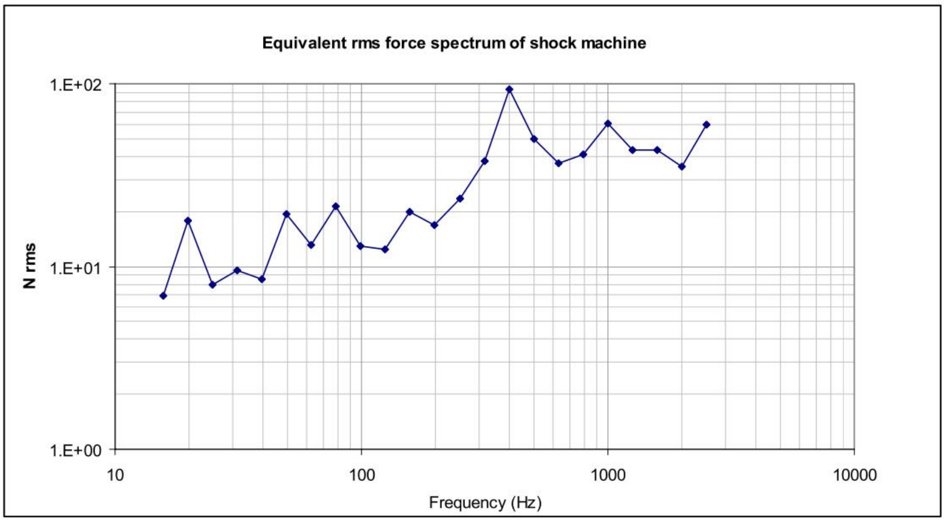

[1] *As tapering hammers have a larger impact area than an classic impact hammer force cell, some spatial wavenumber filtering is expected, that will tend to reduce at high frequency the level of driving point mobility, Y_2, compared to Y_1. In the high frequency when dividing by Y_1 in place of Y_2, a force with smaller high frequency content than original tap machine force would be expected.*

Figure 4.16: Equivalent rms force from the shock machine on the concrete floor (in third octave band)

Validation of force identification

To validate previous post-processing, a theoretical SEA model of the floor is built up. The SEA model is loaded with the measured power. Model output responses are then compared to experimental SEA results where all parameters are under control.

In particular, the measured SEA DLF is allocated to the floor subsystem, which is excited by the measured mean injected power, identified from the impact hammers. The elasticity characteristics of the concrete material are slightly adjusted from default values in order to correlate to the conductance measurements. The Young's modulus E is decreased from 1 E^{11} Pa down to 8 E^{10} Pa. The concrete density is kept to default (2300 Kg/m3).

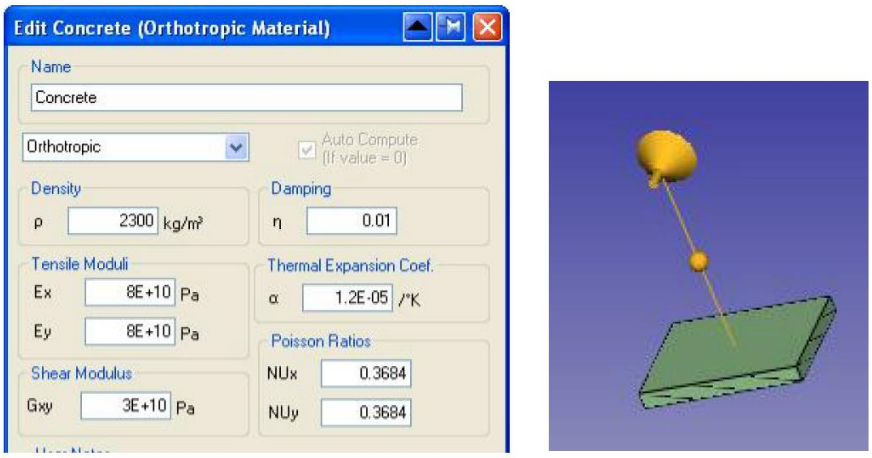

Figure 4.17: Material properties of SEA+ floor model for correlation with impact hammer tests

Corresponding SEA model of the floor is very simple, just one plate subsystem in 90-mm concrete with dimensions of 1 m x 6 m The plate is excited by the user-defined measured mean power. The calculated conductance (or rather the mobility) is compared with the measured mean value Y_1 in figure 4.18. Excellent agreement is found above the first mode of the floor, the latter being not predicted accurately by the analytical SEA model. The prediction of mean rms velocity response is compared with measured velocity in figure 4.19, and the agreement is also found excellent up to the highest frequency of the measurement (3000 Hz).

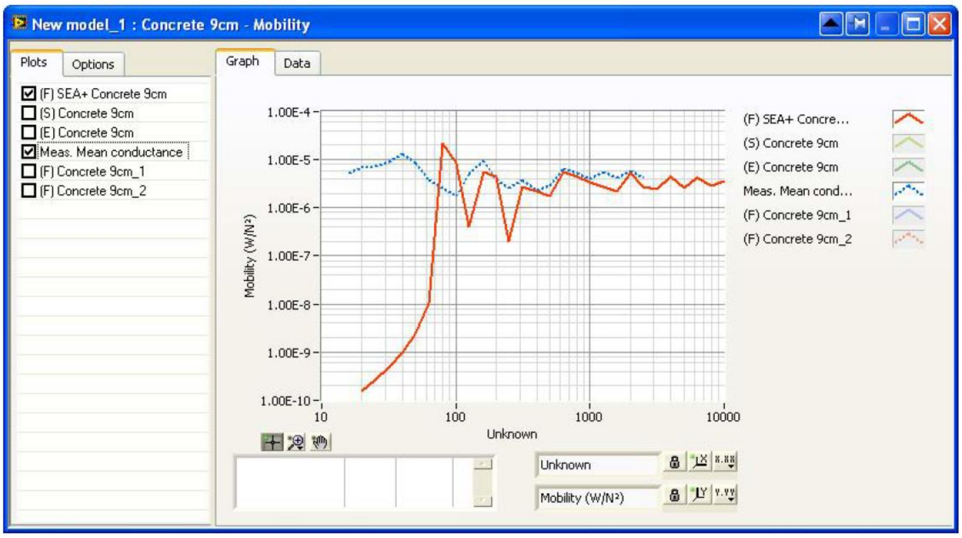

Figure 4.18: Conductances measured and predicted by the concrete floor SEA+ model

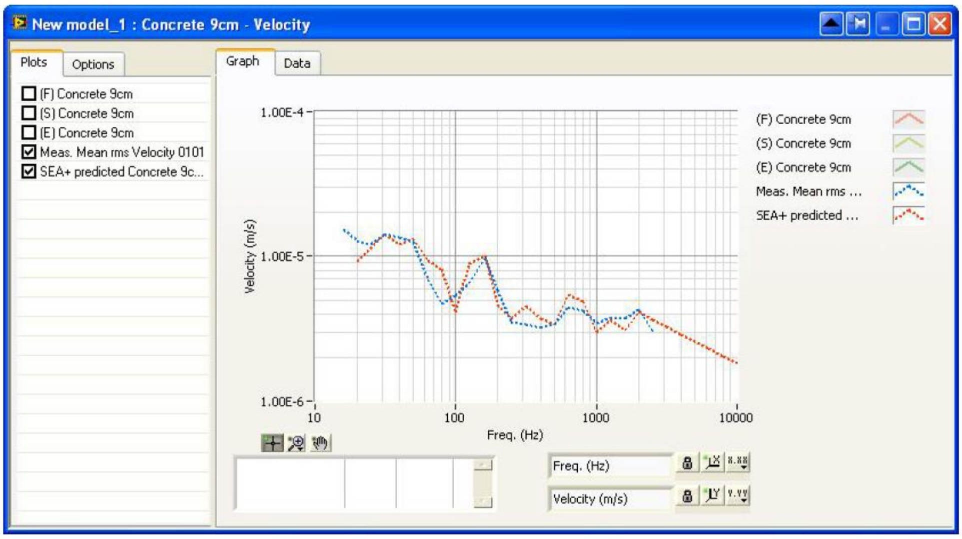

Figure 4.19: Mean rms velocity responses of the concrete floor measured and predicted by the concrete floor SEA+ model under measured injected power from impact hammer

Then, a second model was built, by simply applying to the same concrete floor subsystem the previously identified force from the tapping machine. The SEA+ model is now predicting the mean velocity response compared with measurement in figure 4.21. The excellent agreement above 40 Hz is validating our initial assumption that the tapping machine is behaving in the same way as the impact hammers.

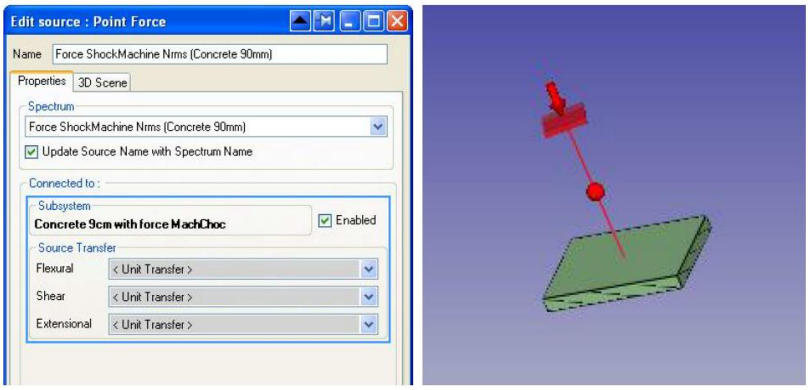

Figure 4.20: Applying the equivalent force of the shock machine as a point force to the concrete floor

Figure 4.21: Mean rms velocity responses of the concrete floor measured and predicted by the concrete floor SEA+ model under shock machine equivalent force

4.2.2 OSB18 floor analysis

Measurement analysis

The post-processing of the data is carried out similarly to the Concrete case: PIM method is applied to identify SEA parameters. Mean Conductance (i.e. real part of the driving point mobility), mean DLF and equivalent mass of the subsystem are then identified from FRF database generated with impact hammer. Mean Conductances are given in figure 4.22-1 for both the region where OSB panel is freely moving and for the region where it is supported by the resilient layer.

Figure 4.22-2 provides the standard deviation of these estimates which fixes the high frequency validity of the measurements to 2 kHz. High frequency conductance around 2 kHz seems higher in the region supported by resilient material but as it is the limit of the confidence interval, it is not sure that this is related to some supporting material effect.

The experimental DLF and the related equivalent mass are given in figures 4.23-1 and 4.23-2.

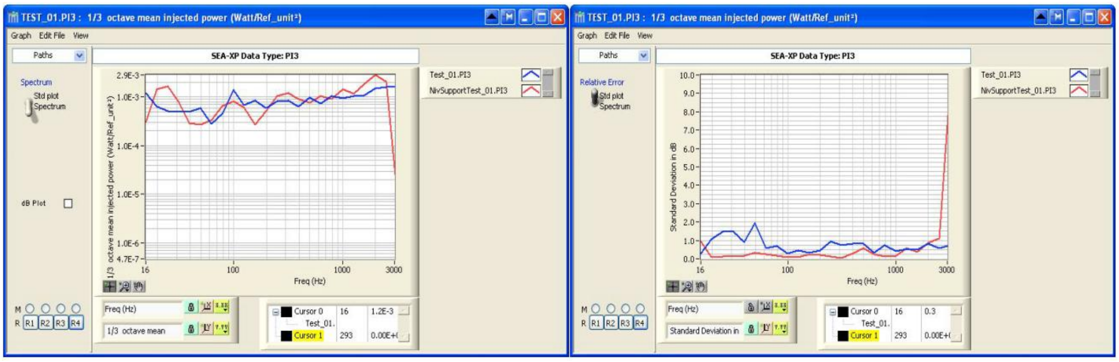

Figure 4.22: 1. In left diagram; Conductances measured on free OSB (blue) and in the region supported by the resilient material (red); 2. In the right diagram; related standard deviation given in dB around the mean value

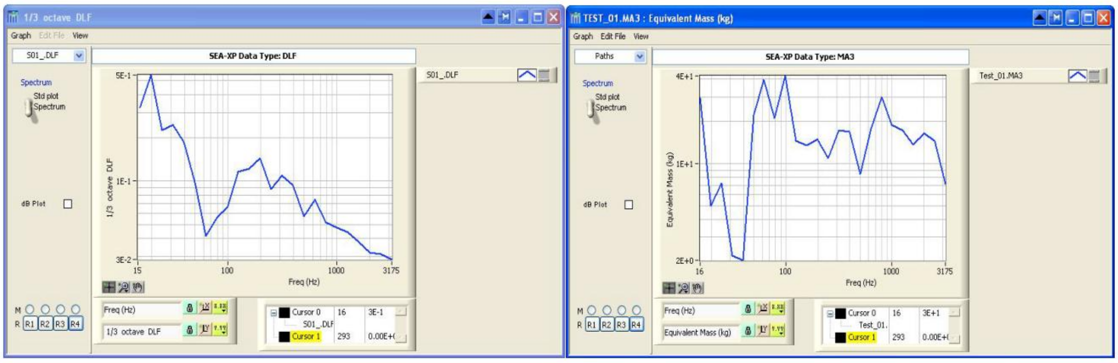

Figure 4.23: 1. In left diagram: DLF of OSB 18 from PIM measurement and; 2. in right diagram: equivalent mass.

Simulation of impact hammer

The default material properties of the OSB (18 mm) used in the floor SEA model are given in 4.24. In the same figure is also given the related measured and calculated conductances of the OSB floor model. The good agreement observed between measured and calculated conductances confirms that OSB chosen properties are near from actual values.

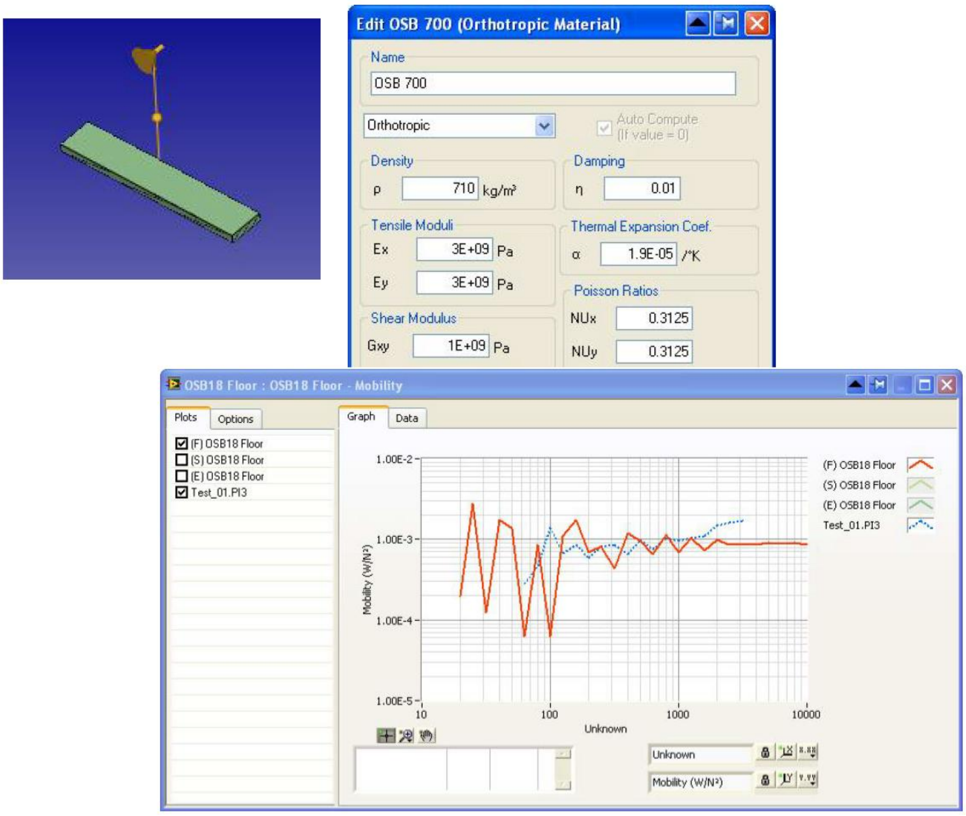

Figure 4.24: OSB properties on left and on right predicted and measured conductance of the 18mm OSB panel.

The measured DLF is now imported into the OSB subsystem and the predicted rms velocity is compared to measured rms velocity under measured impact hammer power in figure 4.25-1 and under unit impact hammer force in figure 4.25-2, as $\langle v^2 \rangle$ is normalized by the squared force spectrum in ESEA tests.

Above 2kHz, predicted and measured responses deviate from each other. This is most probably due to the previously observed differences in the predicted and measured high frequency conductances, the latter being valid up to 2 kHz.

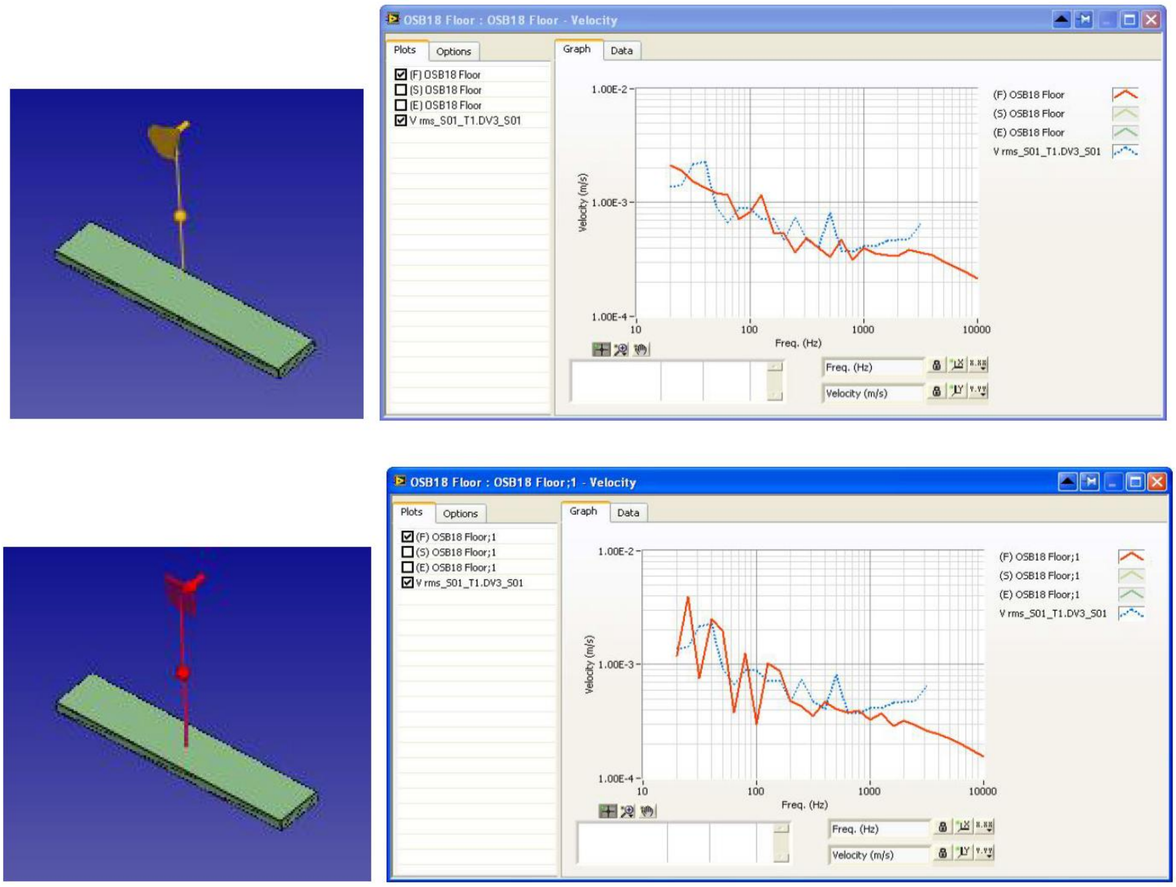

Figure 4.25: 1. The diagram on top: Prediction and measured mean velocity response of the OSB panel under measured injected power and 2. The lower diagram: Velocity response under unit force load.

Simulation of tapping machine excitation

In a similar way to the bare concrete floor, the mean velocity response of the OSB floor is computed from recorded acceleration time histories at the various locations of the tapping machine during normal operating conditions. The mean autospectrum of acceleration is given in narrow band in figure 4.26.

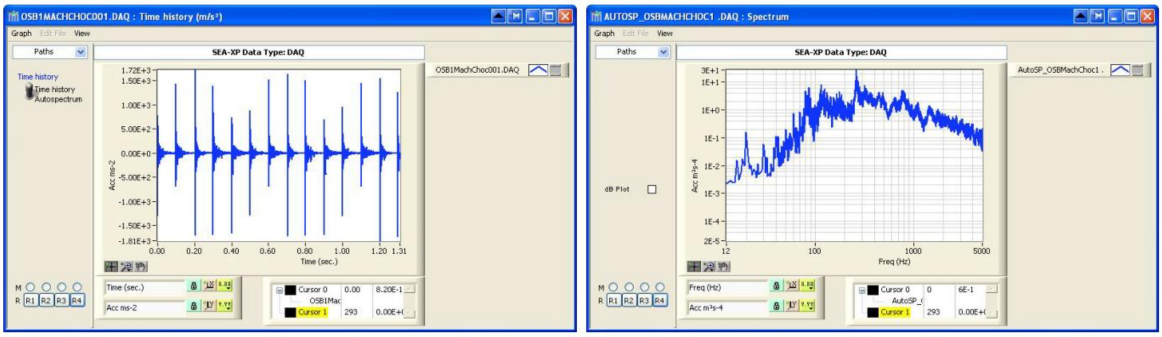

Figure 4.26: The diagram to the left: One particular time history record of the OSB acceleration response during normal operation of the tapping machine and Right Autospectrum of the left signal

The mean third octave velocity computed from previous autospectrum of figure 4.26 right is shown in figure 4.27.

Figure 4.27: Mean velocity response of OSB floor under operating shock machine load

The injected power of the shock machine P_S is then processed as:

$$P_S = P_H \frac{\langle v_S^2 \rangle}{\langle v_H^2 \rangle}$$

and the force is obtained as:

$$F^2{}_S = \frac{\langle v_S^2 \rangle}{\langle v_H^2 \rangle} \Rightarrow F = \frac{\sqrt{\langle |v_S^2| \rangle}}{\sqrt{\langle v_H^2 \rangle}} = \frac{\langle v_{S\_rms} \rangle}{\langle v_{H\_rms} \rangle}..$$

with *H* for "Hammer" and *S* for Shock (tapping) machine".

The related spectra are given in figure 4.28. When the equivalent force is applied to the OSB panel the predicted and measured mean velocity response are almost identical (see figure 4.29).

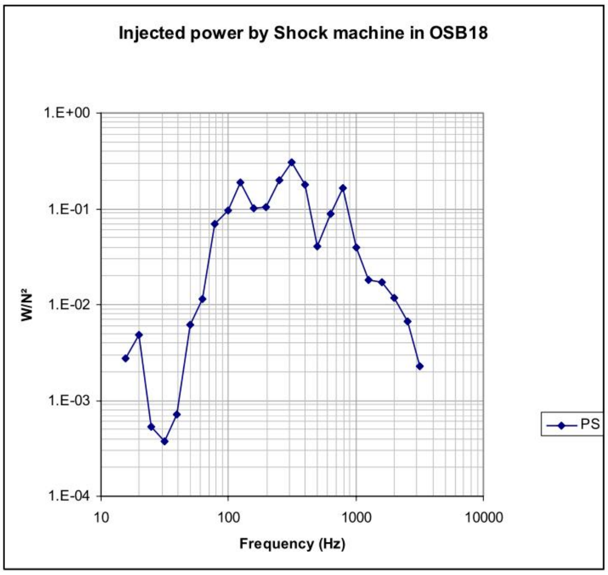

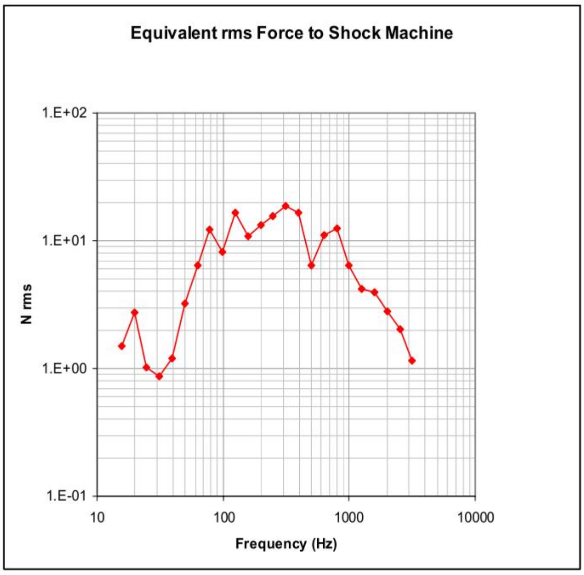

Figure 4.28: 1. Right graph is the injected power from the shock machine in OSB18 ; 2. Left graph is the related equivalent rms force generated by the tap machine

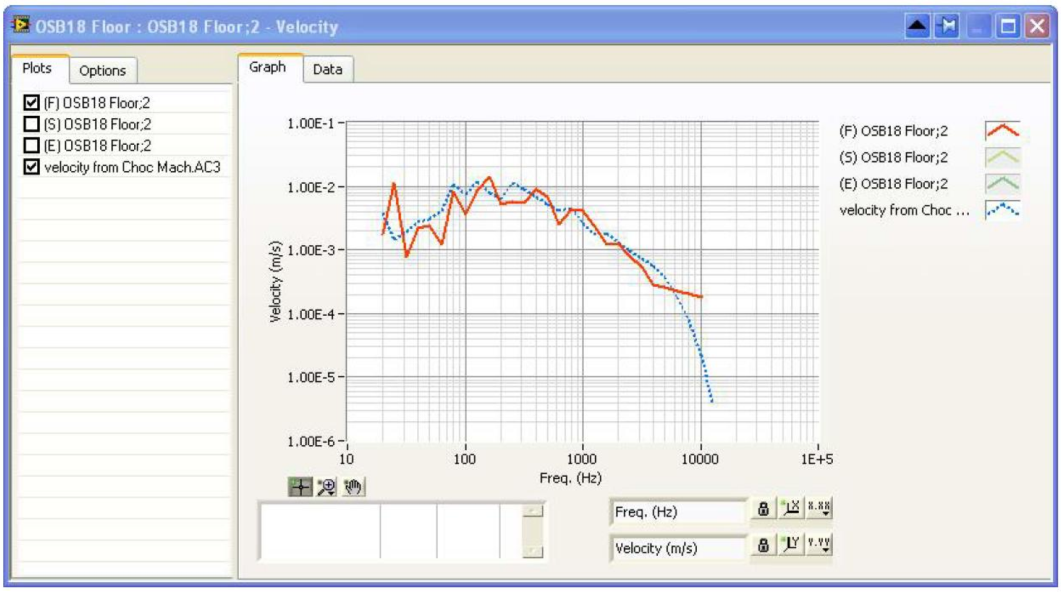

Figure 4.29: Predicted (red) and measured (dashed blue) mean rms velocity of the OSB panel under tapping machine equivalent force

4.2.3 Comparing forces from tapping machine on concrete slab and on OSB on top of concrete

The forces delivered by the shock machine are showing very different amplitudes and spectra, depending whether they are applied to the concrete slab or to the concrete slab equipped with the OSB floating floor.

The ratio of the tapping machine force, between the two floor setups, "Fconcrete/Fosb", is shown in figure 4.30. In the same figure this ratio is compared to the ratio between measured hammer forces recorded with mid-sized hammer. Some caution has to be taken when comparing spectra, since the force responses are defined in rms N and in addition sensitive to the window length. A quick scaling of transient events recorded with different window length, is performed by calculating the total signal energy and comparing them. The total energy is obtained by:

$$E_{FF}(\omega,T) = T \cdot S_{FF}$$

where T is the record window length and S_{FF} the power spectral density or PSD of F.

The PSD is also equal to:

$$S_{FF} = T \cdot F^2$$

where F^2 is the autospectrum.

Then the total signal energy is equal to:

$$E_{FF}(\omega,T) = T^2 \cdot F^2$$

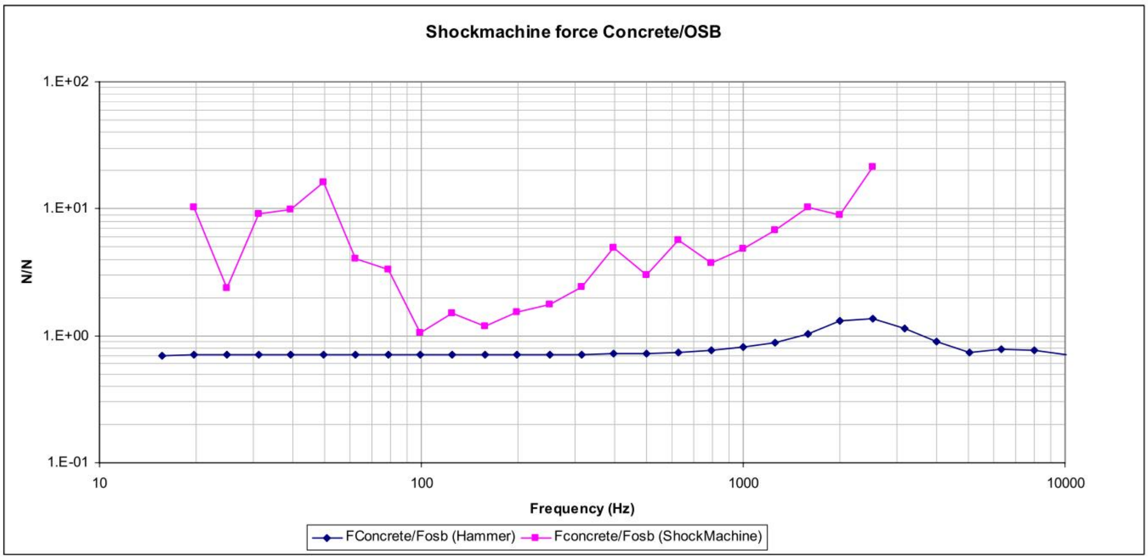

Figure 4.30: Ratio of force_concrete/force OSB estimated during tapping machine test and in impact hammer test

When directly observing compared force spectra applied by impact hammer and tapping machine (figures 4.31 and figure 4.32), tapping machine spectrum exhibits larger offset when compared to impact hammer for hard concrete slab impacts (figure 4.32). This offset is smaller when the force is applied to OSB (figure 4.31). OSB force from tap machine generates less high frequency content giving a bell-shaped force spectrum.

Comparing tap machine force on both OSB and concrete (figure 4.33) shows in a better way that the OSB impact is less efficient in the high frequency range, probably due to low-pass filtering of injected power, which is common and normal for soft structures.

To conclude, the tapping machine is interacting with the floor bending stiffness. Up to 500 Hz, it is assumed that the force is nearly independent of floor bending stiffness while this assumption is not valid above 500 Hz. As shown in this report, PIM test protocol is providing a convenient way to calibrate the tapping machine spectrum in order to predict reliable output levels of vibration from the SEA model.

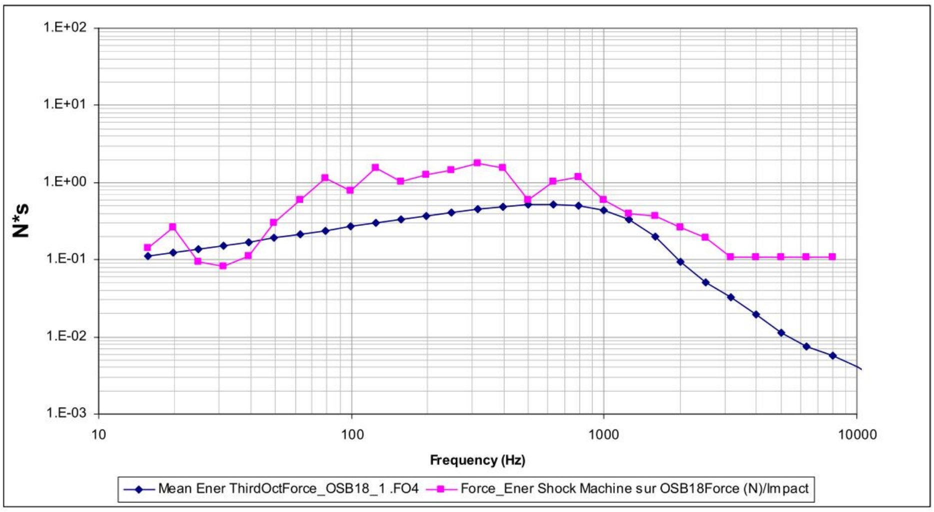

Figure 4.31: RMS spectrum of mean force applied by shock machine when operating on OSB floor and related rms force spectrum of mean force applied with impact hammer

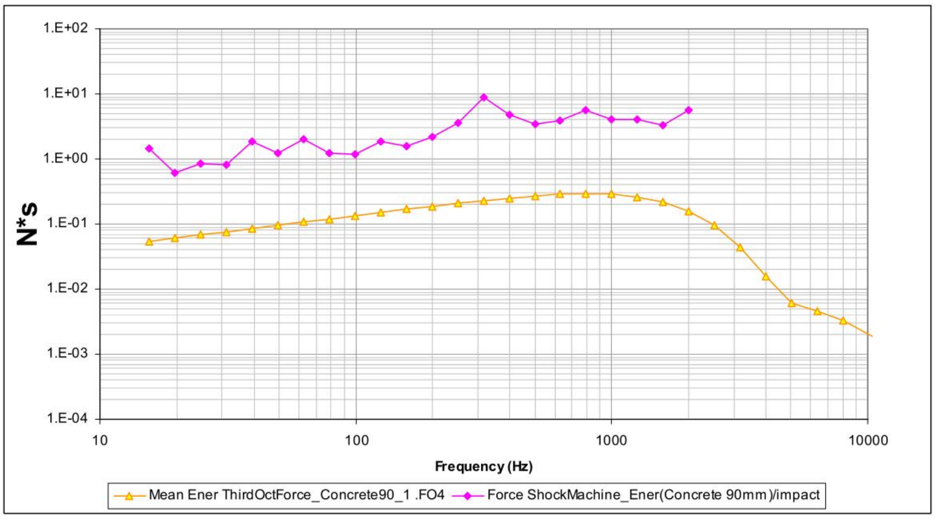

Figure 4.32: RMS spectrum of mean force applied by shock machine when operating on concrete floor and related force spectrum of mean force applied with impact hammer

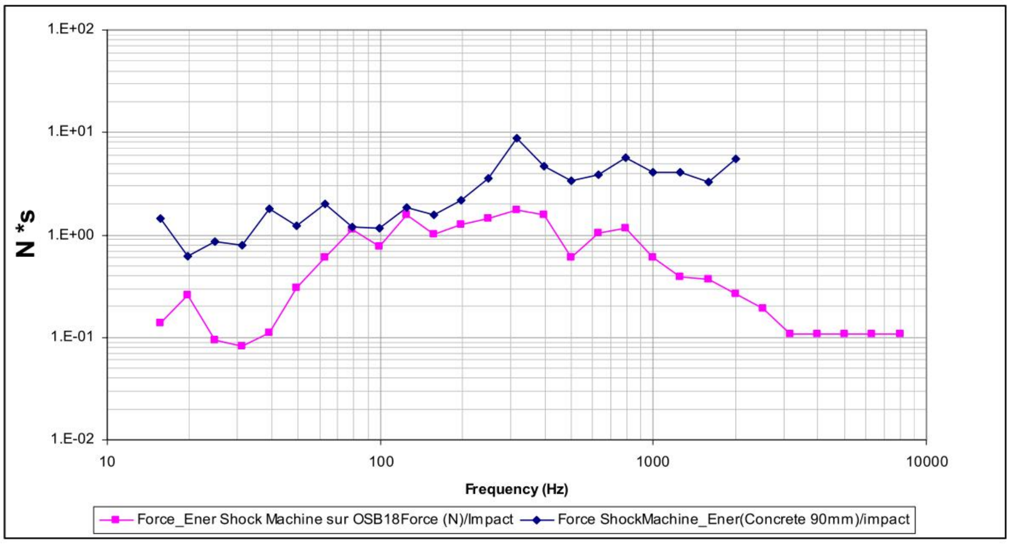

Figure 4.33: Compared reconstructed mean force spectra per impact applied by shock machine when operating on concrete and OSB floors

4.3 Prediction of Time history response to the shock machine

4.3.1 Brief explanations on SEA-SHOCK theory

The SEA-Shock module, available in SEAWOOD, is here used for reconstructing a time history response from the SEA model. The SEA model does not deliver any invertible transfer so to reverse the analysis to time domain, some additional signal processing is required together with some assumptions.

First of all, a force time history is needed as input. Second, connected subsystems need to be weakly coupled in order to reconstruct a scaling function (a modal complex FRF) based only on the local dynamic response of the receiver (subsystem in which we need the time history response), in any subsystem.

The theory implemented in SEA-Shock is based on the calculation of this scaling function obtained for a normalized complex modal response to a unit-force applied in the receiver subsystem. This special FRF is providing a phase to the real-valued SEA transfer, given by the classic frequency solution of the SEA network. In the receiver, the real-valued FRF is made complex and the complex amplitudes are given in narrow frequency bands and interpolated for satisfying the condition that their integral over the SEA frequency bands has to converge to the prescribed SEA FRF modulus. This is the essence of the LMPR algorithm (Local Modal Phase Reconstruction) which provides an invertible FRF function in the complex frequency domain. Convoluted with the time history of the input, the time history of the receiver can then be synthesized. This methodology has been developed over ten years in research applied to spacecraft to predict response to aerospace shock" tests. Some complements have been added for its application to wooden structures.

4.3.2 Concrete floor transient response

In order to perform a quick calculation with SEA-Shock, representative forces in the time domain have to be defined. To do that the Pulse Generator function of SEA is used. Figure 4.34 shows how the pulse response is fitted manually in order to describe the T*PSD response of the receiver. T is the time window of the transient record and PSF states for power spectral density. The product T*PSD corresponds to the total energy (in the signal processing sense) contained in the signal which is independent of the window length and sampling frequency as soon as the transient is captured in the window.

By choosing an exponentially decaying sine signal, the measured T*PSD level is roughly estimated. This signal is made impulsive with an arbitrary duration of around 10 ms.

When this input time history signal (named "Shock machine approximation") is stored in SEAWOOD database, it has to be allocated to a time domain source, as seen in figure 4.35.

The subsystem is declared as "LMPR receiver", LMPR being the name of the shock reconstruction algorithm as detailed in previous paragraph. This declaration indicates to the LMPR solver that the reconstruction of the time history will be performed on this particular subsystem. The LMPR receiver, after declaration, is surrounded by a transparent sphere, indicating where shock outputs are generated.

In figure 4.36 the comparison between prediction and measured response is shown. As expected from selected T*PSD force spectrum, low and mid frequencies content below 500 Hz is well reconstructed and the high frequencies are filtered as selected excitation is behaving like a low-pass filter. That is the reason why the measured signal is filtered by a second order low-pass filter and then compared to the predicted signal.

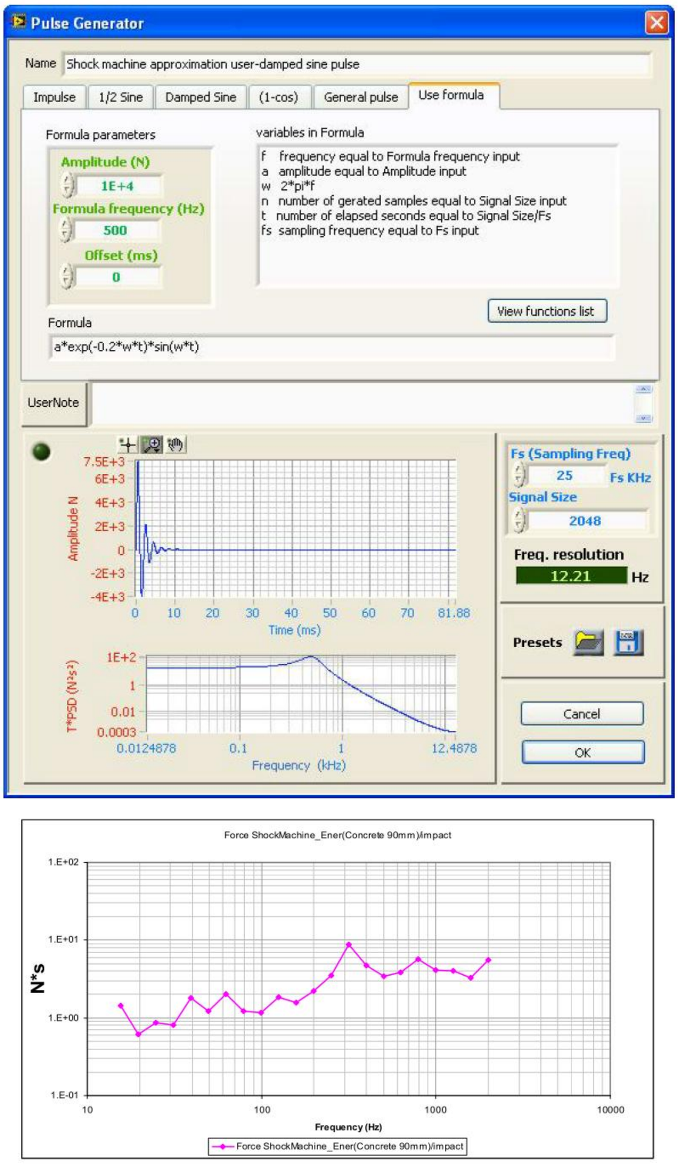

Figure 4.34: Pulse Generator dialog box in SEA+ and entering a formula for fitting with current force autospectrum

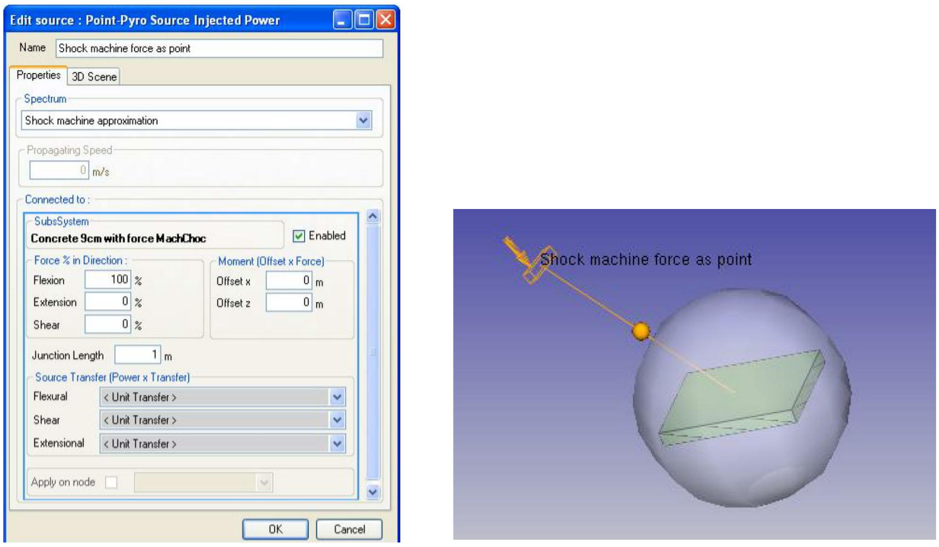

Figure 4.35: Setting the shock source to "Shock machine approximation"

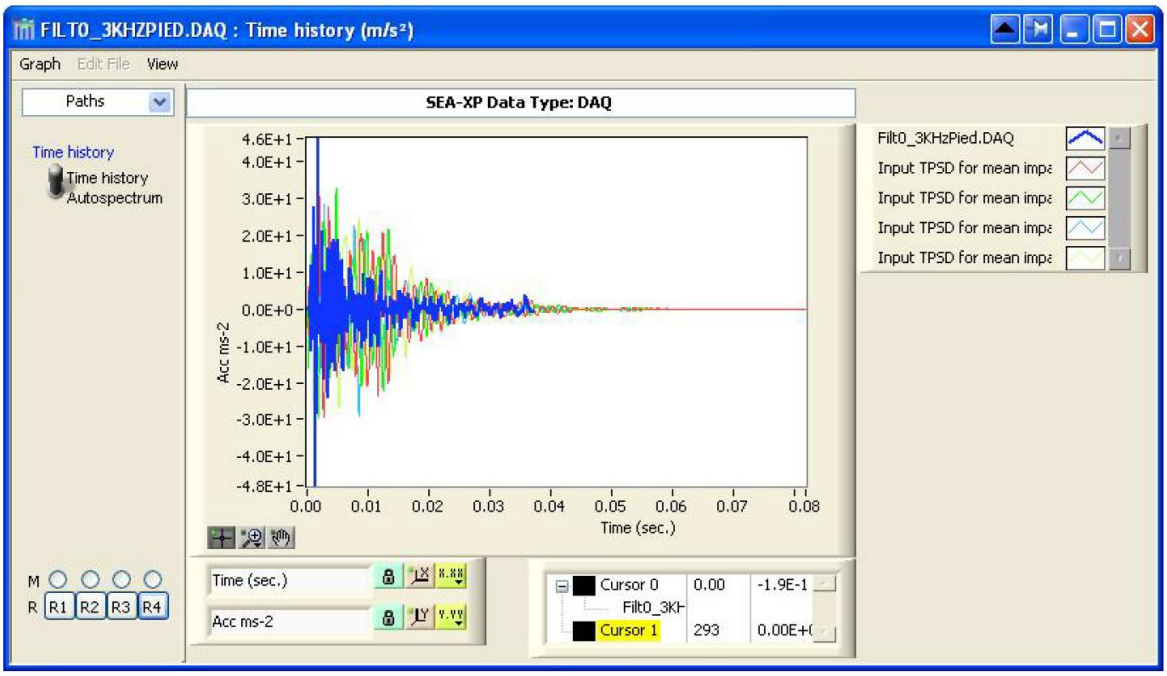

Figure 4.36: Predicted and measured force pulse (blue) when impacting the concrete floor

4.4 Conclusions

Providing correct injected power spectrum from the tapping machine has been achieved using the Power Injected Method (PIM) as implemented in the acquisition software SEA-XP [43]. SEA-XP was applied on isolated floors. Analysis shows that the injected power from the tapping machine is dependent on floor bending stiffness.

Installed on a soft OSB floor, the tapping machine delivers less high frequency force level than on a heavier and harder concrete slab.

The transient response of the floor was also simulated with success by SEA-Shock module of SEAWOOD software [49].

However, defining force as input to simulation is still difficult to assess with accuracy since the force from the tapping machine itself was not directly measured in the test campaign within the Silent Timber Build project. Instead an existing SEA-Shock force profile was tuned to fit the identified power injected spectrum from the tapping machine, inducing limitation in the high frequency range. However, keep in mind that for evaluation of experienced impact sound level this high range is of less importance.

Shaping the force spectrum playing on its time domain representation is not easy. Alternate solutions for source representation are now implemented in latter updates of SEAWOD but have not been applied in this current work program due to time schedule.

The shock source is now represented by either an acceleration Power Spectral Density (PSD), an acceleration time history or a Shock Response Spectrum (SRS). PSD signal is decomposed into series of transient wavelets of which coefficients are scaled to retrieve the input prescribed PSD. The selected wavelet bank gives the guaranty that the reconstructed time history signal is enough impulse. With the new SEA-Shock sources, if some acceleration time history record is available near the tappping machine, it would alternatively be used as input to SEA-Shock, avoiding complementary dispersion due to wavelet reconstruction when using steady-state PSD. In all cases, these sources are expected to describe in an easier way the tapping machine source.

5 Conclusions

WP 1 has developed general models from very low frequencies to high frequencies. We are able to model both airborne sound insulation with high accuracy but also impact sound levels. For impact sound level it is helpful to compare with measured data using the grouping from WP 2 in order to verify the first model.

6 References (2 p)

[1] C. Coguenanff, “Robust design of lightweight wood-based systems in linear vibroacoustics,” Univeristé Paris - Est, Ecole doctorale SIE, 2015.
[2] R. Ohayon and C. Soize, *Structural Acoustics and Vibration*. Academic Press, 1998.
[3] J.-F. Allard and N. Atalla, *Propagation of Sound in Porous Media*. Wiley, 2009.
[4] *NF EN ISO 10140-2 : Acoustics -- Laboratory measurement of sound insulation of building elements -- Part 2: Measurement of airborne sound insulation*. 2013.
[5] *NF EN ISO 10140-3 : Acoustics -- Laboratory measurement of sound insulation of building elements -- Part 3: Measurement of impact sound insulation*. 2013.
[6] *NF EN ISO 10140-5 : Acoustics -- Laboratory measurement of sound insulation of building elements -- Part 5: Requirements for test facilities and equipment*. 2013.
[7] *NF EN ISO 717-1 : Acoustics -- Rating of sound insulation in buildings and of building elements -- Part 1: Airborne sound insulation*. 2013.
[8] *NF EN ISO 717-2 : Acoustics -- Rating of sound insulation in buildings and of building elements -- Part 2: Impact sound insulation*. 2013.
[9] J. Brunskog and P. Hammer, “The interaction between the ISO tapping machine and lightweight floors,” *Acta Acust.*, vol. 89, no. 2, pp. 296–308, 2003.
[10] C. Guigou-Carter and C. Coguenanff, “Prediction of the acoustic performance of floor coverings on lightweight floors,” *Inter-noise 2015*, 2015.
[11] C. Coguenanff, C. Guigou-carter, P. Jean, and C. Desceliers, “Probabilistic Model of the Impact Force Spectrum for the Standard Iso Tapping Machine,” in *ICSV22*, 2015, no. July, pp. 12–16.
[12] H. Chung, G. Dodd, G. Emms, K. Mcgunnigle, and G. Schmid, “Maximising impact sound resistance of timber framed floor / ceiling systems,” Forest and Wood Products Research and Development Corporation, 2006.
[13] J. Brunskog and P. Davidsson, “Sound Transmission of Structures. A Finite Element Approach with Simplified Room Description,” *Acta Acust. united with Acust.*, vol. 90, no. 5, pp. 847–857, 2004.
[14] P. Davidsson, J. Brunskog, P.-A. Wernberg, G. Sandberg, and P. Hammer, “Analysis of Sound Transmission Loss of Double-Leaf Walls in the Low-Frequency Range Using the Finite Element Method,” *Build. Acoust.*, vol. 11, no. 4, pp. 239–257, 2004.
[15] L. Gagliardini, J. Roland, and J.-L. Guyader, “The use of a functional basis to calculate acoustic transmission between rooms,” *J. Sound Vib.*, vol. 145, no. 3, pp. 457–478, 1991.
[16] S. Maluski and B. M. Gibbs, “Application of a finite-element model to low-frequency sound insulation in dwellings,” *J. Acoust. Soc. Am.*, vol. 108, no. 4, pp. 1741–1751, 2000.
[17] S. Maluski and B. M. Gibbs, “The effect of construction material, contents and room geometry on the sound field in dwellings at low frequencies,” *Appl. Acoust.*, vol. 65, no. 1, pp. 31–44, 2004.
[18] P. Jean, H. Siwiak, and G. Joubert, “A Decoupled Vibro-Acoustic Development of FEM: Application to Laboratory Modelling,” *Build. Acoust.*, vol. 13, no. 2, pp. 83–98, 2006.
[19] J.-D. D. Chazot and J.-L. Guyader, “Prediction of transmission loss of double panels with a patch-mobility method,” *J. Acoust. Soc. Am.*, vol. 121, no. 1, p. 267, 2007.
[20] F. Fahy, *Foundations of Engineering Acoustics*. Academic Press, 2003.
[21] J. L. Davy, “The variance of decay rates at low frequencies,” *Appl. Acoust.*, vol. 23, no. 1, pp. 63–79, 1988.
[22] K.-J. Bathe, *Finite Element Procedures*. Prentice-Hall, 1996.
[23] M. Villot and C. Guigou-Carter, “Measurement Methods Adapted to Wood Frame Lightweight Constructions,” *Build. Acoust.*, vol. 13, no. 3, pp. 189–198, 2006.
[24] J. D. Quirt, “Controlling air-borne and structure-borne sound in buildings,” *Inter-noise 2009*, 2009.

[25] T. Nightingale, B. Zeitler, S. Schoenwald, and F. King, “A hierarchy of flanking transmission paths in lightweight wood frame construction,” *Inter-noise 2009*, 2009.
[26] M. Villot and C. Guigou-Carter, “Predicting Sound insulation in wood frame buildings,” *Inter-noise 2009*, 2009.
[27] C. Guigou-Carter, M. Villot, and R. Wetta, “Comparison of measured and predicted sound insulation in wood frame lightweight buildings,” *Inter-noise 2010*, 2010.
[28] C. Guigou-Carter, M. Villot, and R. Wetta, “Prediction Method Adapted to Wood Frame Lightweight Constructions,” *Build. Acoust.*, vol. 13, no. 3, pp. 173–188, 2006.
[29] E. Gerretsen, “Possibilities to improve the modelling in EN 12354 for lightweight elements,” *Euronoise 2006*, 2006.
[30] M. Villot, “Modelling flanking transmissions in lightweight constructions,” *Forum Acusticum - CIB Meet. 2002*, 2002.
[31] C. Guigou-Carter and M. Villot, “Prediction and measurements for lightweight buildings and low frequencies,” *Euronoise 2012*, no. June, 2012.
[32] C. Guigou-Carter and M. Villot, “Junction characteristics for predicting acoustic performance of lightweight wood-based buildings,” in *Internoise 2015*, 2015.
[33] *NF EN 338 : Structural timber - Strength classes*. 2009.
[34] “Wood Handbook,” United States Department of Agriculture, Forest Service, 2010.
[35] *NF EN 12369-1 : Wood-based panels - Characteristic values for structural design - Part 1 : OSB, particleboards and fiberboards*. 2001.
[36] R. Panneton, “Comments on the limp frame equivalent fluid model for porous media,” *J. Acoust. Soc. Am.*, vol. 122, no. 6, 2007.
[37] Y. J. Kang and J. S. Bolton, “Finite element modeling of isotropic elastic porous materials coupled with acoustical finite elements,” *J. Acoust. Soc. Am.*, vol. 98, no. 1, pp. 635–643, 1995.
[38] R. Ohayon and C. Soize, *Advanced Computational Vibroacoustics*. Cambridge University Press, 2014.
[39] G. Borello, Analyse statistique énergétique (SEA: Statistical Energy Analysis) de l'environnement vibroacoustique, Techniques de l’ingénieur, R 6 215v2 (R 6 215), mis à jour et ajout du paragraphe: Dimension finie des liaisons entre sous-systèmes SEA).
[40] InterAC, SEA+/SEAWOOD 2016 User Guide, www.interac.fr
[41] G. Borello, L. Gagliardini, L. Houillon, L. Petrinelli, "Virtual SEA: Mid-Frequency Structure-Borne Noise Modeling Based on Finite Element Analysis",SAE Noise and Vibration Conference, May 6-8, 2003.
[42] Lalor N., "The Experimental Determination of Vibrational Energy Balance in Complex Structures", Paper 108429 Proc. SIRA Conference on Stress & Vibration, 1989.
[43] InterAC, SEA-XP User Guide, Version 2015.
[44] InterAC, SEA-TEST User Guide, Version 2016.
[45] G. Borello, Alliot, A. Kernilis, "Identification of SEA Coupling Loss Factors on a Liquid Rocket Engine", Inter-Noise 1991.
[46] G. Borello, "Prediction of Sound Transmission in Complex Timber-Framed Structures in The Mid and High Frequency Range", Inter-Noise 2012.
[47] G. Borello, L. Gagliardini, L. Houillon, L. Petrinelli, "Virtual SEA-FEA-Based Modeling of Structure-Borne Noise", Sound and Vibration Magazine, January 2005.
[48] G. Borello, J. Primus, R. Nguyen Van Lan, S. Kiryenko, "Prediction of Payload Shock Response in the Mid And High Frequency Range", ECSSMMT, September 15-17, 2009.
[49] InterAC, SEA-Shock module 2016 User Guide, www.interac.fr
[50] Kouyoumji Jean-Luc, Borello Gerard, Ferk Heinz, Reverse sea to predict flanking transmission in timber framed constructions (Silent Timber Build, special session), International Congress on Acoustics, ICA 2016 paper 372, Buenos Aires, Argentina.
[51] Kouyoumji Jean-Luc, Bard Delphine, Borello Gérard, Guigou Catherine, Challenges for acoustic calculation models in "Silent Timber Build", Part 2 Internoise 2014, 16-19 November, Melbourne Australia
[52] Delphine Bard, Gerard Borello, Catherine Guigou and Jean-Luc Kouyoumji Challenges for acoustic calculation models in "Silent Timber Build" The 21st ICSV International

Congress on Sound and Vibration, 13-17 July, 2014, Beijing/China
[53] Bard, Delphine, Negreira, Juan, Kouyoumji, Jean-Luc, Borello, Gérard, Guigou, Catherine, Challenges for acoustic calculation models in "Silent Timber Build", Part 1-FEM Internoise 2014, 16-19 November, Melbourne Australia,
[54] Kouyoumji Jean-Luc, Predicting Sound Transmission Loss of timber framed walls and floors using SEA, in “AcouBois” project of the French wood industry, Internoise 2015, 9-12 August 2015, San Francisco, USA.
[55] Kouyoumji J.L, Predicting Sound Transmission Loss on of lightweight timber framed construction using SEA, 42nd Internoise Congress, 15-18 September, 2013, Innsbruck, Austria.
[56] Kouyoumji J.L, Vibro-Acoustic Prediction of Flanking Transmission in lightweight timber framed construction using SEA, 41st Internoise Congress, August 19-22, 2012, New York City, USA
[57] Ökvist, R; Measurement and perception of Sound Insulation from 20 Hz between Dwellings. Doctoral Thesis; ISBN 978-91-7583-869-4 (pdf) (2017)

Silent Timber Build

The overall objectives of Silent Timber Build project are to develop prediction models for multi storey buildings using various wooden floor and wall assemblies in the structural elements.